UNIVERSITY OF HYDERABAD

DOCTORAL THESIS

Particle scattering by ultracold quantum gases of trapped atoms

This thesis is submitted to the University of Hyderabad in partial fulfilment of the requirements for the award of the degree of

Doctor of Philosophy in Physics.



Submitted by

Samir Das

[Reg. No.: 16PHPH09]

Under the Supervision

of

Dr. Shyamal Biswas

School of Physics University of Hyderabad C.R. Rao Road, Gachibowli Hyderabad-500046, India

March 27, 2023



DECLARATION

I hereby declare that the matter embodied to this thesis entitled "Particle scattering by ultracold quantum gases of trapped atoms" is an outcome of the theoretical research carried out by me at the School of Physics, University of Hyderabad-500046, Hyderabad, India under the supervision of Dr. Shyamal Biswas.

I also declare that this thesis has not been submitted previously in part or in full to any other University or Institution for the award of any degree or diploma.

I hereby agree that my thesis can be deposited to the institutional repository.

I further declare that this thesis is based on my original work done under the supervision of Dr. Shyamal Biswas. I have cited all the relevant sources from which ideas and results are taken. The Library report on the originality is enclosed at the end of the thesis.

In conclusion, I bear the sole responsibility of any errors that might have crept into the thesis.

Place: Hyderabad

Date: March 27, 2023

Samir Das

Samor Das

Reg. No.: 16PHPH09



CERTIFICATE

This is to certify that the thesis entitled "Particle scattering by ultracold quantum gases of trapped atoms" submitted by the student Mr. Samir Das (Reg. No. 16PHPH09) in partial fulfilment of the requirements for the award of the degree of Doctor of Philosophy in Physics is a bonafide work carried out by him under the direct supervision of Dr. Shyamal Biswas at the School of Physics, University of Hyderabad, Hyderabad-500046, India.

This thesis is free from plagiarism and has not been submitted previously in part or in full to any other University or Institution for an award of any degree or diploma.

Further, the student (Mr. Samir Das) got the following research publications, which are related to the present thesis, before its submission for adjudication.

Publications in Peer Reviewed International Journals

- (1) Title: *Particle scattering by harmonically trapped Bose and Fermi gases*Authors: Ankita Bhattacharya, <u>Samir Das</u>, and Shyamal Biswas
 Published in: **Journal of Physics B: Atomic, Molecular and Optical Physics**51, 075301 (2018)
- (2) Title: *Particle scattering by rotating trapped quantum gases at finite temperature* Authors: <u>Samir Das</u> and Shyamal Biswas
 Published in: **Physica Scripta** 96, 125037 (2021)
- (3) Title: *Inelastic particle scattering by rotating harmonically trapped quantum gases*Author: <u>Samir Das</u>
 Published in: **Physics Letters A** <u>397</u>, 127249 (2021)
- (4) Title: Particle scattering by harmonically trapped quantum gases in an artificial magnetic field

Author: Samir Das

Published in: Physica B: Condensed Matter 635, 413833 (2022)

Further, the student presented his doctoral research work at the following conferences before the submission of this thesis for adjudication.

Conferences Attended

(1) Condensed Matter Days-2019 (CMDAYS-19):

Venue: Department of Physics, Vidyasagar University, West Bengal, India

Duration: August 29-31, 2019

Contributory Talk Title: Particle scattering by harmonically trapped Bose and Fermi

gases in different gauge fields

(2) National Conference on Advancement in Interdisciplinary Research (NCAIR-2021):

Organizer: Amiruddaula Islamia Degree College (Lucknow, India) and Sci-

ence Tech Institute (Lucknow, India)

Duration: July 29-31, 2021

Contributory Online Talk Title: Inelastic scattering of a particle by rotating har-

monically trapped quantum gases

(3) International Conference on Frontier Areas of Science and Technology (ICFAST-2022):

Venue: University of Hyderabad, Hyderabad, India

Duration: September 09-10, 2022

Poster Presentation Title: Thermodynamic properties of a particle scattering by ro-

tating trapped quantum gases

Further, the student completed the following Ph.D. (Physics) coursework before the submission of this thesis for adjudication.

Ph.D. (Physics) Courses Taken [in the Semester July-December, 2017]

S.No.	Course Code	Name of the Course	Credits	Pass/Fail
1	PY-801	Research Methodology	4	Pass
2	PY-802	Advanced Quantum Mechanics	4	Pass
3	PY-803	Advanced Experimental Techniques	4	Pass
4	PY-804	Advanced Condensed Matter Physics	4	Pass

Show 1 Ring

Dr. Shyamal Biswas

Thesis Supervisor School of Physics University of Hyderabad

Date: March 27, 2023

Dr. Shyamal Biswas
Assistant Professor,
School of Physics,
University of Hyderabad,
C.R. Rao Road, Gachibowli,
Hyderabad-500046, India.

Prof. K.C. James Raju

Dean

School of Physics University of Hyderabad

संकाय अध्यक्ष / Dean भौतिकी संकाय / School of Physics हेदराचाद विश्वविद्यालय UNIVERSITY OF HYDERABAD हैदराबाद / HYDERABAD-500 046. भारत / INDIA.

ACKNOWLEDGEMENTS

I am happy to express my deep gratitude to my Ph.D. supervisor Dr. Shyamal Biswas for giving me an opportunity to join his research group and for supporting me in carrying out different theoretical tasks to accomplish my dream. I have benefited greatly from his immense knowledge and commitment. He is critical and insightful about my research questions and patient with my writing. He has given me many opportunities to attend conferences, workshops, and school. I learned so much through our numerous discussions. Moreover, I would like to thank him for his caring attitude and concern.

I would like to take this opportunity to thank my past and present doctoral review committee members Prof. B. V. R. Tata, Prof. Ashok Chatterjee, Prof. V. Subrahmanyam, and Prof. G. Vaitheeswaran for their valuable suggestions.

I am thankful to the present Dean Prof. K. C. James Raju and the former Deans Prof. Ashok Chatterjee, Prof. V. Seshubai, and Prof. Bindu A. Bambah for their support to the Ph.D. (Physics) program at the School of Physics, University of Hyderabad, India. I would like to acknowledge all the teachers of the School of Physics for their instructions, encouragement, and help. I would like to especially mention Prof. Ashok Chatterjee, Prof. P. K. Suresh, Prof. Surajit Dhara, Prof. S. Srinath, Prof. B. V. R. Tata, Prof. Nirmal K. Viswanathan, Prof. K. C. James Raju, Prof. V. Seshubai, Dr. V. Ashoka, Dr Manimaran P, Dr. Barilang Mawlong, Dr. Pratap Kollu, Dr. Venkataiah Gorige, and Dr. Abhiram Soori in this regard. I would also like to acknowledge all the non-teaching staff of the University of Hyderabad for their timely services.

I would like to acknowledge the financial support received from the University Grants Commission (UGC), India under the CSIR-UGC NET Junior/Senior Research Fellowship scheme during 2017-2022. I would also like to acknowledge the SERB-EMEQ Senior Research Fellowship which I received during 2022-2022.

My gratitude also goes to our past and present group members: Dr. Najirul Islam, Ms. Bandita Das, Mr. Prathyush Manchala, Mr. Avijit Ghosh, Mr. Bhairab Mondal, Mr. Dhrubajyoti Devsharma, and Ms. Reya Negi with whom I had many fruitful discussions and their love and timely help made me enjoy the doctoral research. I very much appreciate all their cooperation during my study at the School of Physics.

I am thankful to my collaborator Dr. Ankita Bhattacharya. I really appreciate the collaboration I received from her.

I also express my gratitude to the research scholar colleagues Mr. Pawan Kumar Verma, Mr. Mitesh Kumar Behera, Mr. Akshay Chatla, Mr. Nurul Hassan, Mr. Vinod Kumar Rajput, Mr. Soumen Nayak and Mr. Linga Murty for their help on many occasions.

I want to express my gratitude for the lessons I learned from my undergraduate and postgraduate teachers, especially Dr. Satadal Bhattacharyya and Prof. Debnarayan Jana.

I am always grateful to my parents (Mr. Kshitish Chandra Das and Mrs. Kanaklata Das) whose consistent love and efforts motivated me towards my research career. I am also thankful to my elder brothers Mr. Soumen Das and Mr. Sovan Das, and friends Mr. Pradip Manna, Mr. Astik Haldar, Mr. Subrata Das, Mr. Sudipta Show, and Mr. Tanmoy Maity, for their encouragement and help.

Finally, I thank all my family members for their cooperation and support during my doctoral study at the School of Physics, University of Hyderabad, India (2017-2023).

Place: Hyderabad

Date: March 27, 2023

Samin Jag Samir Das

Reg. No.: 16PHPH09

Dedicated to My Parents

List of Abbreviations

MOT Magneto-optical trap

K Kelvin

BEC Bose Einstein Condensation BCS Bardeen-Cooper-Schrieffer

 \vec{r} Position of a particle *LLL* Lowest Landau level

 $i \qquad \sqrt{-1}$

HF Hartree-Fock

μ Chemical Potential

 λ_T Thermal de Broglie wavelength

G-P Gross-Pitaevskii
EM Electromagnetic
dHvA de Haas-van Alphen Ω Rotational frequency QHE Quantum Hall effect g Coupling constant T Absolute temperature

V Volume

Physical Constants

Charge of electron (*e*)

Bohr radius (a_0)

Reduced Planck constant or Dirac constant (\hbar)

Speed of light (*c*)

Free space permittivity (ϵ_0)

Boltzmann constant (k_B)

 $1.60217662 \times 10^{-19} C$

 $5.29177210903(80) \times 10^{-11} m$

 $1.0545718 \times 10^{-34} \ m^2.kg.s^{-1}$

 $299792458 \ m.s^{-1}$

 $8.8541878128(13) \times 10^{-12} \ F.m^{-1}$

 $1.38064852 \times 10^{-23} \ m^2.kg.s^{-2}.K^{-1}$

Abstract

The Ph.D. (Physics) thesis entitled "Particle scattering by ultracold quantum gases of trapped atoms" presents the research work done by us (me and my collaborator / supervisor) during the last six years at the School of Physics, University of Hyderabad, India. The thesis consists of five chapters viz., [i] introduction, [ii] particle scattering by harmonically trapped quantum gases at finite temperatures, [iii] particle scattering by rotating trapped quantum gases at the finite temperatures, [iv] particle scattering by harmonically trapped quantum gases exposed to an artificial magnetic field, [v] conclusions and future scopes. The main contents and the discussion pertaining to the contents are systematically presented chapter wise.

Chapter 1: Introduction

In chapter 1, we have begun with the physics of scattering with some common examples of light scattering and particle scattering. We have introduced the basic scattering theory for particles with an emphasis on the quantum scattering theory. We have discussed various approximation techniques for the theoretical determination of the differential scattering cross-sections, such as - partial wave analysis, phase shift method, and Born approximation. Then we have obtained exact result for the Fermi-Huang potential by considering all orders of Born series for the particle scattering. Then we have briefly reviewed the particle scattering for unfixed scatterers having quantized motions in a box geometry for the Fermi-Huang potential. We have introduced several thermochemical properties of ultracold quantum (Bose or Fermi) gases of trapped scatterers having quantized motions. For the bosonic or fermionic scatterers, we have briefly introduced the Bose-Einstein condensation in a harmonically trapped geometry, the quantum Hall effect in rotating harmonically trapped Bose gas, the Abrikosov vortex lattice in a rapidly rotating harmonically trapped Bose-Einstein condensate, and the de Haas-van Alphen effect on harmonically trapped Fermi gas of uncharged atoms exposed to an artificial magnetic field.

Chapter 2: Particle scattering by harmonically trapped quantum gases at finite temperatures

In chapter 2, we have analytically explored the quantum phenomenon of particle scattering by harmonically trapped Bose and Fermi gases for the short ranged Fermi-Huang (δ_p^3) interactions between the incident particle and the scatterers. We have considered elastic scattering. We have predicted differential scattering cross-sections and their temperature dependence in this regard. The coherent scattering even by a single boson or fermion in the finite geometry gives rise to a new tool for determining the energy eigenstates of the scatterer. Our predictions on the differential scattering cross-sections can be tested within the present day experimental setups, specially, for (i) 3-D harmonically trapped interacting Bose-Einstein condensate (BEC), (ii) BECs in a double well, and (iii) BECs in an optical lattice.

Chapter 3: Particle scattering by rotating trapped quantum gases at finite temperatures

In chapter 3, we have analytically explored the quantum phenomena of particle scattering by rotating trapped quantum gases of electrically neutral bosons and fermions for the short-ranged Fermi-Huang interactions between the incident particle and the scatterers. We have considered rotating co-moving frame for all our analyses. We also have considered elastic scattering. We have predicted differential scattering cross-sections and their temperature and angular velocity dependencies in this regard, in particular, for an ideal Bose gas in a rotating harmonic trap, an ideal Fermi gas in a rotating harmonic trap, and a weakly interacting Bose gas in a slow rotating harmonic trap. We have theoretically probed the lattice-pattern of the vortices in a rapidly rotating strongly interacting Bose–Einstein condensate by the particle scattering method. We also have obtained de Haas-van Alphen-like oscillations in the differential scattering cross-section for an ideal ultracold Fermi gas in a rotating harmonic trap for $T \to 0$. Our predictions on the differential scattering cross-sections can be tested within the present-day experimental setups.

Chapter 4: Particle scattering by harmonically trapped quantum gases exposed to an artificial magnetic field

In chapter 4, we have analytically explored the quantum phenomena of particle scattering by harmonically trapped trapped quantum (Bose or Fermi) gases of electrically neutral atoms exposed to a uniform artificial magnetic field for the short-ranged Fermi-Huang interactions between the incident particle and the scatterers. We have considered elastic scattering. For the bosonic scatterers, we have obtained the differential scattering cross-section around the Bose-Einstein condensation point. For the fermionic scatterers, we have obtained artificial magnetic field dependent differential scattering cross-section exhibiting de Haas-van Alphen like oscillations for $T \to 0$. Here, the main difference from the theoretical study mentioned in chapter 2 is coming from the centrifugal force in the rotating frame. The difference has also been further made by the consideration of the inelastic scattering for all the above cases.

Chapter 5: Conclusions and future scopes

The final chapter (i.e. chapter 5) describes the summary of the thesis and the conclusions made out of the present work. This chapter also presents the future prospects and the scopes for further investigations.

Contents

Intro	oduction	1
1.1	Motivation and Objectives	1
1.2	Scattering	2
	1.2.1 Light Scattering	3
	Rayleigh Scattering	3
	Raman Scattering	4
	Compton Scattering	5
	X-ray Scattering	6
	1.2.2 Particle Scattering	9
	Electron Scattering	9
	Neutron Scattering	0
1.3	Theory for Particle Scattering	1
	1.3.1 Classical Scattering Theory	1
	1.3.2 Quantum Scattering Theory	2
	Scattering Cross-section	3
	Fermi-Huang Potential	4
	Lippman- Schwinger Equation	4
	Born Series	5
	Are the conditions for Born approximation experimentally sat-	
	isfy?	8
	Partial wave analysis of quantum scattering 1	9
1.4	The scattering length	.1
1.5	Quantum scattering for unfixed scatterers in a box geometry 2	4
1.6	Ultracold Gas	6
1.7	Properties of scatterers	6
1.8	Magneto-optical trapping (MOT)	8
1.9	A Bose-Einstein condensate	9
1.10	Properties of Bose-condensed gases	1
	1.10.1 Healing length	1
	1.10.2 The coherence properties of a Bose- Einstein Condensate 3	2
1.11	Rotating quantum gases	32
	1.11.1 Quantum Hall effect for rotating quantum gases	5
	1.11.2 The filling fraction	37
	1.11.3 Vortex Lattice	8
	1.11.4 Mean- field Quantum Hall regime	9
	1.1 1.2 1.3 1.4 1.5 1.6 1.7 1.8 1.9 1.10	1.1 Motivation and Objectives 1.2 Scattering 1.2.1 Light Scattering Rayleigh Scattering Raman Scattering Compton Scattering X-ray Scattering Electron Scattering Neutron Scattering 1.3 Theory for Particle Scattering 1.3.1 Classical Scattering Theory 1.3.2 Quantum Scattering Theory 1.3.2 Quantum Scattering Theory 1.3.4 Lippman- Schwinger Equation Fermi-Huang Potential Lippman- Schwinger Equation Born Series Are the conditions for Born approximation experimentally satisfy? Partial wave analysis of quantum scattering 1.4 The scattering length 2 Quantum scattering for unfixed scatterers in a box geometry 2 Ultracold Gas 7 Properties of scatterers 1 Magneto-optical trapping (MOT) 1 Magneto-optical trapping (MOT) 1 Magneto-optical trapping (MOT) 1 Poperties of Bose-condensed 1.10 Properties of Bose-condensed 1.11 Rotating quantum gases 1.11.1 Quantum Hall effect for rotating quantum gases 1.11.1 Quantum Hall effect for rotating quantum gases 1.11.2 The filling fraction 1.11.3 Vortex Lattice

	1.12	Introduction of Artificial Gauge	40			
	1.13	The Artificial de Haas-van Alphen effect	42			
2	Part	icle scattering by harmonically trapped quantum gases at finite tem-				
	pera	tures	47			
	2.1	Introduction	47			
	2.2	Particle scattering by a single scatterer in a harmonic trap	49			
		2.2.1 For a single scatterer in a 1D harmonic trap	50			
	2.3	For a single scatterer in a 2D harmonic trap	51			
		2.3.1 For a single scatterer in a 3D harmonic trap	51			
	2.4	Particle scattering by Bose and Fermi gases in thermodynamic equi-				
		librium in 3D harmonic traps	52			
		2.4.1 Weak interparticle interactions and finite size effects for Bose				
		scatterers in a 3D harmonic trap				
	2.5	Particle scattering by Bose scatters in other 3D optical traps	58			
		2.5.1 For Bose scatterers in a double-well potential	58			
		2.5.2 For Bose scatterers in a 1D optical lattice				
	2.6	Conclusions	63			
3	Part	icle scattering by rotating trapped quantum gases at finite temperatures	68			
	3.1	Introduction	68			
	3.2		70			
	3.3	Particle scattering by Bose and Fermi gases in rotating harmonic traps 3.3.1 The case of inter-scatterer interactions for the Bose gas at a fi-	7 5			
		nite temperature	77			
		The case of slow rotation	78			
		The case of rapid rotation with the formation of the vortex lattice	80			
	3.4	Probing artificial de Haas-van Alphen effect by elastic particle scattering	84			
	3.5	Probing artificial de Haas-van Alphen effect by inelastic particle scat-				
		tering	86			
	3.6	Conclusions	87			
4	Part	icle scattering by harmonically trapped quantum gases exposed to an				
	artif	icial magnetic field	94			
	4.1	Introduction	94			
	4.2	Scattering by trapped quantum gases in an artificial magnetic field at				
		finite temperatures	96			
	4.3	Scattering properties of Bose gases in an artificial magnetic field 1	06			
	4.4	Conclusions	07			
5	Con	onclusions and future scopes 11				
	5.1	Conclusions	.12			
	5.2	Future Scopes	13			

Chapter 1

Introduction

1.1 Motivation and Objectives

Both the light scattering and the particle scattering are useful to know the structural and physical properties of the scatterers. Particle scattering is further useful for understanding the transport properties of matter. However, it has not been realized so far that the differential cross-section, as well as the cross-section, of a scattering phenomenon could be a thermodynamic property except for a few cases, such as - the electron-phonon scattering and electron-electron scattering in a metal, critical opalescence, etc. While electron-phonon scattering and electron-electron scattering result in a temperature dependence of the resistivity which is proportional to the total scattering cross-section [1], the critical opalescence results in a temperature dependence of the differential scattering cross-section for the light scattering (Rayleigh scattering) by a liquid (or a mixture of liquids) near around its critical point where the density fluctuation plays a significant role [2]. In all the above examples, the scatterer(s) is either fixed or having classical motion. Systematic study of the temperature dependence of the differential scattering cross-section for a particle scattering has not been done so far with the consideration of the quantized bound motion of the scatterer except for particle(s) in a box [3].

There have been a lot of experimental and theoretical studies on ultracold Bose and Fermi gases in magneto-optical traps during the last three decades since the observation of the Bose-Einstein condensation of ultracold (μ K - nK) alkali atoms (23 Na, 87 Rb, etc) [4, 5, 6, 7, 8, 9, 10, 11, 12, 13, 14, 15, 16, 17]. The s-wave scattering length plays an important role in a gas of ultra-cold atoms [9, 18], in particular, determining its thermodynamic properties, such as - the Bose-Einstein condensate fraction [19], density profile of a harmonically trapped Bose gas below the condensation point [7, 20], BEC-BCS crossover of a harmonically trapped Fermi gas [11, 21], vortex lattice structure of a rotating harmonically trapped Bose-Einstein condensate [12, 22], etc. Scattering of impurity atoms with a harmonically trapped Bose-Einstein condensate has also been experimentally studied to probe the many-body effects in

it [23]. The impurity scattering in a Bose-Einstein condensate has also been theoretically studied for finite temperature [24]. Scattering of atoms on the harmonically trapped interacting Bose–Einstein condensate has also been theoretically investigated for $T \to 0$ [25]. However, the quantized bound motion of the magneto-optically trapped ultracold atom(s) has not been theoretical/experimentally probed by scattering of a beam of indecent particles so far for finite temperatures.

Thus we are motivated to theoretically prove the quantized bound motion of the magneto-optically trapped ultracold atom(s) at finite temperatures by the particle scattering method [26, 27, 28, 29]. For the simplicity, we consider short-ranged (Fermi-Huang) interaction(s) between an incident particle and the scatterer(s) in this regard. We mainly considered the elastic scattering for our analyses because inelastic scattering is less probabilistic at a finite temperature and the differential scattering cross-section in the inelastic channels decays exponentially with the number of scatterers beyond a certain value. In connection with the particle scattering by ultracold quantum gases of magneto-optically trapped atoms, we are motivated to find the following: (i) differential scattering cross-section for the Fermi-Huang interaction $(g\delta_n^n(\vec{r}))$ between an incident particle and a quantum harmonic oscillator at a finite temperature, (ii) differential scattering cross-section for a Bose or Fermi gas of quantum harmonic oscillators at a finite temperatures, (iii) differential scattering cross-section for a weakly interacting Bose gas at around the condensation point, (iv) differential scattering cross-section for Bose-Einstein condensates in double-well potential or optical lattice, (v) differential scattering cross-section for a rotating harmonically trapped interacting Bose gas, (vi) differential scattering cross-section for a rotating harmonically trapped Fermi gas, (vii) differential scattering cross-section for a harmonically trapped Bose or Fermi gas exposed to a uniform artificial magnetic field. These are our objectives for this thesis.

Let us now introduce various topics related to our objectives.

1.2 Scattering

Scattering is a phenomenon where an incident particle (or wave) changes its momentum (or wavevector) after colliding or interacting with an object (called scatterer) and remains free after the collision or interaction. There are numerous classic examples of scattering such as Rayleigh scattering, Rutherford scattering, X-ray scattering, Compton scattering, Raman scattering, electron scattering, neutron scattering, etc. While Rayleigh scattering, X-ray scattering, and Raman scattering in the above examples involve the scattering of light/photons by atoms, crystalline objects, and electrons, respectively, Rutherford scattering, electron scattering, and neutron scattering involve scattering of particles by atomic nuclei, crystalline objects, magnetic material, respectively. Let us now elaborate or introduce a few keywords for the light scattering, the particle scattering, and the theory for particle scattering.

1.2. Scattering 3

1.2.1 Light Scattering

One of the most important phenomena in daily life is light scattering. Light is a form of oscillating EM field which excites charges, hence radiating EM waves. The redirection of radiation away from its original propagating direction is known as light scattering. Light scattering usually occurs due to the interaction between EM waves and atomic or molecular electrons. In the case of the interaction between the EM waves and molecules, radiation is further coupled to the internal degrees of freedom of the molecules. In the case of light scattering, the EM wavelength is so much greater than the distances between the atoms that the atoms perceive a local uniform electric field. In the case of light scattering case, it makes sense to discuss how the radiation is coupled to a varying dielectric constant (related density fluctuations) for the medium. Elastic light scattering occurs when the wavelength remains same before and after collision but the intensity of the scattered radiation changes. On the other hand, the wavelength of the emitted radiation differs from that of the incident radiation due to inelastic scattering. The Maxwell equations provide the foundation for theoretical and computational approaches to describe light scattering from the classical point of view. In the following section, we will mention various examples of light scattering.

Rayleigh Scattering

Rayleigh scattering is the elastic scattering of light by particles (atoms or molecules) whose size (radius) is smaller than the wavelength of the incident light so that the scattered radiation spreads uniformly in all directions. The charges inside an atom or a molecule are affected by the oscillating electric field of a light wave, which causes them to vibrate with the same frequency. As a result, the atom or molecule transforms into a radiating dipole, the radiation of which we observe as scattered light. The differential cross-section due to the Rayleigh scattering is given by the following expression [30]

$$\frac{d\sigma}{d\Omega} = \frac{4\pi^2 (n-1)^2}{n_0^2 \lambda^4} (1 + \cos^2 \theta)$$
 (1.1)

where λ is the wavelength of the incoming radiation, θ is the scattering angle, n is the refractive index of the medium, and n_0 is the molecular number density. The scattered intensity is inversely proportional to the fourth power of the wavelength. Thus EM waves of short-wavelength scatter more than the EM wave of longer wavelengths. Because of its long wavelength, the red light is scattered less and the blue light is scattered more than the other colours because of its small wavelength. The sky appears blue for this reason.

Rayleigh scattering has an interesting application towards the temperature dependence of the differential scattering cross-section. The critical opalescence results in a temperature dependence of the differential scattering cross-section for the light scattering by a liquid (or a mixture of liquids) near around its critical point (T_c) where the density fluctuation plays a significant role [2]. The differential scattering cross-section for such a system near around the critical point takes the following form [2, 31]

$$\frac{d\sigma}{d\Omega} = \frac{V\pi^2}{\lambda^4} \left(\frac{\partial \epsilon}{\partial \rho}\right)_T^2 k_B T \rho^2 \beta_T \tag{1.2}$$

where λ is the wavelength of the incident plane monochromatic lightwave which is polarized perpendicular to the scattering plane, ϵ is the local isotropic dielectric constant, T is the temperature of the liquid medium, ρ is the density of the liquid medium, and $\beta_T = -\frac{1}{V} \left(\frac{\partial V}{\partial \rho} \right)_T$ is the isothermal compressibility which diverges as $\beta_T \propto |T-T_c|^{-1}$ near the critical point. This result was originally obtained by Einstein in 1910 [31]. In this thesis we study the temperate dependence of the differential scattering cross-section in connection with the particle scattering for various system of scatterers have quantized bound motion.

Raman Scattering

The Raman effect [32], also known as Raman scattering, is the inelastic scattering of photons by atoms molecules. This process involves a change in the frequency of the scattered radiation. Indian physicist C V Raman discovered it for light scattering by liquids. Raman scattering occurs in a fluid due to a change in the vibrational or rotational energy of a molecule. The schematic diagram of the Raman scattering is shown in figure 1.1.

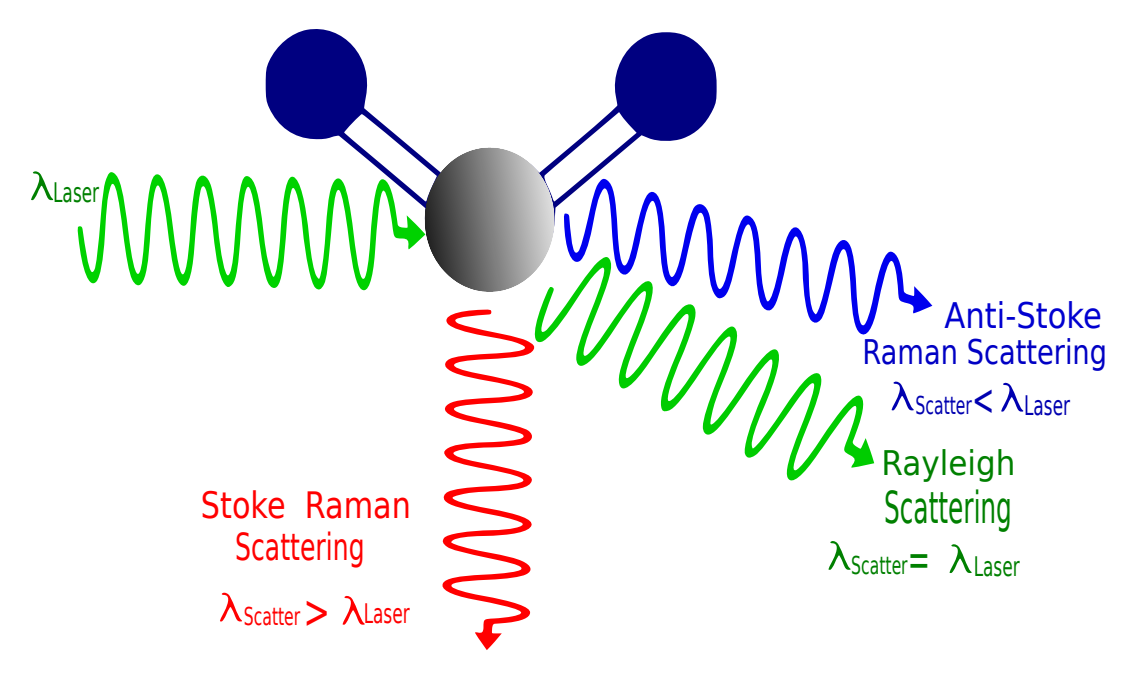


FIGURE 1.1: A schematic diagram for the Raman scattering.

Usually the Raman effect causes molecules to gain the vibrational energy as incident photons from a visible laser is shifted to lower energy. This is called the Stokes Raman scattering. On the other hand, energy of photons also increases in a reverse

1.2. Scattering 5

process by lowering the vibrational energy of molecules in anti-Stokes Raman scattering. The observed Raman shift of the anti-Stokes and Stokes properties is a direct measure of the vibrational energies of the molecule. The schematic diagram for the Stokes Raman scattering and the anti-Stokes Raman scattering is shown figure 1.2. The Raman Scattering technique is used in the medical diagnostic analysis, hyper-

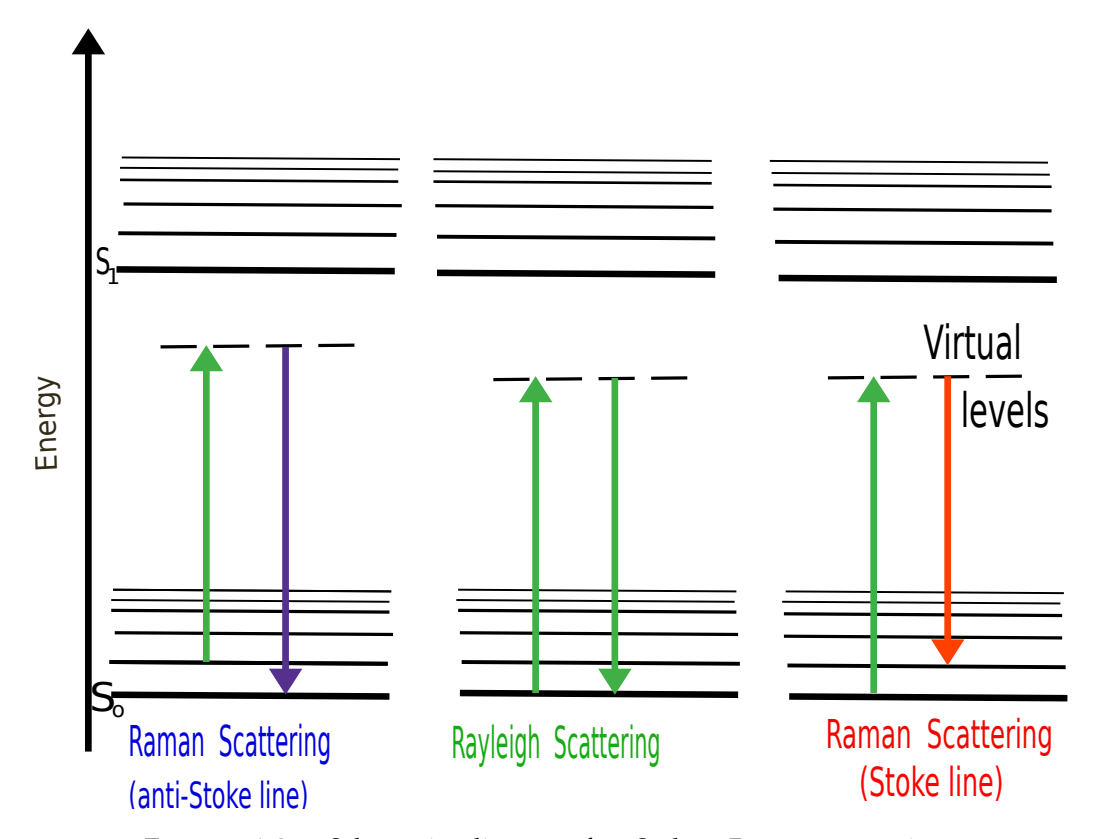


FIGURE 1.2: Schematic diagram for Stokes Raman scattering, Rayleigh scattering, and anti-Stokes Raman scattering are shown in the picture.

spectral molecular imaging of cells and tissue, and others. Raman spectroscopy can be applied to detect low-frequency excitations of the solid, such as magnons, plasmons, and superconducting gap excitations [33].

Raman transitions, on the other hand, may take place in an atom. Indirect EM transitions between two non-degenerate ground states of an atom via EM transitions to and from another excited state without any population inversion can be called as a Raman transition. Raman transitions can to used to create artificial gauge (magnetic) field.

Compton Scattering

The Compton effect occurs when a beam of photons inelastically collide with free electrons or charged particles [34, 35]. One of the most important methods of absorption of radiant energy by matter is Compton scattering which leads to an increase in the wavelength of X-ray and other intense electromagnetic rays (such as - gamma

ray) once they are scattered by the electrons. This effect has been shown to be one of the pillars of quantum mechanics because it explains both the wave and particle aspects of the radiation. The collision between a photon and an electron creates new a photon with reduced energy and momentum. The scattering angle for the new photon can be determined in terms of the amount of energy lost to the recoiling electron. The change in the wavelength of the photon due to the Compton scattering can be expressed by the following formula [35]

$$\lambda' - \lambda = \frac{\hbar}{m_0 c} (1 - \cos \theta) \tag{1.3}$$

where λ is the wavelength of incident photon, λ' is the wavelength of the (new) scattered photon, m_0 is the rest mass of the electron, θ is the angle at which the photon is scattered (i.e. the angle between the wave vectors \vec{k}' and \vec{k} of the scattered and incident photons, respectively, as shown in figure 1.3) and c is the speed of light in the free space.

According to one of the fundamental processes for the Compton scattering, an electron after completely absorbing the photon moves freely for a while before emitting the (new) scattered photon. The Feynman diagram for this process $(e^- + \gamma \rightarrow e^- + \gamma)$ is shown in figure 1.3. Compton scattering is used in radiation therapy.

X-ray Scattering

X-ray scattering occurs when an X-ray (EM wave) passes through a crystalline object and is elastically scattered by atoms at the lattice points [36]. The wavelength for the X-ray is nearly equal to the size of the lattice spacing of the crystal. Thus the X-ray scattering is useful to determine the lattice structure of a crystalline object [37].

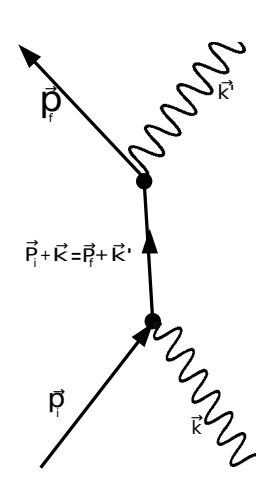


FIGURE 1.3: A Feynman diagram for the Compton scattering.

A crystalline object is periodic in space. Bragg's law for the scattering of an X-ray by two consecutive layers of a crystalline object (as shown is figure 1.4) can be written as $2d \sin \theta = n\lambda$ where n is an integer. This is the necessary condition for constructive interference between waves for an angle of incidence on two lattice planes separated by d. We need to determine the scattering amplitude for X-ray scattering by a "small" single crystal. Here, "small" indicates that we can neglect numerous scattering events. We assume the crystal is entirely periodic. The Fourier transform of the number density of scatterers (atomic electrons) is the form factor or the scattering factor for a single atom. The form factor can be expressed as follows [37]

$$f(\vec{q}) = \int n(\vec{r}) e^{-i\vec{q}\cdot\vec{r}} d^3\vec{r}$$
 (1.4)

1.2. Scattering 7

where $n(\vec{r})$ is the number density of the scatters (atomic electrons) at the position \vec{r} , \vec{k} is the wave vector of the incoming beam, $\vec{k'}$ is the wave vector of the scattered beam, and $\vec{k'} - \vec{k} = \triangle \vec{k} = \vec{q}$ represents the change in wave vectors. This form factor is also proportional to the scattering amplitude. By integrating over the entire crystal (instead of that for a single atom as shown in Eqn.

(1.4)) one can obtain the scattering amplitude in each final polarisation direction as [38]

$$f(\vec{q}) = r_0 \int_{Crystal} n(\vec{r}) e^{-i\vec{q}\cdot\vec{r}} d^3\vec{r} \left[\hat{\epsilon} \cdot \hat{\epsilon'}\right]$$
 (1.5)

where r_0 is the classical radius of the electron (i.e. the Thompson scattering length: $r_0 = \frac{e^2}{4\pi\epsilon_0 m_e c^2} \simeq 2.82 \times 10^{-5}$ Angstroms), $\hat{\epsilon}$ represents a unit vector for the polarization of the incident ray, and $\hat{\epsilon}'$ represents a unit vector for the polarization of the scattered ray. The crystal lattice structure can be represented as $n(\vec{r}) = n(\vec{r}_i + \vec{x}) = n(\vec{x})$ where \vec{r}_i represents the lattice translation for $i = 0, 1, 2, \ldots$. We can take the advantage of the periodicity of the number density to get the following result

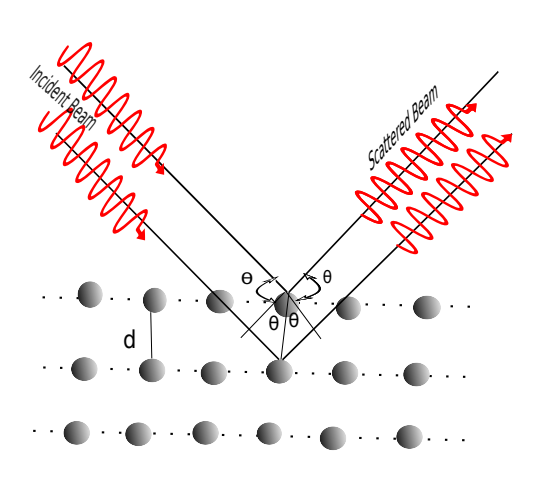


FIGURE 1.4: A schematic diagram for the Bragg scattering.

$$f(\vec{q}) = r_0 \sum_{j} \int_{\text{Unit Cell}} n(\vec{x}) e^{-i\vec{q} \cdot (\vec{r}_j + \vec{x})} d\vec{x} \left[\hat{\epsilon} \cdot \hat{\epsilon}' \right]$$

$$= \sum_{j} e^{-i\vec{q} \cdot \vec{r}_j} r_0 \int_{\text{Unit Cell}} n(\vec{x}) e^{-i\vec{q} \cdot \vec{x}} d\vec{x} \left[\hat{\epsilon} \cdot \hat{\epsilon}' \right]$$
the Structure Factor $F(\vec{q})$ (1.6)

where the summation is taken for all the unit cells of the crystal and $F(\vec{q}) = r_0 \int_{\text{Unit Cell}} n(\vec{x}) \mathrm{e}^{-i\vec{q}\cdot\vec{x}} \mathrm{d}\vec{x}$ is the structure factor of crystal. It is clear from this expression that the Fourier transform of the number density of the scatterers (atomic electrons) integrated over the unit cell of a crystal is essentially the structure factor of the crystal. The structure factor of a crystal can be determined by the X-ray scattering method. The differential scattering cross-section for the crystal can now be written as

$$\frac{d\sigma}{d\Omega} = |f(\vec{q})|^2 = \sum_{j} \sum_{i} e^{-i\vec{q}\cdot(\vec{r}_j - \vec{r}_i)} |F(\vec{q})|^2 |[\hat{\epsilon}\cdot\hat{\epsilon'}]|^2$$
(1.7)

where the double summation in the parentheses runs over all the lattice points of the crystal. The number density of the scatterers for a unit call, can however, be written as $n(\vec{x}) = \sum_{j=1}^{n_0} n_j(\vec{x}) = \sum_{j=1}^{n_0} f_j \delta(\vec{x} - \vec{r}_j)$ where $n_j(\vec{x}) = f_j \delta(\vec{x} - \vec{r}_j)$ is the number density of the scatterers (atomic electrons) bound to the jth atom in the unit cell, \vec{r}_j represents the position of the jth atom in the unit cell ($j = 1, 2, 3..., n_0$), n_0 is the number of atoms in the unit cell, and $f_j = f_j(\vec{q}) = \int n_j(\vec{x}) \mathrm{e}^{-i\vec{q}\cdot(\vec{x}-\vec{r}_j)} \mathrm{d}^3[\vec{x}-\vec{r}_j]$ is the

form factor for the *j*th atom. Thus the structure factor for a crystal takes the form

$$F(\vec{q}) = r_0 \sum_{j=1}^{n_0} f_j(\vec{q}) e^{-i\vec{q}\cdot\vec{r}_j}.$$
 (1.8)

This equation relates the form factor with the structure factor. Incidentally, this (classical) equation has a similarity with the equation for the scattering amplitude for the (quantum) particle scattering due to unfixed scatterers [26]. Evaluating over the summation over i and j of Eqn. (1.7) the differential scattering cross-section can, however, be recast as follows

$$\frac{d\sigma}{d\Omega} = \prod_{i=1}^{3} \frac{\sin^2(\frac{N_i \vec{q} \cdot \vec{a_i}}{2})}{\sin^2(\frac{\vec{q} \cdot \vec{a_i}}{2})} |F(\vec{q})|^2 |[\hat{\epsilon} \cdot \hat{\epsilon'}]|^2$$
(1.9)

where $\{\vec{a}_1, \vec{a}_2, \vec{a}_3\}$ are the primitive (translation) vectors for the unit cell of the crystal and $\{N_1, N_2, N_3\}$ are the number of lattice points along the three primitive vectors. It is clear from Eqn. (1.9) that the differential scattering cross-section has maxima for the following condition

$$\vec{q} \cdot \vec{a}_i = \triangle \vec{k} \cdot \vec{a}_i = 2\pi n_i \tag{1.10}$$

where i=1,2,3, and $n_1=h=0,1,2,3,...$, $n_2=k=0,1,2,3,...$, & $n_3=l=0,1,2,3,...$ are known as the Miller indices $\{h,k,l\}$. Eqn. (1.10) is known as the Laue condition or the Laue equation. By applying the Laue equations we recast the structure factor as

$$F_{h,k,l}(\vec{q}) = \sum_{j=1}^{n_0} \underbrace{f_j(\vec{q})}_{Amplitude} e^{-i\underbrace{2\pi(hx_j + ky_j + lz_j)}_{Phase}}$$
(1.11)

where $\vec{r}_j = x_j \vec{a}_1 + y_j \vec{a}_1 + z_j \vec{a}_3$ represents the position of the j atom in a unit cell and $\{x_j, y_j, z_j\}$ are the dimensionless coordinates for the j atom along the primate vectors \vec{a}_1, \vec{a}_2 , and \vec{a}_3 , respectively.

The arrangement of the atoms in the crystal determines the intensity of the diffraction peaks as follows

$$I_{h,k,l}(\vec{q}) \propto |F_{h,k,l}(\vec{q})|^2.$$
 (1.12)

Let us take an example of the bcc crystal. It has effectively two atoms in a unit cell. Their position can be described as (0,0,0) and $(\frac{1}{2},\frac{1}{2},\frac{1}{2})$ as one can see from figure 1.5. For identical atoms sitting at both the positions we have $f_i(\vec{q}) = f$. Thus we get the structure

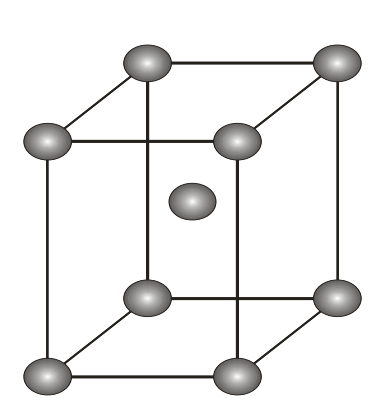


FIGURE 1.5: A schematic diagram for body centred orthorhombic crystal.

1.2. Scattering 9

factor for the bcc crystal as

$$F_{h,k,l}(\vec{q}) = f[1 + e^{i\pi(h+k+l)}]$$
 (1.13)

for the bcc crustal. This form can now be recast in terms of the Miller indices (which define a crystal plane) as follows

$$F_{h,k,l} = \begin{cases} 2f & \text{if } h+k+l = \text{even integer} \\ 0 & \text{if } h+k+l = \text{odd integer.} \end{cases}$$

For the bcc lattice, the X-ray scattering (diffraction) peaks are observed from the crustal planes like (200), (110), (222) but not from the planes like (100), (300), (111), (221).

Bragg scattering results in due to the scattering of a plane wave (X-ray) by successive parallel lattice planes of a reflecting crystal (see figure 1.4). The incident wave will be eventually diffracted after reflection from the set of parallel lattice planes. The separation between two consecutive parallel lattice planes (h, k, l) and (2h, 2k, 2l) can, however, be written as d such that $\frac{1}{d} = +\sqrt{\frac{h^2}{a_1^2} + \frac{k^2}{a_2^2} + \frac{l^2}{a_3^2}}$ if the primitive vectors are orthogonal. The intensity pattern due to the X-ray diffraction is modulated by the destructive and constructive interferences. Thus, the path length difference between the scattered waves coming out from two adjacent planes must be an integral multiple of the wavelength for the constructive interference. This leads to the Bragg's law

$$2d\sin\theta = n\lambda\tag{1.14}$$

 θ is the angle between incident wave and lattice plane (see in figure 1.4) and n is the order of diffraction. Lattice constant and the lattice planes (Miller indices) can be determined from the X-ray diffraction method.

1.2.2 Particle Scattering

The particle scattering, however, is applicable for a wide range of objects from nucleons to billiard balls. There are a few examples of particle scattering: electron scattering, neutron scattering, etc.

Electron Scattering

The Davisson-Germer experiment confirmed the existence of the wave associated with a particle (de Broglie's hypothesis). It marked a significant advancement in the development of quantum mechanics by giving wave-particle duality a solid experimental foundation. Let us consider the elastic scattering of electron due the Coulomb potential. Mainly electron scattering occurs when the incoming electron is scattered by a system of bound charged particles. Solids such as metals, semiconductors, and insulators are common examples of the occurrence of electron scattering.

The Coulomb potential arises due to the nucleus and the electrons bound in an atom. For simplicity, we assume the electrons are spinless particles. Within the first Born approximation, the scattering amplitude is proportional to the Fourier transform of scattering potential energy [39]. Thus we have the following result for the scattering amplitude for the particle scattering:

$$f(\theta,\phi) \simeq -\frac{1}{4\pi} \frac{2m}{\hbar^2} \int d^3 \vec{r} \ V(\vec{r}) e^{-i\vec{q}\cdot\vec{r}}$$
(1.15)

where $V(\vec{r})$ is the potential energy of the incident particle near an atom, m is the mass of the incident particle (electron), and $\vec{q} = \vec{k}' - \vec{k}$ is amount of the momentum transfer in the units of \hbar due to the scattering process. We can further recast the above result (by virtue of the Fourier transform and the integration by parts) as follows:

$$f(\theta,\phi) \simeq \frac{m}{2\pi\hbar^2 q^2} \int d^3\vec{r} V(\vec{r}) \nabla^2 e^{-i\vec{q}\cdot\vec{r}} = \frac{m}{2\pi\hbar^2 q^2} \int d^3\vec{r} e^{-i\vec{q}\cdot\vec{r}} \nabla^2 V(\vec{r}). \tag{1.16}$$

The expression for the charge density of an atom with atomic number Z is $\rho(\vec{r}) = Ze \ \delta^3(\vec{r}) + (-e) \ \rho_{el}(\vec{r})$ where the ρ_{el} is the number density of the bound electrons of an atom and -e is the charge of an electron. Now using Poisson's equation electrostatic potential $V(\vec{r})$ we have

$$\nabla^2 V(\vec{r}) = e^2 \left(Z \delta^3(\vec{r}) - \rho_{el}(\vec{r}) \right) / \epsilon_0. \tag{1.17}$$

The expression for differential scattering cross-section for this process takes the following form

$$\frac{d\sigma}{d\Omega} = |f(\theta, \phi)|^2 \simeq \left(\frac{me^2}{2\pi\epsilon_0 \hbar^2 q^2}\right)^2 \left| Z - \int \rho_{el}(\vec{r}) e^{-i\vec{q}\cdot\vec{r}} d^3\vec{r} \right|^2$$
(1.18)

where the integral $\int \rho_{el}(\vec{r})e^{-i\vec{q}\cdot\vec{r}}\mathrm{d}^3\vec{r} = f(\vec{q})$ is the form factor which have already been introduced in connection with the X-ray scattering. The term $\frac{me^2}{2\pi\epsilon_0\hbar^2}$ in the parentheses of the above equation takes the approximate value $3.779\times10^{10}~\mathrm{m}^{-1}$. This term divined by q^2 is analogous to the Thompson scattering length (classical radius of an electron) $r_0 = \frac{e^2}{4\pi\epsilon_0mc^2} \simeq 2.82\times10^{-15}\mathrm{m}$ for the X-ray scattering. Therefore, we can see that the range of q (1-10 Å $^{-1}$) is used in the electron diffraction experiments.

Neutron Scattering

Neutron scattering occurs when neutrons are scattered with atomic nuclei via very short-range (\sim fm) forces. A magnetic dipole interaction also occurs between Neutrons and unpaired electrons. Neutron wavelength is much greater than the range of nuclear force (\sim 1 fm), so Neutron scattering is "point-like." Scattering is elastic because the energy of the neutron is very small to change the energy of the nucleus

and the Neutron cannot transfer KE to a fixed nucleus. Neutron scattering cross section by a single (fixed) nucleus is given by $\sigma = 4\pi b^2$ [40]. Here, we only take into account scattering away from nuclear resonances, at which neutron absorption is nominal. If the neutrons are scattered by many nuclei then the differential scattering cross-section can be written as [40]

$$\frac{d\sigma}{d\Omega} = \sum_{i,j} b_i b_j e^{-i\vec{q} \cdot (\vec{R}_i - \vec{R}_j)}. \tag{1.19}$$

The scattering length b_i is influenced by the nuclear isotope, spin, etc. For a single nucleus, the differential scattering cross-section is [40]

$$\frac{d\sigma}{d\Omega} = \langle b \rangle^2 \sum_{i,j} e^{-i\vec{q} \cdot (\vec{R}_i - \vec{R}_j)} + \underbrace{(\langle b^2 \rangle - \langle b \rangle^2) N}_{\text{Incoherent Scattering}}.$$
(1.20)

Here the coherent scattering part is the direction of q dependent. But, the incoherent scattering part is uniform in all directions. In the scattering system, N is the total number of atoms. The structure factor or correlations of atomic positions is measured by coherent elastic scattering. In the process of inelastic neutron scattering, neutrons can also gain or lose energy. Atomic motions are determined by the inelastic neutron scattering process.

Magnetic neutron scattering occurs due to a neutron scatters from magnetic atoms or molecules. Magnetic neutron scattering couples to fluctuations in magnetization density [41]. In neutron scattering, the short-distance and short-time behavior are measured. One of the most crucial methods for determining microstructure is small-angle neutron scattering, which is used in a broad range of scientific areas, such as materials science, physics, chemistry, and biology.

1.3 Theory for Particle Scattering

1.3.1 Classical Scattering Theory

The scattering cross section identifies the characteristics of both quantum and classical scattering. Assume a particle collides with a scattering target. Let us consider an incoming particle with energy E and impact parameter b exits at a particular scattering angle θ -see figure 1.6. For simplicity, we assume that the target is azimuthally symmetric, keeps the trajectory in one plane, and the target is heavy. We can therefore ignore the recoil effect. In classical mechanics, the impact parameter $b(\theta)$ determines the scattering angle for a central potential $V(\vec{r})$. Of course, generally, the scattering angle increases with decreasing the impact parameter. Let us consider a collision experiment where a detector counts the number of particles per unit time, $Nd\Omega$ that are scattered into an element of solid angle $d\Omega$ in the direction (θ, ϕ) per unit time. The differential cross section is used to describe the angular distribu-

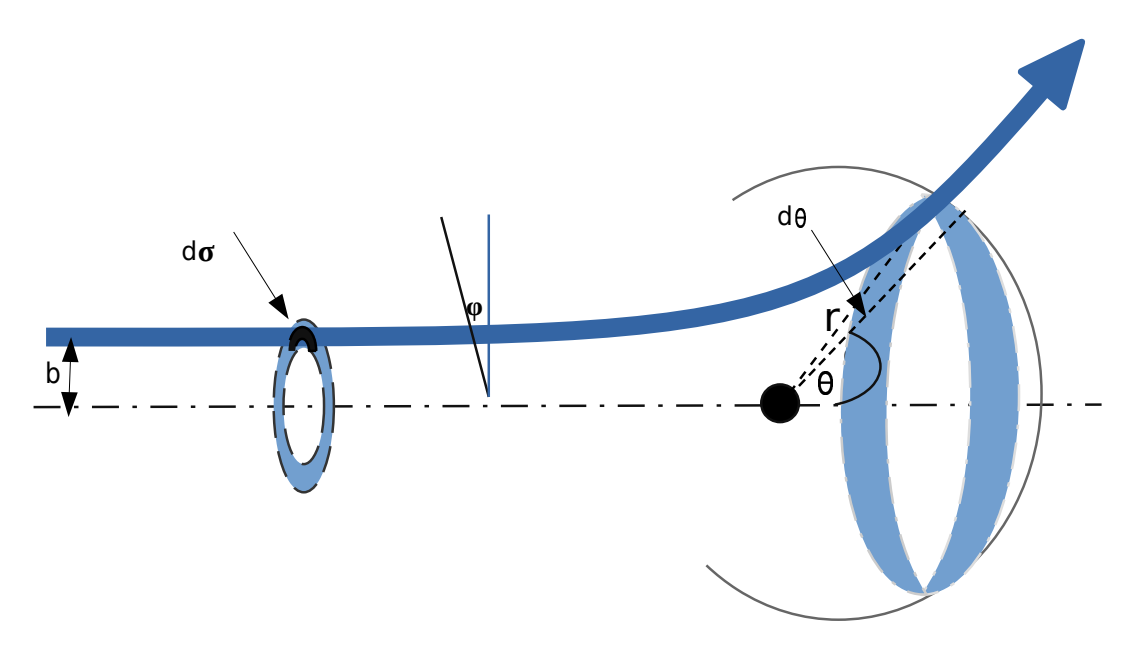


Figure 1.6: The incoming particles incident in an elementary area $d\sigma$ and scatter into the elementary solid angle $d\Omega$

tion of scattered particles in a particular process. From the figure 1.6 it is clear that between b and b+db the number of incident particles per unit time is equal to the number of particles per unit time between $\theta+d\theta$ that are scattered. The number of particles scattered into the solid angle $d\Omega$ per unit time for incident flux (J_{in}) is given by $Nd\Omega = N \sin\theta d\phi d\phi = J_{in}bdbd\phi = J_{in}d\sigma$. Therefore, we have

$$D(\theta) = \frac{d\sigma}{d\Omega} = \frac{b}{\sin \theta} \left| \frac{db}{d\theta} \right|. \tag{1.21}$$

For classical Coulomb scattering $V(r) = \frac{\kappa}{r}$. In this case, we get the Rutherford formula [39]

$$D(\theta) = \frac{\kappa^2}{16E^2} \frac{1}{\sin^4 \frac{\theta}{2}}.$$
 (1.22)

Therefore, the Rutherford scattering cross-section depends on the scattering angle and the velocity of the incoming particles. The form of the scattering intensity is the same for the repulsive force as it is for an attractive one, since it is unaffected by the sign of the charge.

How does the overall cross-section look for Rutherford scattering? The differential cross-section Eqn. (1.22) has an unusual characteristics in that the associated total cross-section is infinite. Because the Coulomb force's infinite range is responsible for this result. A key point to note that the classical derivation and the quantum-mechanical treatment of Coulomb scattering gives the same outcome.

1.3.2 Quantum Scattering Theory

The collision or interaction of two particle are treated by viewing an incoming particle that scatters off a second particle and propagates as measured by the nature of

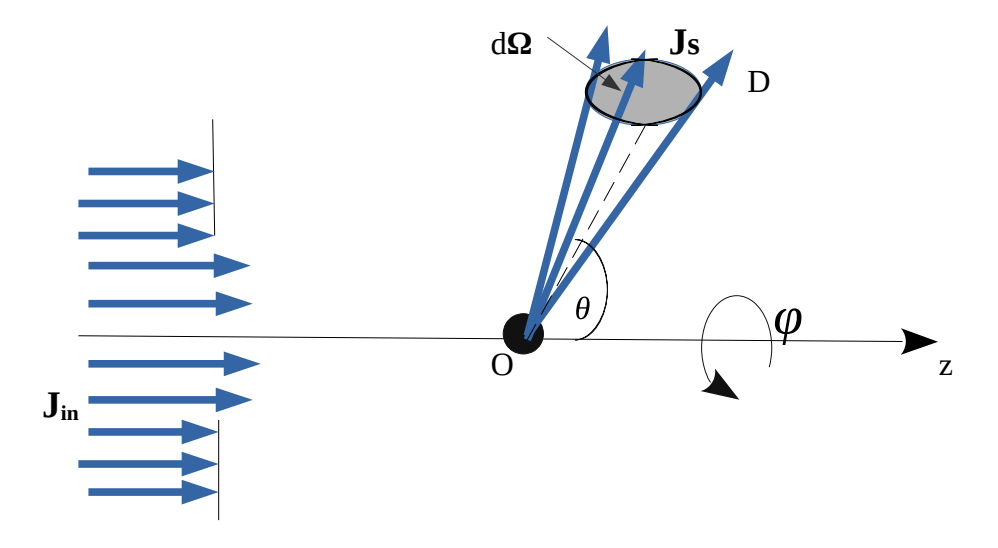


FIGURE 1.7: The basic setup is a flux of incident particles with uniform energies that are scattered from the target and captured by detectors that measure deflection angles.

the potential and the incoming particle. We use the transformation to the center of the mass frame because we are dealing with the two-particle problem. The original problem is now reduced to a single particle traveling in a target potential $V(\vec{r})$. The scattering information is carried by the wave function for the particle's relative motion. Perhaps one of the simplest examples of 3D scattering is scattering by a spherical potential. In this case, the scattering potential $V(\vec{r})$ is fully dependent on the separation between the target and the particle. The spatial representation of the time-independent Schrödinger equation looks like

$$\frac{\hbar^2}{2m}\nabla^2\Psi(\vec{r}) + [E - V(\vec{r})]\Psi(\vec{r}) = 0.$$
 (1.23)

It is useful to take class of potentials that diminish when r > a. Or, at least become insignificant in comparison to the centrifugal potential $\frac{\hbar^2 l(l+1)}{2mr^2}$. In quantum scattering theory, we imagine that an incoming plane wave $\Psi(z) = e^{ikz}$ propagates along the z-direction, collides with some localized target, and then produces an outgoing spherical wave. The solution to the Schrödinger Eqn. (1.23) can be written as [39]

$$\Psi \simeq e^{ikz} + f(\theta, \phi) \frac{e^{ikr}}{r},$$
 for large r . (1.24)

Scattering Cross-section

The energy of the incident particle $E = \frac{\hbar^2 k^2}{2m}$ while the uniform flux is given by

$$\vec{J_{in}} = -i\frac{\hbar}{2m}(\Psi^*\nabla\Psi - \Psi\nabla\Psi^*) = \frac{\hbar\vec{k}}{m}.$$
 (1.25)

The asymptotic form of the outgoing spherical wave at large distance r is $f(\theta, \phi) \frac{e^{ikr}}{r}$. Particle flux associated with scattered particle in the (θ, ϕ) direction is given by

$$\vec{J_{out}} = \frac{\hbar}{m} Im(\Psi_s^* \frac{\partial \Psi_s}{\partial r}) \hat{e_r} = \frac{\hbar}{m} \frac{|f(\theta, \phi)|^2}{r^2} \hat{e_r}.$$
 (1.26)

The particle flux crosses the area $dA = r^2 d\Omega$ which subtends an elementary solid angle $d\Omega$ at the centre of the target is given by

$$Nd\Omega = \frac{\hbar}{m} \frac{|f(\theta, \phi)|^2}{r^2} r^2 d\Omega. \tag{1.27}$$

Again $Nd\Omega = J_s dA = J_{in} d\sigma$. Hence, we get the differential cross section

$$\frac{d\sigma}{d\Omega} = |f(\theta, \phi)|^2. \tag{1.28}$$

This expression is significant because the fluxes J_s and J_{in} are measurable quantities and can be determined theoretically.

Fermi-Huang Potential

An usable short-range Fermi-Huang potential [42] in three dimensions can be defined as

$$<\vec{r}|V_{HF}|\Psi>=g\delta^3(\vec{r})\Psi_{reg}(\vec{r})$$
 (1.29)

where $\Psi_{reg} = \frac{d}{dr}(r\Psi(\vec{r}))$. This potential is also known as a "regularized delta potential". Now we expand $\Psi(\vec{r})$ in power of r, starting with r^{-1}

$$\Psi(\vec{r}) = C_1(\theta, \phi) \frac{1}{r} + C_0(\theta, \phi) + C_1(\theta, \phi)r + \dots$$
 (1.30)

Thus we have,

$$\Psi_{reg} = \frac{d}{dr}(r\Psi(\vec{r})) = C_0(\theta, \phi) + 2C_1(\theta, \phi)r + \dots$$
(1.31)

The Eqn. (1.31) shows that due to the effect of regularization operator the singularity is removed. Thus, $\Psi_{reg}(\vec{r})$ has always non-singular behavior at $\vec{r}=0$. Using the shifting properties of delta function Eqn. (1.29) will give

$$\langle \vec{r}|V_{HF}|\Psi\rangle = g\delta^3(\vec{r})\Psi(0).$$
 (1.32)

Lippman- Schwinger Equation

To describe the scattering theory, let us take an incident particle state $|\Psi_0\rangle$, is scattered by the interacting potential V, resulting in a scattered state is $|\Psi_s\rangle$. The incident

state $|\Psi_0\rangle$ is considered to be an eigenstate of the free particle (with V=0). Hamiltonian or 'background' Hamiltonian H_0 with eigenvalue E. This is written mathematically as

$$(E - H_0)|\Psi_0\rangle = 0 \tag{1.33}$$

where H_0 is free particle Hamiltonian with incident state is $\Psi(\vec{r}) = e^{i\vec{k}.\vec{r}}$. For asymptotic case $(r \to \infty)$, the eigenvectors are determined by

$$(E - H_0)|\Psi\rangle = V|\Psi\rangle \tag{1.34}$$

where we take E > 0 and $|\Psi\rangle$ is the eigenstate of the total Hamiltonian $H = H_0 + V$ with eigenvalue E. Using Eqn. (1.33) and Eqn. (1.34) the Lippmann-Schwinger equation can be obtained as

$$|\Psi\rangle = |\Psi_0\rangle + G_0(E)V|\Psi\rangle \tag{1.35}$$

where the symbol G_0 is known as unperturbed Green's function, defined as $G_0 = \lim_{\epsilon \to 0} \frac{1}{(E-V+i\epsilon)}$. The small parameter ϵ is inserted to resolve the singularity in the operator $G_0(E)$. If we choose the boundary condition $\frac{1}{E-H_0-i\epsilon}$, the second term can be produced by the starting from infinity and convergent at the origin. Thus, it is practically impossible to arrange. An alternative form of Eqn. (1.35) can be expressed as

$$|\Psi\rangle = (1 - G_0(E)V)^{-1}|\Psi_0\rangle.$$
 (1.36)

Now we are trying to understand the meaning of this solution in the next section.

Born Series

The iteration approach can be used to solve the Lippmann-Schwinger equation. To solve Eqn. (1.36) by using the iteration method, we first rewrite the equation as

$$|\Psi_{new}\rangle = |\Psi_0\rangle + G_0(E)V|\Psi_{old}\rangle. \tag{1.37}$$

For zero-order approximation $|\Psi_{new}\rangle = |\Psi_0\rangle$. Thus, Eqn. (1.37) can rewrite as $|\Psi_{new}\rangle = (1 + G_0(E)V)|\Psi_0\rangle$. After successive number of iterations, the whole equation leading to the Born series:

$$|\Psi\rangle = (1 + G_0(E)V + G_0(E)VG_0(E)V + G_0(E)VG_0(E)VG_0(E)V + \dots)|\Psi_0\rangle$$

=
$$\sum_{n=0}^{\infty} (G_0(E)V)^n |\Psi_0\rangle.$$
 (1.38)

Eqn. (1.38) leads to an infinite series with increasing powers of the interaction potential $V(\vec{r})$. Physically Eqn. (1.38) represents from the potential the incident particle is

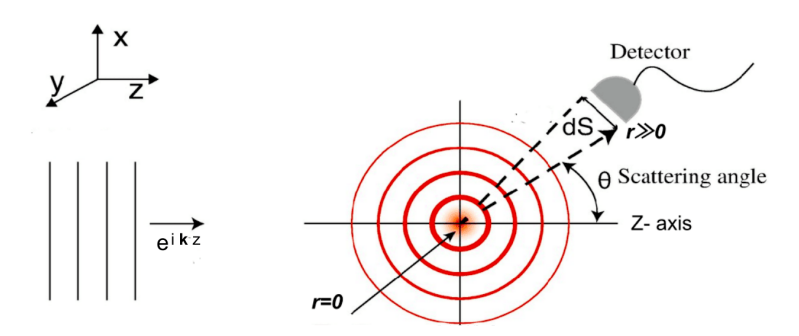


FIGURE 1.8: The Schrödinger equation has a solution that is the sum of the incident plane wave e^{ikz} and the wave scattered by the potential propagating outward from r=0 in the quantum mechanical description of low-energy scattering. That is, the wave function in the form $\Psi \simeq e^{ikz} + f(\theta,\phi)e^{ikr}/r$. This is an eigenstate with energy $E = \hbar^2 k^2/m$ (no energy loss due to elastic scattering). Only the amplitude of the scattering is $f(\theta,\phi)$ which depends on the scattering potential V(r).

subjected to a series of numerous scattering events. The position representation of Lippmann-Schwinger Eqn. (1.37) can be expressed as [39]

$$\Psi(\vec{r}) = \Psi_0(\vec{r}) + \int d^3 \vec{r'} G_0(\vec{r}, \vec{r'}, E) V(\vec{r'}) \Psi(\vec{r'}). \tag{1.39}$$

In this approximation, Eqn. (1.39) leads to an expansion first order in V. The n-th order approximation for the wave function can be obtained by analogy to Eqn. (1.38). At zeroth order in $V(\vec{r})$, scattering wave function translates to an unperturbed incoming plane wave. The Green function in position representation in free space the Eqn. (1.39) is given by [39]

$$G_{0}(\vec{r}, \vec{r'}, E) = \langle \vec{r} | (E - H_{0} + i0)^{-1} | \vec{r'} \rangle$$

$$= -\frac{2m}{\hbar^{2}} \frac{e^{ik|\vec{r} - \vec{r'}|}}{4\pi |\vec{r} - \vec{r'}|}.$$
(1.40)

This represents the outgoing spherical wave function. If we consider the center of the scattering potential is at the origin and if the detector is sufficiently large distances from the scatterer. For a spherically symmetric potential, behavior of $\Psi(\vec{r})$ at very large distances, one can write

$$\Psi(\vec{r}) \simeq_{\lim_{r \to \infty}} e^{i\vec{k}\cdot\vec{r}} + f(\theta, \phi) \frac{e^{i\vec{k}\cdot\vec{r}}}{r}.$$
 (1.41)

The incoming plane wave is represented by the first term while the departing spherical wave is represented by the second term (see figure 1.8). The scattering amplitude depends on the incident particle momentum \vec{k} and the angle of scattering between the incoming particle and the direction of observation, which contains all of the information. The factor $f(\theta, \phi)$ can be expressed as [39]

$$f(\theta,\phi) = -\frac{2m}{4\pi\hbar^2} \int d^3\vec{r'} e^{-i\vec{k}\cdot\vec{r'}} V(\vec{r'}) \Psi(\vec{r'})$$
 (1.42)

where $f(\theta,\phi)$ has a dimension of length. The scattering amplitude is independent of the distance \vec{r} . Here, $\vec{r'}$ represents the target size and \vec{r} is the distance between the target and the detector. In the above approximation valid for r >> r'. Thus, $|\vec{r} - \vec{r'}| \simeq r$ [39]. The scattered particle state is $|\Psi_s\rangle = |\Psi\rangle - |\Psi_0\rangle$. The T- matrix or transition matrix is defined as

$$|\Psi_{s}\rangle = G_{0}(E)T|\Psi_{0}\rangle$$

$$= G_{0}(E)(V + VG_{0}(E)V + VG_{0}(E)VG_{0}(E)V + \dots)|\Psi_{0}\rangle$$

$$= G_{0}(E)V(1 - G_{0}(E)V)^{-1}||\Psi_{0}\rangle.$$
(1.43)

Thus, the final form of T- matrix is

$$T = V(1 - G_0(E)V)^{-1}$$

= $V + VG_0(E)V + VG_0(E)VG_0(E)V + \dots$ (1.44)

Now we want to show the transition matrix (T-matrix) for the Fermi-Huang potential

$$\langle \vec{r} | T | \Psi \rangle = g \delta^{3}(\vec{r}) \Psi_{reg}(0) \left[1 + G_{0,reg}(0,0)g + \frac{d}{dr} r G_{0}(\vec{r},0) G_{0,reg}(0,0)g^{2} + \dots \right]$$

$$= g \delta^{3}(\vec{r}) \Psi_{reg}(0) \left[1 + G_{0,reg}(0,0)g + G_{0,reg}^{2}(0,0)g^{2} \right]$$

$$= \frac{g \delta^{3}(\vec{r}) \Psi_{reg}(0)}{1 - i G_{0,reg}(0,0)g}$$
(1.45)

where $G_0(\vec{r},0) = -\frac{m}{2\pi\hbar^2}[r^{-1} + ik - \frac{k^2r}{2} + \dots]$. Thus, $G_{0,reg}(0,0) = -\frac{m}{2\pi\hbar^2}ik = -ik\frac{m}{2\pi\hbar^2}$. Finally T- matrix we have

$$T = \frac{V_{HF}}{1 + i\frac{m}{2\pi\hbar^2}k} \tag{1.46}$$

where $g' = \frac{g}{1+ik\frac{m}{2\pi\hbar^2}}$, g' is known as 're-normalized' coupling constant. The scattering amplitude in term of T- matrix is defined as

$$f(\vec{k'}, \vec{k}) = -\frac{m}{2\pi\hbar^2} \int d^3\vec{r} d^3\vec{r'} e^{-i\vec{k'}\cdot\vec{r'}} T(\vec{r}, \vec{r'}) e^{-i\vec{k}\cdot\vec{r}}$$

$$= -\frac{(2\pi)^2 m}{\hbar^2} \langle \vec{k'} | T | \vec{k} \rangle$$
(1.47)

where the initial and final relative momenta of the colliding particle are \vec{k} , $\vec{k'}$. If we take the Fermi-Huang potential as an interacting potential, then the scattering amplitude can be expressed as [43]

$$f(\vec{k'}, \vec{k}) = f(\theta, \phi) = -\frac{\frac{m}{2\pi\hbar^2}}{1 + i\frac{m}{2\pi\hbar^2}k}.$$
 (1.48)

The amplitude of scattering is independent on the direction of scattering, as shown by the above calculation. So, whatever the modulus k is, the Fermi-Huang potential scatters only in the s -wave. The scattering amplitude at low momentum converges to a constant value known as the s-wave scattering length if we analyze the potential from a short-ranged central potential. We can relate this important parameter in terms of the T-matrix as $a_s = -\lim_{k \to 0} f(\theta, \phi) = \lim_{k=k' \to 0} \frac{m}{2\pi\hbar^2} f(\vec{k'}, \vec{k}) = \frac{m}{2\pi\hbar^2}$. The scattering amplitude at low energies is constant at $f \propto Y_{0,0}$ and the condition $ka_s << 1$ is satisfied, in the interaction region, the phases kz and kr are negligible. Therefore, $\Psi \simeq 1 + f/r$. From Eqn. (1.46), we can determine the scattering cross-section and its angular dependency:

$$\frac{d\sigma}{d\Omega} = |f(\vec{k'}, \vec{k})|^2 = |f(\theta, \phi)|^2. \tag{1.49}$$

Eqn. (1.49) represents the probability of scattering per unit solid angle at an angle between the wave vector $\vec{k'}$ and \vec{k} . We explain the quantum scattering for distinguishable particles. The varied internal states of alkali atoms are caused by couplings of nuclear and electronic spins which are referred to as atomic hyperfine states. We assume there are two identical particles which mean they can occupy the same hyperfine states. For fermions or bosons particle, we must then take antisymmetrize or symmetrize the wave function according to the total atomic spin. The differential cross section for both types of particle can be written as[39]

$$\frac{d\sigma}{d\Omega} = |f(\theta) \mp f(\pi - \theta)|^2 \tag{1.50}$$

where the minus and plus signs indicates fermions and bosons respectively. The determination of the scattering cross-section has been an essential tool in the physics community. In the high-energy physics area, scattering experiments give us information about the size of the particle and the interaction strength. In condensed matter physics, neutron scattering and X-ray scattering off materials reveal the crystal structure of bulk material.

Are the conditions for Born approximation experimentally satisfy?

The Born approximation's validity condition is $k|a_s| \ll 1$. For scattering state one requires $r \gg a_s$. Now $r = \rho^{-\frac{1}{3}}$ be the mean distance between the particles, where ρ is density of the gas. Thus, the Born approximation is valid when $\rho^{\frac{1}{3}}|a_s| \ll 1$. At a temperature of $T = 1\mu K$, we use an average of the k^2 atoms in the Maxwell-Boltzmann distribution which is often greater than the critical temperature for alkali gases to determine the order of magnitude of k. The average yields a root mean square for k equal to $\Delta k = \sqrt{\frac{3mk_BT}{2\hbar^2}}$. Scattering length for k0 atoms is k0 atoms obtain k0 atoms k0 atoms case scattering length k1 atoms. Thus, we obtain k0 atoms. First, measured experimentally at JILA for k1 atoms. Let

us now discuss the second case. Condensates reach when densities of the order of 2×10^{14} atoms per cubic centimeter. When the scattering length of 23 Na atoms is specified $\rho^{1/3}a_s=0.015\ll 1$. This results for the specified scattering length of 87 Rb atoms $\rho^{1/3}a_s=0.034\ll 1$.

Partial wave analysis of quantum scattering

At the low energy limit, the analysis of the scattering problem can be used by the method of partial wave expansion. If the scattering potential $V(\vec{r})$ is zero, then the unique solution (plane wave) would be expressed in term of spherical wave using the Rayleigh formula. Therefore,

$$\Psi(r) = e^{ikz} = \sum_{l} (2l+1)i^{l} j_{l}(kr) P_{l}(\cos \theta)$$
 (1.51)

where P_l is a Legendre polynomial, $k = \sqrt{\frac{2mE}{\hbar^2}}$ and j_l is a spherical Bessel function. The total wave function (i.e, solution of the Schrödinger Eqn.(1.23)) outside of the potential range takes the following form

$$\Psi(r) = e^{ikz} + f(k,\theta) \frac{e^{ikr}}{r}$$
(1.52)

where the scattering amplitude $f(k,\theta)$ for the spherical symmetric potential. The system is symmetric (rotationally invariant) about the z-axis because $V(\vec{r})$ is central. Therefore, the azimuthal quantum number m=0, the scattered wave function cannot depend on the azimuthal angle. The complete solution of Eqn. (1.23) is as follows [39]

$$\Psi(r) = \sum_{l} a_{l} R_{l}(kr) P_{l}(\cos \theta)$$
 (1.53)

where the partial wave equation is satisfied by the radial function $R_l(r)$. Now the radial form of the Schrödinger equation can be written as using Eqn. (1.53) in Eqn. (1.23)

$$\frac{\hbar^2}{2m} \frac{1}{r^2} \frac{d}{dr} r^2 \frac{d}{dr} R_l(r) + \left[E - V(r) - \frac{\hbar^2}{2m} \frac{l(l+1)}{r^2}\right] R_l(r) = 0.$$
 (1.54)

Now V(r) = 0 when r > a, the linear combination of the spherical Bessel functions $j_l(kr)$ and $n_l(kr)$, which represents the solution of Eqn. (1.54). In the limit $kr \to \infty$, the asymptotic forms of the spherical Bessel functions are [39]

$$j_l(kr) \to \frac{\sin(kr - \frac{\pi l}{2})}{kr}, \quad n_l(kr) \to -\frac{\cos(kr - \frac{\pi l}{2})}{kr}.$$
 (1.55)

Therefore, using the Eqn. (1.55), the radial from can be written as

$$R_l(r) o rac{\sin(kr - rac{\pi l}{2} + \delta_l)}{kr}.$$
 (1.56)

Because of the phase shifts δ_l , this wave function is referred to distorted plane wave. The radial function of Eqn. (1.56) is finite at r=0 with $\delta_l=0$ as $R_l(r)$ in Eqn. (1.55) simplifies to $j_l(kr)$. In the absence of the scattering potential (i.e., V=0), δ_l is a real angle that diminishes for all values of l, δ_l is also known as the phase shift of the l-th partial wave. The series Eqns. (1.51) and (1.53) are inserted in an Eqn. (1.52), and replace the Bessel functions at $kr \to \infty$ limit, giving us

$$\sum_{l} a_{l} \frac{\sin(kr - \frac{\pi l}{2} + \delta_{l})}{kr} P_{l}(\cos \theta) = \sum_{l} (2l + 1)i^{l} \frac{\sin(kr - \frac{\pi l}{2})}{kr} P_{l}(\cos \theta) + \frac{f(k, \theta)e^{ikr}}{r}.$$
(1.57)

One can obtain by applying the formula $\sin y = \frac{e^{iy} - e^{-iy}}{2i}$ and matching the coefficients of e^{-ikr} in the equation above

$$a_l = (2l+1)i^l e^{i\delta_l}. (1.58)$$

Putting a_l in place of Eqn. (1.53) and comparing the coefficient of $\frac{e^{ikr}}{r}$, Eqn. (1.57) we have

$$f(k,\theta) = \sum_{l} (2l+1) f_{l}(k) P_{l}(\cos(\theta))$$
 (1.59)

where l is the value of angular momentum of the scattering particle. In the asymptotic limit, we can obtain partial amplitude

$$f_l(k) = \frac{1}{k} e^{i\delta_l(k)} \sin \delta_l(k) = \frac{1}{k(\cot \delta_l - i)}.$$
 (1.60)

The scattering amplitude $f(k,\theta)$ is written as a superposition of Legendre polynomials. In ultracold gases, the scattering energies are very low. Then the scattering occurs only due to the s-wave (l=0) momentum states. The scattering amplitude in this low energy limit is explained by the resulting s-wave phase shift δ_0 . Now the scattering amplitude can be obtained by expanding the cot term in the above equation via the effective range expansion

$$f_s(k) = \frac{1}{(-ik + \frac{1}{2}R_0k^2 - \frac{1}{a_s})}$$
 (1.61)

where $k \cot \delta_0(k) \approx -\frac{1}{a_s} + \frac{1}{2}R_0k^2$. From the cot expansion at very low energy one can determine the s-wave scattering length a_s and effective range R_0 of the potential. These terms represent the effective size of the scatterer from the asymptotic limit.

The elastic cross-section for identical boson is given precisely in terms of a(k) is given by

$$\sigma_e(k) = \frac{8\pi a^2}{(1 + a^2 k^2)}. (1.62)$$

The additional factor of 2 emerges as a result of constructive interactions of bosons, which increases scattering.

To determine the implicit formula for the l-wave scattering length a_l . Let us examine the analytic properties of $f_l(k)$ for small k as

$$f_l(k) \simeq -\frac{2m}{\hbar^2} \int dr V(r) [rj_l(kr)]^2$$
 (1.63)

$$= -\frac{2m}{\hbar^2} \int dr V(r) r^2 \left[\frac{(kr)^l}{(2l+1)!!} (1 + \mathcal{O}([k^2 r^2])) \right]^2.$$
 (1.64)

By switching the limits and assuming uniform convergence, it is possible to arrive at the general momentum dependency $f_l(k) = \mathcal{O}(k^{2l})$ as $k \to 0$. One can reformulate this in terms of phase shifts by using the formula $f_l(k) \sim \frac{1}{k \cot \delta_l(k)}$. Finally, that leads to

$$k^{2l+1}\cot\delta_l(k) = -a_l^{-(2l+1)} + \frac{1}{2}R_l^2k^2 + \mathcal{O}(k^4), \qquad a_l \neq 0$$
 (1.65)

or

$$\frac{\tan \delta_l(k)}{k^{2l+1}} = -a_l^{-(2l+1)} + \mathcal{O}(k^2). \tag{1.66}$$

For the l-wave scattering length a_l , it provides an implicit definition and the effective range R_l . The amplitude does not vanish at low energies except for s-wave scattering (l = 0). No matter the shape of the potential, a_s is the only important parameter in that limit.

1.4 The scattering length

A crucial characteristic of ultra-low-energy collisions is that despite of the attractive interacting potential between two atoms in the figure 1.9. The total effect is identical to that of the hard-sphere potential scattering. The cold atomic cloud can be modeled as a hard-sphere gas, especially for calculating the energy contribution to the gas from interactions between atoms. An atomic collision happens in the center-of-mass frame. The scattering happens from potential V(r) of a particle with a reduced mass can be written as

$$\mu' = \frac{mM}{m+M}. ag{1.67}$$

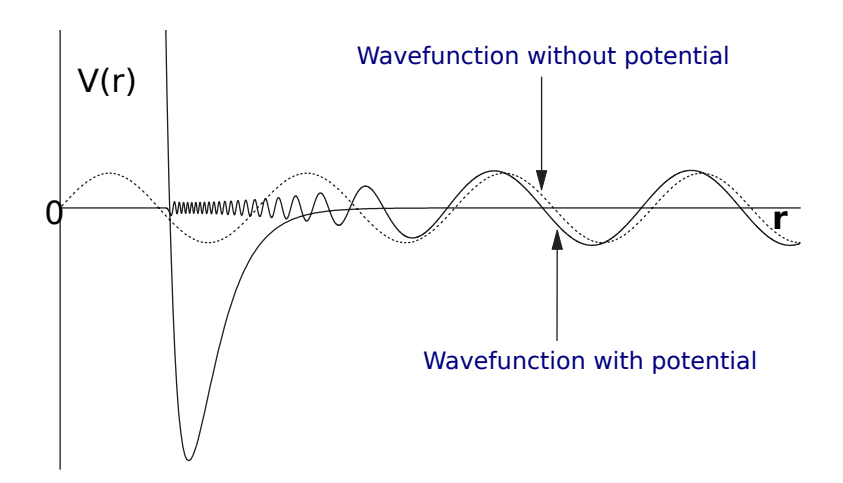


FIGURE 1.9: The radial wavefunction is $= sin(kr - \Phi)$ and the phase shift is produced by the same scattering as a hard-sphere potential. When the distance is very large, the overall effect of each potential on the scattered wave function has a phase shift (indicated by the dashed line for waves spread from a point- object at r = 0). The equivalent hard-sphere potential radius a_s can be applied to characterize the potential. Greenhow extended computational techniques to the study of quantum scattering (1990). Figure from Butcher et al. al (1999).

When two atoms collide in a gas of identical particles, their reduced mass becomes $\mu' = m/2$ because they have the same mass, m = M = m. In the short range, where $sin(k(r-R)) \approx k(rR)$, the radial solution can be written as

$$\frac{\Psi(r)}{r} \propto 1 - \frac{R}{r} = 1 - \frac{a_s}{r}.$$
 (1.68)

It shows the general form of the low-energy wavefunction ($ka_s \ll 1$) near the hard-sphere ($a_s < r \ll \frac{\lambda_{dB}}{2\pi}$ region). Here, l=0. Use eigenstates in the expression (1.68) with amplitude η , we can calculate the average of the kinetic energy $-\frac{\hbar^2}{2\mu'}\nabla^2$ with $\mu'=m/2$, is given by [45]

$$E_{K.E} = -\frac{4\pi\hbar^2}{m} |\eta|^2 \int_{a_s}^{\infty} |\frac{d}{dr} (1 - \frac{a_s}{r})|^2 r^2 dr = \frac{4\pi\hbar^2 a_s}{m} |\beta|^2.$$
 (1.69)

A reasonable estimate of the energy is obtained by assuming an infinite upper bound on the integral of r (please see, Pathra et al. 1971). Pitaevskii and Stringari (2003) book [9] provides a brief description of different aspects of collisions among ultracold bosons associated with BEC. This reference gives a more details definition of the scattering length and also provides an brief explanation of positive ($a_s > 0$) or negative ($a_s < 0$) (see 1.10) scattering length. When $a_s > 0$, the interaction between hard spheres is effectively repulsive. For $a_s < 0$ this is the case for attractive hard-sphere interactions. However, most Bose-Einstein condensation experiments use sodium and rubidium atomic states with positive scattering lengths corresponding to strong

¹Both classical and quantum physics use the reduced mass and the transformation to the centre of mass frame in very similar ways.

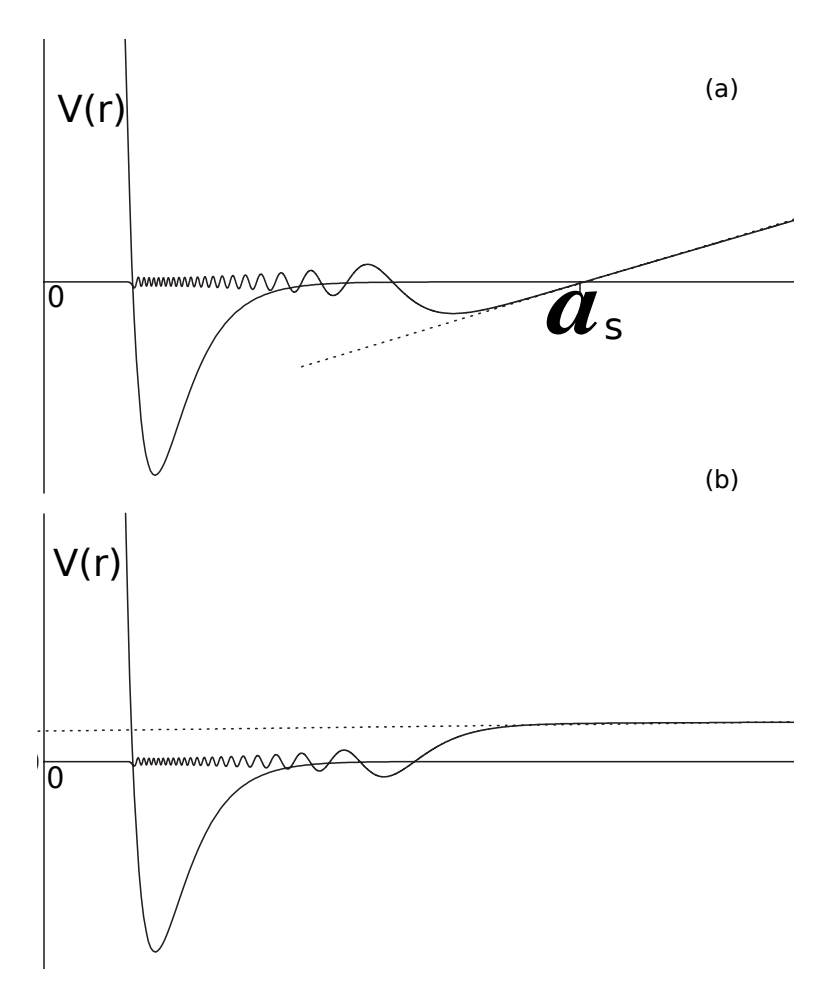


FIGURE 1.10: Radial wave functions for molecular potentials with slightly different very low-energy scattering from a) large positive and b) negative scattering lengths (see Butcher et al. (1999)). The dashed line crosses the horizontal axis at $r=a_s$ representing the extrapolation of the wavefunction for large r.

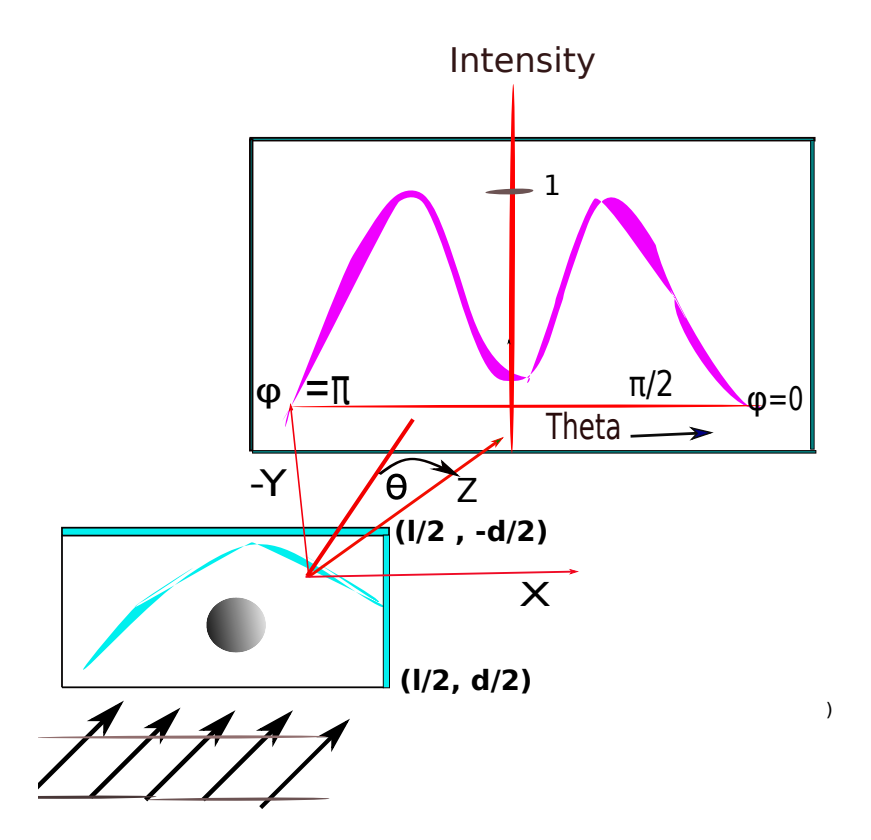


FIGURE 1.11: Intensity distribution for a 'particle' scattering (e^{ikz}) by a quantum scatterer in 2-D box.

repulsive interactions between hard spheres.

1.5 Quantum scattering for unfixed scatterers in a box geometry

We will now discuss the brief review of quantum scattering for unfixed scatterers in a box geometry which is studied by Ankita Bhattachrya *et al*, (2017) [44]. The incident particle is considered to propagate in the z-direction. One can express the interaction between the incident particle and scatterers by a short-range Fermi-Huang potential $g\delta_p^3(\vec{r})$. We will look at two spatial scenarios: The scatters move in a one-dimensional box geometry. So, the possible position of the scatterers is $(-l/2 < x_0 < l/2)$ along the x-axis. The interaction between the incident particle and the scatters along the x-axis can be written as

$$V_{in} = g\delta_p^3(\vec{r} - x_0\hat{i}) \tag{1.70}$$

where \vec{r} is the position of the incident particle and x_0 is the position of the scatterers. Due to these interactions, the particle would scatter coherently from all possible points with probability density $|\Psi n^{(p)}(x_0)|^2$. The normalised energy eigenstate of

the scatterer is

$$\Psi^p(x_0) = \sqrt{2/l} \cos \frac{n\pi x_0}{l} \tag{1.71}$$

for n = 1, 3, 5...., and

$$\Psi^p(x_0) = \sqrt{2/l} \sin \frac{n\pi x_0}{l} \tag{1.72}$$

for even n=2,4,6... All outgoing spherical waves interfere with different phases, resulting in coherent scattering amplitude. Now scattering amplitude depends on the scatterer's quantum state in a given direction (θ,ϕ) at the large distance $\mathbf{x_0}+\mathbf{r}$ from the scattering center. The interaction between the incident particle and scatterer is given by the Fermi-Huang potential. Using the Eqn. (1.70), particle scattering amplitude for the single scatter in the quantum state $|\Psi_n^p(\mathbf{x_0})\rangle$ can be written as

$$f_n^p(\theta,\phi) = -\frac{mg_k}{2\pi\hbar^2} \int_{-l/2}^{l/2} e^{-i\vec{k}\cdot x_0\hat{i}} |\Psi_n^p(x_0)|^2 dx_0$$

$$= -\frac{mg_k}{2\pi\hbar^2} \operatorname{sinc}(q_x l) \frac{1}{1 - (\frac{q_x l}{n\pi})^2}$$
(1.73)

where $q_x = k \sin(\theta) \cos(\phi)/2$. For $l \to 0$, the scatterer should be fixed. For classical fixed scatters one can get

$$f_n^p(\theta,\phi) = -\frac{mg_k}{2\pi\hbar^2}. (1.74)$$

Additionally, the aperture will contribute to quantum scattering. This is due to the fact that a particle can be scattered when an incident occurs on an empty box. The Fresnel-Kirchoff formula will give the eigenstate in this situation

$$\Psi^{p} \approx \frac{-Aik}{2\pi} \frac{(1+\cos\theta)}{2} \frac{e^{ikr}}{r} \int e^{i(k_{x}x_{0}+k_{y}y_{0})} dx_{0} dy_{0}. \tag{1.75}$$

The scattering amplitude for a rectangular aperture $(-\frac{l}{2} < x_0 < \frac{l}{2}, -\frac{l}{2} < y_0 < \frac{l}{2})$ of area A = l d can be obtained as

$$f^{a}(\theta,\phi) = e^{-i\frac{\pi}{2}} \frac{Aik(1+\cos\theta)}{4\pi} sinc(q_{x}l) sinc(q_{y}l)$$
(1.76)

where $q_y = k \sin \theta \sin \phi$. The solution shown above is for a rectangular 2-D aperture, but by assuming a few conditions l/d << 1, k d>> 1, and A = d l non zero finite constant. Then we can get the same result in 1-D. Since d k >> 1 now, $\mathrm{sinc}(q d) \to 0$ except for $\phi = 0$ and $\phi = \pi$ which results in $\mathrm{sinc}(q d) = 1$. The scattering amplitude can therefore be written as

$$f^{a}(\theta,\phi) = e^{-i\frac{\pi}{2}} \frac{Aik(1+\cos\theta)}{4\pi} sinc(q_{x}l)(\delta_{\phi,0} + \delta_{\phi,\pi}). \tag{1.77}$$

Adding Eqns. (1.74) and (1.77) give the total scattering amplitude for 1D box. The significance of the above result increases with temperature, where the amplitude of a diffraction maximum at $\theta = 0$ can also decrease due to the completion between particle scattering and aperture scattering. The figure 1.11 shows the intensity profile of the scattered particle in a 2-D box.

1.6 Ultracold Gas

Atoms stored at temperatures below ten microkelvins (μk) near absolute zero are called ultracold atoms. At these temperatures, the quantum mechanical properties of the atom come into play. Achieving such low temperatures usually requires a combination of techniques. First, the atoms are usually trapped in a magneto-optical trap and precooled by laser cooling. Further cooling is done by evaporative cooling in a magnetic or optical trap to achieve the lowest possible temperature. Quantum magnetism, Bose-Einstein condensation (BEC), quantum phase transitions, boson superfluidity, Efimov states, many-body spin dynamics, Bardeen-Cooper-Schrieffer (BCS) superfluidity and BEC-BCS crossover are only a small part of the phenomena studied in experiments with ultracold atoms. Ultracold atomic systems have been used as quantum simulators in some of these research directions to study the physics of other systems, e.g., unitary Fermi gas and the Ising and Hubbard models. Quantum computers can also be built with ultracold atoms.

1.7 Properties of scatterers

At the microscopic quantum level, there are two types of scatterers: Fermi scatter and Bose scatter, which differ in their intrinsic angular momentum, the spin. Bose scatterers behave like bosonic particles, while Fermi scatterers behave like fermionic particles. According to Pauli's exclusion principle, there is only one electron in each of the quantum mechanical states of the atom. The shells fill up while we add electrons. As a result, each electron requires a particular spatial volume. Without interaction, the fermions continuously fill the lowest quantum states of the trap, eventually reaching the Fermi energy level and producing a degenerate Fermi gas. The spin statistics theorem states that bosons are particles with integer spins, while fermions are particles with half-integer spins. When identical particles grow so close to each other that their wave packets overlap, their distinct characteristics become visible. At low temperature, bosons tend to congregate in the same state, whereas fermions repel one another. Bosons contained in a trap experience a phase shift at very low temperatures, here all the particles condense into a single macroscopic matter wave, the Bose-Einstein Condensation (BEC). The BEC is a purely statistical quantum phenomenon in which the phase transition occurs without the requirement for interaction. BEC has appealing qualities, such as a coherence nature (as for the laser). In 1995, various groups achieved their first experimental successes with atomic gases,

the Bose-Einstein condensates of bosonic atoms. The temperatures required to reach condensation are of the order of $0.5-2\mu K$, about 10^2 to 10^9 number of atoms are needed in the condensate, while the densities are between $10^{14}-10^{15}cm^{-3}$. The cigar-shaped Bose condensate has a typical diameter of $15\mu m$ and a length of 0.3 mm (Ketterle, 2001). The study of Bose-Einstein condensates demonstrates how early quantum mechanics' core ideas can be understood and shown in experiments. Observations of macroscopic matter-wave interference, vortex formation, and dark and bright solitons are the most famous experimental achievements. An attractive interaction is required for a phase transition to a superfluid state, as it influences the formation of pairs, which subsequently operate as bosons due to their integer total angular momentum and Bose condense. The quantum phenomena begin to appear when the number density $n=\frac{N}{V}$ reaches a specific value [45]

$$n = \frac{2.6}{\lambda_{dB}^3} \tag{1.78}$$

where the thermal de Broglie wavelength is denoted by

$$\lambda_{dB} = \frac{h}{\sqrt{2\pi m k_B T}}. (1.79)$$

This definition refers to the conventional statement $\lambda_{dB} = \frac{h}{mv}$ with v as the typical velocity of the atomic gas. Easily said, the thermal de-Broglie wavelength

measures the delocalization of atoms. This is the size of the portion in which an atom is most likely to reside when the atomic position is measured. When λ_{dB} equals the distance between atoms, the quantum effect becomes so pronounced that it becomes impossible to distinguish between individual particles. The Eqns. (1.78) and (1.79) state that 3.1K is the critical temperature of the Bose gas at the density of liquid ${}^{3}\text{He}$ (145 kg m^{-3} at atmospheric pressure). This is near to λ point at 2.2 K when superfluid He starts to form (see [1]). Helium liquefies at 4.2 K, but since helium is less dense than other liquids ($103 \text{ kg } m^{-3} \text{ for water}$) because of it's atomic structure. Helium atoms have weak interactions; their small size and extremely low polarizability are caused by the confined electron shell. Superfluid helium's detailed characteristics however are very different from those of a Bose-condensed gas with weak interactions. BEC takes place at temperatures about one microkelvin because trapped atomic gases have

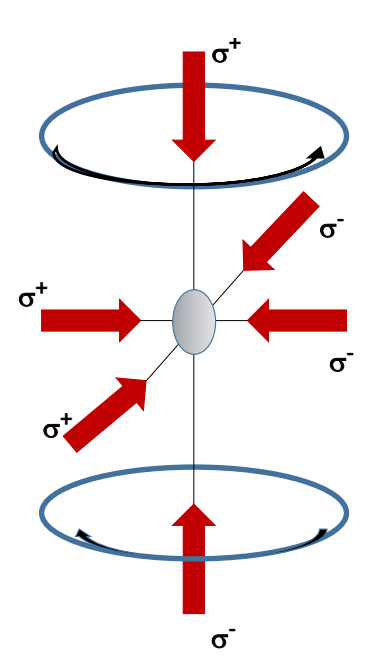


FIGURE 1.12: The MOT is made up of two coils with opposite currents for the magnetic field gradient and three pairs of counter-propagating beams with opposite $\frac{\sigma_+}{\sigma_-}$ polarization.

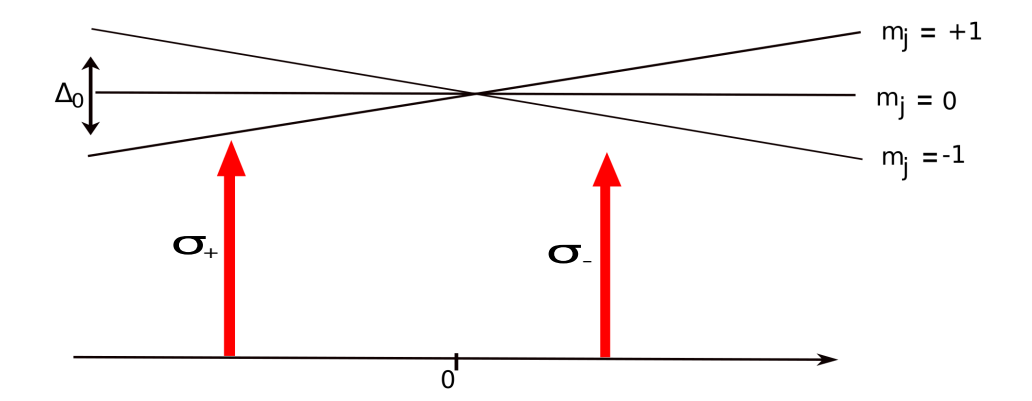


FIGURE 1.13: For the case of an atom having a J=0 to J=1 transition, the mechanism of a magneto-optical trap is shown. The atomic position affects how the sub-levels of the magnetic field gradient are Zeeman divided. The atom is illuminated by two counter-propagating circularly polarised light beams, and because of how transitions between the Zeeman states are chosen. There is an imbalance in the radiative force generated by the laser beams which pulls the atom back centre of the trap.

substantially lower density.

1.8 Magneto-optical trapping (MOT)

In the magneto-optical trap (MOT), the quadrupole magnetic field induces an imbalance in the scattering forces of the laser beams. It is this radiation force that closely confines the atoms². Figure 1.13 shows the basic principle of MOT for a transition from J = 0 to J = 1. The magnetic fields generated by the coils cancel out at their centre, resulting in B = 0. A uniform field gradient exists close to this zero field that perturbs the atomic energy levels. As a result of the Zeeman effect, the energy of the three sub-levels of the J = 1 level (with $m_J = 0, \pm 1$) varies linearly with position of the atoms, as illustrated for the z-axis in figure 1.13.³ The figure 1.12 depicts the circularly polarized laser beams and frequency of the counter-propagating laser beams which are just below the atomic resonance frequency. The optical molasses method to incorporate the frequency shift brought on by the Zeeman effect into the description of the magneto-optical trap

$$f_{MOT} = f_{scatt}^{\sigma_{+}}(\omega - kv - (\omega_{0} + \beta z)) - f_{scatt}^{\sigma_{-}}(\omega + kv - (\omega_{0} + \beta z)) \simeq -2kv \frac{df}{d\omega} + 2\frac{df}{d\omega_{0}}\beta z.$$
(1.80)

The terms $\omega_0 + \beta z$ and $\omega_0 - \beta z$ represent the resonant absorption frequency for the $m_I = +1$ transition at position z, and for $m_I = -1$ respectively. The Zeeman shift is

²Jean Dalibard proposed the fundamental concept of magneto-optical trapping which was then tested at Bell Laboratories in the United States in collaboration with a team from MIT

³There are other variations in the energy levels as well. According with Maxwell's equation div $\vec{B} = 0$ which implies that $\frac{dB_x}{dx} = \frac{dB_y}{dy} = -\frac{dB_z}{2dz}$.

obtained for the displacement z as

$$\beta z = g \frac{\mu_B}{\hbar} \frac{dB}{dz} z. \tag{1.81}$$

More generally, $g = g_{F'}m_F' - g_Fm_F$ is during a transition between the hyperfine-structure levels $|F',m_F'\rangle$ and $|F',m_F'\rangle$. However, $g \simeq 1$ for many of the transitions employed for laser cooling. The force is affected by frequency detuning $\delta = \omega - \omega_0$. So, $\frac{df}{d\omega_0} = -\frac{df}{d\omega}$. Therefore, the equation of motion is as follows

$$f_{MOT} = 2\frac{df}{d\omega}(kv + \beta z)$$
$$= -\alpha v - \frac{\alpha \beta}{k} z. \tag{1.82}$$

The Zeeman effect causes an imbalance in the radiation force which results in a restoring force with a spring constant of $\frac{\alpha\beta}{k}$ (expressed in this manner to emphasize that it evolves similarly to damping). The atom experiences over-damped simple harmonic motion under typical working conditions, as seen in Ref.[45] example. The magneto-optical trap is frequently employed in laser cooling experiments due to its excellent trapping and damping properties, which make it simple to load.

1.9 A Bose-Einstein condensate

Atomic interactions are accounted for by including terms in the Schrödinger equation derived from Eqn. (1.69), proportional to the square of the wave function [9]

$$\left(-\frac{\hbar^2}{2M}\nabla^2 + V(r) + g|\Psi|^2\right)\Psi = \mu\Psi. \tag{1.83}$$

The additional energy due to the interaction is proportional to $|\Psi|^2$ and it determines the probability of a particle being found in a particular region and the coupling constant are $g=\frac{4\pi\hbar^2Na_s}{M}$. This is obtained from Eqn. (1.69) with $|\eta|^2\to N|\Psi|^2$, which gives the interaction per atom when N atoms are present⁴. The energy of a single atom when there are all other atoms is denoted by the symbol μ (instead of E). This equation is called the Gross-Pitaevskii equation (see rigorous derivation in the book by Pitaevskii and Stringari (2016) [46]). Let us think about the atoms that are trapped in a harmonic potential

$$V(r) = \frac{1}{2}M\omega_x^2 x^2 + \frac{1}{2}M\omega_y^2 y^2 + \frac{1}{2}M\omega_z^2 z^2.$$
 (1.84)

We should consider all three oscillation frequencies are equal for the sake of simplicity, i.e., the isotropic potential $V(r) = \frac{1}{2}M\omega^2r^2$. To estimate the energy, we apply a

 $^{^4}$ There are actually N-1 other atoms, although, for large numbers of atoms, the difference from N is negligible.

variational technique. We select a Gaussian function for the trial wavefunction:

$$\Psi(r) = Ae^{-\frac{r^2}{2b^2}}. (1.85)$$

This can be used to calculate the expectation values of the terms in Eqn.(1.83)

$$E = \frac{3}{4}\hbar\omega \left(\frac{a_{ho}^2}{b^2} + \frac{b^2}{a_{ho}^2}\right) + \frac{g}{(2\pi)^{\frac{3}{2}}} \frac{1}{b^3}.$$
 (1.86)

When g = 0, this expression of differentiation indicates that the minimum energy obtains when $b = a_{ho}$, where

$$a_{ho} = \sqrt{\frac{\hbar}{M\omega}} \tag{1.87}$$

is the characteristic length of the quantum harmonic oscillator's Gaussian ground-state wavefunction. $a_{ho}=2\times 10^{-6}$ m is the harmonic oscillator length if sodium atoms are in a trap with oscillatory frequency $\frac{\omega}{2\pi}=100$ Hz. With this equilibrium value of b, the two terms that are potential energy and kinetic energy each contribute an amount equal to the total energy $E=\frac{3}{2}\hbar\omega$. This is consistent with the quantum harmonic oscillator's ground state⁵. Variational approaches pro-

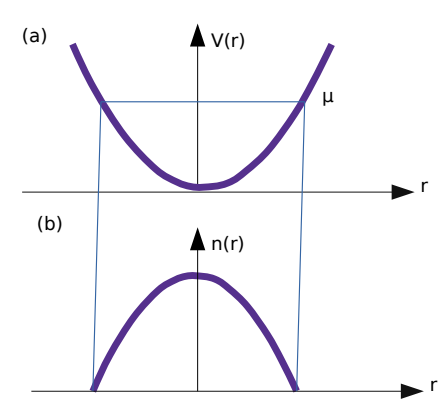


FIGURE 1.14: The condensate in the Thomas-Fermi regime has the similar form as the confining potential.(a) harmonic potential. (b) The density of atoms in a harmonic trap has an inverted-parabolic shape along all three axes.

vide accurate outcomes in this specific case, because the trial wave function has the Gaussian shape as the solution for the harmonic oscillator. Now let us explore what occurs when $g > 0^6$. Atomic interactions and kinetic energy are expressed in a ratio, which is ⁷ [9]

$$\frac{4}{3} \frac{1}{(2\pi)^{\frac{3}{2}}} \frac{g}{\hbar \omega a_{ho}^3} \simeq \frac{Na_s}{a_{ho}}.$$
 (1.88)

We can ignore the kinetic energy term if N > 700 atoms compensate the condensate 8 because this ratio equals $a_{ho}/a_s = 700$ for $a_{ho} = 2\mu m$ and $a_s = 3$ nm. However, if the kinetic energy term is neglected, the Gross-Pitaevskii (G.P) equation can be solved very easily. In this alleged Thomas-Fermi regime, Eqn. (1.83) is reduced to

$$\left(V(r) + g|\Psi|^2\right)\Psi = \mu\Psi. \tag{1.89}$$

⁵A zero-point energy of $\frac{1}{2}\hbar\omega$ has been allocated to each of the three degrees of freedom.

⁶It has been possible to create small Bose-Einstein condensates with interactions that are basically attractive, but when the number of atoms increases, these condensates collapse inwards.

⁷The factor $\frac{4}{3} \frac{1}{(2\pi)^{\frac{3}{2}}}$ has a numerical value of about 1.

⁸Typically, experiments have $N > 10^5$, and the condensate is considerably larger than $a_h o$ due to the effectively repulsive interactions. On the value of T_C , the interactions between the atoms in a diluted gas only have a marginal influence (less than 10%)

Thus, the region where $\Psi \neq 0$ one find

$$|\Psi|^2 = \frac{\mu - V(r)}{g}.$$
 (1.90)

As a result, in a harmonic potential, the number density of atoms is $n(r) = N|\Psi|^2$, which takes the shape of an inverted parabola

$$n(r) = \frac{N\mu}{g} \left(1 - \frac{x^2}{R_x^2} - \frac{y^2}{R_y^2} - \frac{z^2}{R_z^2} \right) = n(0) \left(1 - \frac{x^2}{R_x^2} - \frac{y^2}{R_y^2} - \frac{z^2}{R_z^2} \right)$$
(1.91)

where n(0) is the condensate's central number density. The density of the condensate is zero at points on the axes indicated by $x = \pm R_x$, $y = \pm R_y$, $z = \pm R_z$, and it has an ellipsoidal shape (see figure (1.14)) defined by

$$\frac{1}{2}\omega_x^2 R_x^2 = \mu. {(1.92)}$$

It is also similar for R_y and R_z . The chemical potential μ is obtained by the normalization condition

$$1 = \int |\Psi|^2 dx dy dz = \frac{8\pi}{15} \frac{\mu}{g} R_x R_y R_z.$$
 (1.93)

The suitable form of μ is [9]

$$\mu = \frac{1}{2} \left(\frac{15Na_s}{a_{ho}} \right)^{\frac{2}{5}} \hbar \bar{\omega} \tag{1.94}$$

where $\bar{\omega} = (\omega_x \omega_y \omega_z)^{\frac{1}{3}}$ is the gemetric mean of the oscillation frequencies.

1.10 Properties of Bose-condensed gases

Coherence and superfluidity are two remarkable features of Bose-condensed systems. Both connect to the microscopic explanation of condensate as N atoms with the same wave function and for Bose-condensed gases, they can be quite easily explained from the first principles (as in the following section).

1.10.1 Healing length

The kinetic energy expressions in the Schrödinger equation are ignored by the Thomas-Fermi approximation. As a result, the condensate's surface exhibits an unusually sharp edge (see figure 1.14), thus the gradient would become discontinuous and $\nabla^2\Psi$ would become infinite. Therefore, we must consider kinetic energy at the boundary. We compare the kinetic term (that included $\nabla^2\Psi \simeq \hbar^2/(2M\xi^2)$ to the energy scale of the system given by the chemical potential to calculate the closest distance ξ over which the wave function can change. Atoms having energies greater

than μ leave the condensate. The $n_0 = N/g$ from Eqn. (1.92) we find that [9]

$$\frac{\hbar^2}{2\pi\xi^2} \simeq \mu = \frac{4\pi\hbar^2 a_s n_0}{M}.$$
 (1.95)

Hence, we get $\xi=\frac{1}{8\pi a_s n_0}$, which use to characterize the vortex-core radius, which appear in a superfluid as the confining potential rotates (or a fast-moving object passes through it). For cold atomic gases, the healing length is near the order $\xi\simeq 0.5\mu m$. In the case of superfluid He-3, due to the strong interactions effect, the healing length is small ($\sim \xi \simeq 0.8 \text{Å}$).

1.10.2 The coherence properties of a Bose- Einstein Condensate

Coherence is the another crucial characteristic. This property makes it possible to treat the entire condensate as a single large matter wave similar to how a laser produces light waves. The two atomic clouds became expanded and overlapped when the trapping potential was removed due to the atomic repulsion to each other. The two condensates interfere with one another; atoms are absent from certain locations where destructive interaction between the matter waves from the two source points occur. These atoms are then redistributed to locations in the fringe pattern where matter waves effectively superpose. Such interference is common in optics, but this experiment differs significantly from standard double-slit experiments in a very intriguing way. The phases of the two condensates in the MIT experiment had no fixed relationship, and before the experiment was carried out. There was a lot of debate about whether interference would be seen. Each time the experiment was carried out, distinct interference fringes were observed. When the experiment was repeated, bright and dark stripes appeared in different places. As a result, the fringe pattern is "washed out" on average over many runs. However, the position of these stripes depends on how the phase of the condensate changed in that particular experiment. It is necessary to be able to discern interference fringes in a single shot to see the interference of two condensates.

1.11 Rotating quantum gases

Now we are interested in the origin of Landau levels in the single-particle energy spectrum of the quantum gases. In this section, we will describe how this appears for trapped harmonically quantum gases under situations of rapid rotation. We consider the atoms are neutral. Simulating behavior of charged particles (electrons) in a magnetic field is a common problem. The Lorentz force does not affect our ultracold atoms since they are neutral. Rotating the trap containing the particles is probably the simplest (conceptually) approach to this problem. The force acting on

the rotating frame, we have

$$M\frac{d\vec{v}}{dt} = \underbrace{-M\omega_{\perp}^{2}\vec{r}_{\perp} - M\omega_{z}^{2}\vec{z}}_{\text{Trapping force}} \underbrace{-M\vec{\Omega} \times (\vec{\Omega} \times \vec{r})}_{\text{Centrifugal force} = M\Omega^{2}r_{\perp}} \underbrace{-M\frac{d\vec{\Omega}}{dt} \times \vec{r}}_{\text{Euler force} = 0} \underbrace{-2M\vec{v} \times \vec{\Omega}}_{\text{Coriolis force}}.$$
 (1.96)

The idea is to take advantage of the similarity between the magnetic Lorentz force $(\vec{qv} \times \vec{B})$ and the Coriolis force $(2M\vec{v} \times \vec{\Omega})$, which occurs when the frame rotates at angular frequency $\vec{\Omega}$ along the z-direction. $2M\Omega$ takes on the role of q^*B . As a result in the rotating frame, neutral atoms act as charged particles if they were in a true magnetic field. Furthermore, the particles will be subjected to centrifugal force, which can be compensated for by harmonic confinement. This technique works and has resulted in the formation of vortices and vortex lattices in BECs. However, there are some disadvantages. One of the issues is the destabilizing centrifugal force in the presence of trap asymmetry. More precisely, one can understand from the hamiltonian expression. When addressing the problem of a rotating gas theoretically, it is common to assume that an arbitrarily anisotropic potential moving at frequency Ω is added to the isotropic trapped potential. The state of the system is only stationary in the frame rotating at Ω when the stirring potential is present. $H = H_{Lab} - \dot{\Omega} \cdot \vec{L_z}$ deduces the Hamiltonian in the rotating frame from the Hamiltonian in the lab frame H_{Lab} . The rotational potential is usually switched off for a short amount of time before to the measurement. When the system evolves in the axis-symmetric potential, then Ω acts as the Lagrange multiplier for the angular momentum that is being placed L_z , which is a constant of motion. Consider an atom that is trapped in an isotropic harmonic trap with an oscillation frequency of $\omega \perp$ in the xy plane. In a rotating frame around the z-axis with angular frequency Ω , the Hamiltonian that describes particle motion is given as

$$H_{Rot} = \frac{p_x^2 + p_y^2}{2M} + \frac{1}{2}M\omega_{\perp}^2(x^2 + y^2) - \Omega L_z + \frac{p_z^2}{2M} + \frac{1}{2}M\omega_z^2 z^2$$
 (1.97)

where the angular momentum operator of the particle along the z-axis is $L_z = xp_y - yp_x$. This Hamiltonian one can be written as follows:

$$H_{Rot} = \frac{(\vec{p}_{\perp} - q'\vec{A})^2}{2M} + \frac{1}{2}M(\Omega^2 - \omega_{\perp}^2)(x^2 + y^2) + H_z.$$
 (1.98)

However, since H_{\perp} only contains the coordinates x and y. The quantum Hall effect is based on this Hamiltonian, as well as the term describing the interaction effects. The $\vec{r}_{\perp}=(x,y,0)$ and $\vec{p}_{\perp}=(p_x,p_y,0)$ are the 2-d position and momentum vectors, and the effective vector potential is $q'\vec{A}(\vec{r})=M\Omega(x\hat{j}-y\hat{i})$ and the corresponding magnetic field is $q'\vec{B}=2M\vec{\Omega}$. For identical neutral particle one consider q'=1. Thus, one can justify the comparison of the Coriolis and Lorentz forces. In addition to the Coriolis force, the centrifugal force $M\Omega^2\vec{r}_{\perp}$ appears in the rotating frame. The system is stable when the rotation rate is below the "centrifugal limit" $\Omega \leq \omega_{\perp}$.

Centrifugal force leads to a drop in the harmonic confinement potential. It is exciting to see how this rotation technique can exactly apply the magnetic Hamiltonian Eqn. (1.123). If we compare Eqn. (1.123) to Eqn. (1.98), we realize that one condition need to be fulfilled: The centrifugal potential would balance the trapping potential, thus $\Omega = \omega_{\perp}$, implying that an extra potential (possibly quadratic, as in [47]) is required to confine the particles). When $\Omega < \omega_{\perp}$, the Hamiltonian Eqn. (1.98) in the polar coordinates system, one can also be solved alternatively. The normalized eigen-state is given by

$$\Psi_{n,m,j}(\vec{r}) = \sqrt{\frac{1}{2\pi} \frac{2}{l_{\perp}^{2}} \frac{(n - [|m| + m]/2)!}{(n + [|m| - m]/2)!}} e^{-im\phi} \left(\frac{r_{\perp}^{2}}{l_{\perp}^{2}}\right)^{\frac{|m|}{2}} e^{-\frac{r_{\perp}^{2}}{2l_{\perp}^{2}}} \times L_{n - \frac{|m| + m}{2}}^{|m|} \left(\frac{r_{\perp}^{2}}{l_{\perp}^{2}}\right) \sqrt{\frac{1}{\sqrt{\pi}l_{z}}} \frac{1}{\sqrt{2^{j}j!}} H_{j}(z/l_{z}) e^{-z^{2}/2l_{z}^{2}}.$$
(1.99)

Eqn. (1.99) comes after solving the time-independent Schrödinger equation. Here $n=0,1,2,\ldots$ is known as the Landau level index, $m=-n,-n+1,-n+2,\ldots,+n$ the magnetic quantum number in the n'th Landau level, and $j=0,1,2,\ldots$ is called the sub-band index for motion along the z-axis. The Eqn. (1.99) contains analytical equations for higher Landau levels as well as wave functions with the correct angular momentum. The Eqn. (1.99) describes the relationship between the Fock-Darwin spectrum for the neutral particles in a magnetic field in the xy plane and harmonic confinement along the z-axis. The energy eigenvalue of the system in the rotating frame of reference, when rotated at an angular speed of Ω , is given by

$$\epsilon_{n,m,j} = (n+1/2) \hbar(\omega_{\perp} + \Omega) + (m'+1/2) \hbar(\omega_{\perp} - \Omega) + (j+1/2) \hbar\omega_{z}.$$
 (1.100)

where m' = n - m = 0, 1, 2, ... is treated as a single quantum number in Ref.[12, 10, 48, 49].

To create a vortex, one must rotate faster than the critical speed of $\Omega_c \approx 0.7\omega_{\perp}$ ([12]). However, due to centripetal forces, the atoms are no longer bound in the trap when the rotation frequency is higher than the trapping frequency. Thus, it is a delicate balancing act to choose the right rotation frequency for generating vortex lattices in BEC systems. Even yet, large vortex lattices have already been generated, both conceptually and practically [22, 50, 51, 52]. A "rotating bucket" method has been used an ultracold atomic systems. It is one way to experimentally create rotation for a few vortices ([53]). This technique involves confining bosons in a magnetic field and superimposing an aniso-tropic potential that rotates at the required angular speed [54, 55, 56]. The evaporative spin-up approach, in which atoms with lower angular momentum are evaporated so that the remaining atoms have a higher rotational speed, is one of the ways [50, 57]. Additionally, the rotation has recently been used in experiments to create vortex-ring-like formations.

1.11.1 Quantum Hall effect for rotating quantum gases

The Lorentz force $F = q\vec{v} \times \vec{B}$ (for an electron) does not act on electrically neutral atoms in a magnetic field \vec{B} . However, when we place atoms in a rotating frame, they experience the Coriolis force($F = 2M\vec{v} \times \vec{\Omega}$), as a result of a rotating field. Because of the structural similarities of the Coriolis forces and Lorenz forces. The rotating ultracold gases of neutral atoms can be able to produce quantum Hall states. In this part, we will explain the relationship between rotating gas and quantum Hall states. The quantum Hall effect which is characterized by a 2-d electron gas in a strong magnetic field and fast-rotating atomic BEC has quite a strong theoretical similarity that was first identified more than 20 years ago. The QHE, which happens in a 2-d electron gas at low temperatures in the presence of strong magnetic fields, and a fast-rotating dilute BEC of electrically neutral atoms, are well known to have a tight theoretical link. The key to this similarity is that rotation and perpendicular magnetic fields are found to play analogous roles in 2-d, making the two systems mathematically identical. This implies that given a quick enough rotation, a Bose condensate must reach a domain of tightly coupled quantum Hall states. The quasiparticle excitations obey fractional (anyon) statistics in this regime.

Experimentally constructed Abrikosov lattices with hundreds of vortices are near the rotation velocity at which this vortex lattice structure is projected to melt, putting the system in the quantum Hall regime. The fundamental reason for this is that at these rotation velocities, the system is approaching the point when the centrifugal potential drops the external harmonic trap, causing the atomic cloud to fly apart. The fractional effect is a considerably more delicate phenomenon that occurs (primarily) in the LLL and can only be learned when the electron interactions are taken into consideration, as discussed below. Another important aspect to note is that if $\omega_{\perp} = \Omega$, the mean system flattens out, revealing the Landau problem (free electrons in a perpendicular magnetic field) which is connected to QHE. The total energy of the system is then independent of m. Thus, total Hamiltonian describes as a quasi-2D system with an energy spectrum given as

$$\epsilon_{n,m,j} = (n+1/2)\hbar\omega_c + (j+1/2)\hbar\omega_z. \tag{1.101}$$

The energy spectrum is highly degenerate with single-particle states having the same energy regardless of angular momentum value m. Now the effective "Larmor frequency" is $\hbar\omega_c=\hbar\frac{q^*B}{M}=2\hbar\omega_\perp=2\hbar\Omega$. For the quasi-2d case, the wave-function for the lowest Landau level (LLL(n=0,j=0)) [58] states can be written as

$$\Psi_{0,m}(\mathbf{r}) \propto (\frac{x+iy}{l_{\perp}})^m e^{-\frac{x^2+y^2}{2l_{\perp}^2}} e^{-\frac{z^2}{2l_{z}^2}}.$$
 (1.102)

This wave function of course, meets the normalization condition $\int dx dy |\Psi_{0,m}|^2 = 1$. Where $l_{\perp,z} = \sqrt{\frac{\hbar}{M\omega_{\perp,z}}}$ is the confinement lengths in the radial and axial directions. If one makes the connection of Eqn. (1.102) with fractional quantum Hall state then

the new length scale define as $\zeta \equiv \frac{x+iy}{l_{\perp}}$ and $l = \sqrt{\frac{\hbar}{M\omega_c}} = \frac{l_{\perp}}{\sqrt{2}}$. Now normalized 2d the wave function for LLL states can be written as

$$\Psi_{0,m}(\zeta) = \frac{1}{\sqrt{2\pi l^2 m! 2^m}} \zeta^m e^{-\frac{|\zeta|^2}{4}}$$
(1.103)

where l is the magnetic length and $m \ge 0$. It is noted that $\zeta = \frac{r_{\perp}}{l_{\perp}} e^{i\phi}$ when expressed in 2-d polar coordinates.

Now, we want to show an expression for the total number of states per unit area in a single Landau level. One knows that the complex coordinates representation of the position vector can be expressed in terms of ladder operators as $z=2l_{\perp}(a^{\dagger}+b)$, $\bar{z}=2l_{\perp}(a+b^{\dagger})$. One can determine the quantized orbit for the $\Psi_{0,m}(\zeta)$ state using

$$\pi \langle n_+ | z\bar{z} | n_- \rangle = 2\pi l_\perp^2 (n_+ + n_- + 1).$$
 (1.104)

Now the ring has the radius $R = \sqrt{2\pi l_{\perp}^2(n_+ + n_- + 1)}$. For a large n value, the orbit becomes strongly localized within $\sim l_{\perp}$ of the ring. In a thermodynamic limit, the area occupied per electron is $2\pi l_{\perp}^2$. We take here the lowest landau level is filled by occupying all single particle quantum state with $n_+ = 0$, and $n_- = n^* - 1$. Another way one can obtain the same result

$$\sum_{m=0}^{n^*-1} |\Psi_{0,m}(\zeta)|^2 = \frac{1}{2\pi l_{\perp}^2} \sum_{m=0}^{n^*-1} \frac{X^m}{m!} e^{-X} \to \frac{1}{2\pi l_{\perp}^2}$$
(1.105)

where $X \equiv \frac{|\zeta|^2}{2l_\perp^2}$. The macroscopic Landau level degeneracy that creates the opening for novel physical phenomena in the strong magnetic field limit. The rotation rate cannot be greater than the radial trapping frequency since the centrifugal force effectively creates an anti-trapping potential.

Let us now return to the harmonic trapping potential for the many-body problem. We will use the Gross–Pitaevskii (G.P) approximation and at the end of this portion we will see, when it fails. The effective confining potential in the rotating frame becomes shallower as the rotation rates increase (see Eqn. (1.122)), lowering the interaction energy and lowering the density of the gas. A suitable approximation is to employ a trial condensate wave function with components mainly at the LLL when the interaction energy $\tilde{g}n_{2d}$ is less than the energy $2\hbar\Omega$ required to excite higher Landau levels [48]. The trial wave function is a polynomial in $\zeta = x + iy$ multiplied by a Gaussian factor, based on the form of the functions Eqn. (1.103). Now we consider that the G.P wave function is a linear combination of these LLL eigenfunctions

$$\Psi_{G,P}(r_{\perp}) = \sum_{m} C_m \Psi_{0,m}(r_{\perp}) \propto \prod_{j=1}^{N} (\zeta - \zeta_j) e^{-\frac{|\zeta|^2}{4}}.$$
 (1.106)

The product from $\prod_{j=1}^N (\zeta - \zeta_j)$ is a complex polynomial function that disappears at each of the points $\{\zeta_j\}$ and all those are nodes position of Ψ . The LLL trial solution has only quantized vortices found at positions of zeros $\{\zeta_j\}$, the reason is the phase of wave function raises by 2π whenever ζ goes around any of these zeros $\{\zeta_j\}$. The spacing of the vortices is determined by number density $|\Psi_{LLL}(r_\perp|^2)$. The core size is same with the inter-vortex spacing $l_\perp = \sqrt{\frac{\hbar}{M\Omega}}$ in the limit of $\Omega \equiv \omega_\perp$. Since LLL wave functions are crucial to the quantum Hall effect, this LLL regime is known as "mean-field quantum Hall" limit. It to be noted that we are still in the regime directed by the G.P equation, so there still the presence of a BEC. The most crucial fractional states at $\nu = 1/m$ are defined theoretically with m is an odd integer, when Laughlin introduced his well-known many-body wave function in 1983, for the ground state

$$\Psi_m(\zeta_1, \zeta_2, \dots, \zeta_N) = \prod_{i < j} (\zeta_i - \zeta_j)^m e^{-\frac{\sum_i |\zeta_i|^2}{4}}$$
 (1.107)

where $\zeta_i \equiv \frac{(x_i+iy_i)}{l_\perp}$ are 2-d complex coordinates indicating the positions of the particles in the complex plane. A number of highly correlated states related to some well-known quantum Hall effect states in a particular bosonic version of the Laughlin state, exist for the smaller value of ν (here $\zeta_i = \frac{x_i+iy_i}{l_\perp}$ refers to i-th particle). A novel, completely quantum mechanical state of matter is represented by the Laughlin wave function (especially for an incompressible quantum fluid). In the plasma analogy, if the particles have artificial charge m and electron density is $\frac{1}{m} \frac{1}{2\pi l_\perp^2}$. Hence landau level filling factor $\frac{1}{m} = \frac{1}{3}, \frac{1}{5}, \frac{1}{7}, \ldots$ etc. For $\omega_\perp > \Omega$ and at absolute zero temperature, the density of atoms is $|\Psi_{n,m}(\mathbf{r}_\perp)|^2\Theta(\varepsilon_{n,m}-\varepsilon_F)$ with ε_F is the Fermi energy and $\Theta(y)$ is the step function. The total number of atoms can be written as $\sum_{n,m} (\varepsilon_F - \varepsilon_{n,m})$. The density of atoms at finite temperature T becomes

$$\bar{n}_{2d} = \sum_{n,m} |\Psi_{n,m}(\mathbf{r}_{\perp})|^2 f(\epsilon_{n,m})$$
 (1.108)

where $f(\epsilon_{n,m})$ is Fermi-Dirac distribution function and total number of atoms is $N = \sum_{n,m} f(\epsilon_{n,m})$.

1.11.2 The filling fraction

The Gross-Pitaevskii mean-field theory explained earlier is an approximate theory. Here we assume that the ground state is a simple condensate. It is essential to investigate under what conditions its results are reliable. It is obvious that the single-electron quantum mechanics cannot account for fractional Hall states. Now the connection between cold atoms in the 2-d LLL and the FQHE of electrons can be explained. Thus, the presence of a strongly correlated and gapped ground state at particular filling factors provides a base for the FQH physics mechanism. In the

FQHE of electrons, the ground states are described by the electron filling factor

$$\nu_{electron} \equiv n_{electron} \frac{\hbar}{eB} \tag{1.109}$$

where $n_{electron}$ is the 2-d number density. From the mapping of the rotating atomic gas in 2-d, the similar quantity is (Cooper et al., 2001)

$$\nu \equiv n \frac{\hbar}{q^* B} = n \frac{\hbar}{2M\Omega}.\tag{1.110}$$

Thus, the filling factor of the rotating gas in term of the votex density is

$$\nu = \frac{n}{n_{v_1}} = \frac{N}{N_{v_1}}. (1.111)$$

Here, we assume that the particle is to be distributed uniformly over an area containing N_v vortex. The above result arises from the equivalence of flux density n_{ϕ} and vortex density n_v in a large system. Because of similarities of a 2-d electron gas in a high magnetic field, ν is known as the "filling fraction" [49]. Theoretically, the range of rotational frequencies Ω can be separated into three regimes. They can be identified by the value of the filling factor. Strongly correlated states achive at higher $\Omega \approx \omega_{\perp}$. The high fillings fraction $\nu > 100$ corresponds to the regime of vortex lattices, which is known as a mean-field quantum Hall regime. The previous experiment [50] was showed $N \sim 10^5$ and $N_v \sim$ several hundred, so that $\nu \sim$ a few hundred. Transversal excitations of the vortex lattice become less frequent as more vortices start to form in the system. The expected lattice melting below $\nu \sim 10$, which is assumed to be caused by quantum fluctuations, is predicted by the longwavelength characteristic of Tkachenko modes. The numerical studies [49] show that, for a small number of vortices $N_v \sim 8$ with variable N the coherent G.P state is favored for $\nu \geq 6$. In the crossover regime, extrinsic vortex phases are exacted to substitute the Abrikosov vortex lattice. Strongly correlated quantum phases are expected to produce mainly fractional quantum-Hall liquids if N_v eventually exceeds the number of particles in the region of critical rotation. Numerical simulations show the subsequent creation of a highly correlated fractional (incompressible) quantum Hall state for $\nu \sim 2$. Highly degenerate LLLs approve the creation of states with low occupation per level ("fully fragmented condensate."). The difficulty is that one cannot rotate condensate fast enough in an experiment to enter this regime. Reducing the number of particles does not operate since one loses the signal.

1.11.3 Vortex Lattice

When superfluid He is allowed to circulate in a rotating vessel by cooling liquid He from above the superfluid transitions to the superfluid phase [59]. The superfluid then produces a collection of single quantized vortex lines that are oriented parallel to the rotational axis. The kinetic energy of the superfluid flow becomes a significant

impact on the arrangement of dilute vortices when they are separated by a distance of $a_v >> \xi$. The following results arise from the minimization of the kinetic energy of the superfluid flow in the rotational system [60]:

- i) For the average vortex density to be determined in the plane perpendicular to the rotational axis, the mean superfluid flow must mimic rigid body rotation. The average vortex density $n_v = \frac{N_v}{A} = \frac{2M\Omega}{\hbar}$ is determined by the Feynman result [61] by setting the integral of the vorticity of a rotating body over an area A is $2\Omega A$, equal to the motion of a superfluid with N_v vortices in that area $N_v\hbar/m$.
- ii) the vortices interact pairwise in a logarithmic repulsive manner and have an interaction energy per unit length of

$$-n_{s} \frac{\hbar^{2}}{2\pi M} \sum_{i < j} ln(\frac{|R_{i} - R_{j}|}{\zeta})$$
 (1.112)

where $R_i = (X_i, Y_j)$ is the location of the i_{th} vortex in the plane perpendicular to the rotation axis and n_s is the superfluid density. A triangular lattice is a ground state form of a set of classical particles that interact in a logarithmic repulsive manner. Therefore, at low temperatures one expects the vortices to form a triangular Abrikosov lattice [62].

1.11.4 Mean-field Quantum Hall regime

Let us think about the effects of increasing the rotation frequency. Based on the filling factor, several phenomena can be anticipated. In the case of rapid rotation $(\Omega_c \lesssim \Omega \lesssim \omega_\perp)$ the vortex lattice is formed in the rotating trapped Bose Einstein condensate. The lattice pattern is tri-angular shape. This vortex lattice is called Abrikosov vortex lattice. The Abrikosov vortex lattice [63] has been experimentally observed [22, 54]. In the rotating frame, at zero temperature, the state of the system is obtained by minimizing the energy

$$E' = E - \Omega L = \int \left[\frac{|(\vec{p} - M \vec{\Omega} \times \vec{r})\Psi|^2}{2M} + \frac{M}{2} (\omega_{\perp}^2 - \Omega^2) r^2 |\Psi|^2 + \frac{g}{2} |\Psi|^4 \right] d\vec{r}. \quad (1.113)$$

The above equation clearly shows that as Ω approaches ω_{\perp} then the system belongs to a quasi-2d system. When the boson filling factor ($\nu_0 = N_0/N_v \lesssim 8$) then the system belongs in the mean-field quantum Hall regime obeys the Gross-Pitaevskii equation (G.P), where the mean-field theory is still appropriate but the system state is well described by the LLL (Eqn. (1.106)) approximations [64]. The kinetic energy of the system remains exactly equal to $\hbar\omega_{\perp}$ in the LLL approximation, where $n=|\Psi|^2$ denotes the particle number density. So, the Eqn. (1.113) reduces to

$$E' = \hbar \omega_{\perp} N + \frac{M}{2} (\omega_{\perp}^2 - \Omega^2) \int r^2 |\Psi|^2 d\vec{r} + \frac{g}{2} \int |\Psi|^4 d\vec{r}.$$
 (1.114)

We are looking for situations with a many vertices. The particle wave function varies rapidly near to the vortex position due to the wave function nodes at the vortex gap. It is thus convenient to incorporate coarse-grained averages of density (\bar{n}) taken over a distance greater than the inter vortex distance, but small respect to the cloud size. Thus, the energy of the system is defined as

$$\bar{E}' = \hbar\omega_{\perp}N + \frac{M}{2}(\omega_{\perp}^2 - \Omega^2) \int r^2 \bar{n} d\vec{r} + \frac{g\beta}{2} \int \bar{n}^2 d\vec{r}$$
 (1.115)

where the Abrikosov lattice parameter is represented by

$$\beta \equiv \frac{\bar{n^2}}{\bar{n}^2} \tag{1.116}$$

for a triangular lattice. The value of β , one can calculate to be $\beta \approx 1.1596$ [63]. One takes the approximation that the vortices are on a regular triangular lattice and hence we can take β to be independent of position. $N=\int \bar{n}d\vec{r}$ and the appropriate density distribution is obtained via minimization of \bar{E} w.r.t the coarse-grained density distribution, under the assumption that the total particles number remains constant and thus gives

$$\beta g \bar{n} = \mu - \hbar \omega_{\perp} - \frac{M}{2} (\omega_{\perp}^2 - \Omega^2) r_{\perp}^2. \tag{1.117}$$

or

$$\bar{n}(r_{\perp}) = \bar{n}(0)(1 - \frac{r_{\perp}^2}{R_{\perp}^2})$$
 (1.118)

where $\bar{n}(0) \equiv \frac{\mu - \hbar \Omega}{g\beta}$ and $R_{\perp} \equiv \sqrt{\frac{2(\mu - \hbar \Omega)}{M(\omega_{\perp}^2 - \Omega^2)}}$. The chemical potential represented by μ in the rotating frame. The coarse-gained density profile of a rapid rotating BEC has a Thomas–Fermi distribution like form [65].

1.12 Introduction of Artificial Gauge

Many different physical contexts exist for the realization of synthetic gauge fields. One of the most pervasive ideas in physics. Gauge fields offer incredible connections between the domains of condensed matter physics, quantum optics, high-energy physics, and cosmology. It is difficult to simulate magnetic effects with quantum gases: requires the creation of "artificial gauge potentials" as "substitutes" for true electromagnetic fields. Electric forces can be simulated by gravitational acceleration or gradient magnetic fields. But how can we simulate the Lorentz force ($\vec{F}_{Lorentz} = q'\vec{v} \times \vec{B}$) experienced by charged particles moving in a magnetic field? In quantum mechanics the Schrödinger equation is

$$i\hbar \frac{\partial \Psi(\vec{r},t)}{\partial t} = \frac{(\hat{p} - q'\vec{A}(\hat{r}))^2}{2M} \Psi(\vec{r},t). \tag{1.119}$$

Now consider gauge transformation which is imposed by the Schrödinger equation can be expressed as follows

$$\vec{A}(\vec{r}) \rightarrow \vec{A}'(\vec{r}) = \vec{A}(\vec{r}) + \vec{\nabla}\chi(\vec{r})$$
 (1.120)

where χ is gauge parameter.

$$\Psi(\vec{r},t) \to \Psi'(\vec{r},t) = e^{\frac{(iq\chi(\hat{\tau})}{\hbar}} \Psi(\vec{r},t). \tag{1.121}$$

A gauge transformation changes the wave function by giving it a phase. Investigation of the physical consequences of gauge fields, first demonstrated by the pioneering Aharonov-Bohm effect [66]. Gauge potentials arise naturally from "real" electromagnetic fields, but through proper manipulation of physical systems, gauge fields of various types can be created and fine-tuned. This can be done both in solid-state devices and ultracold atomic gases [67, 68, 69] and photonic crystals [70].

We are especially interested in the spectral characteristics that are well described by a designed Hamiltonian of the type

$$H(\hat{p} - \vec{A}), \qquad \vec{A} = \vec{A}\{\hat{r}, \vec{\sigma}, t\}$$
 (1.122)

where \hat{p} represents the canonical momentum operator and $\vec{A}\{\hat{r}, \vec{\sigma}, t\}$ represents a general gauge potential. \vec{A} can theoretically be affected by the position operator \hat{r} and the "spin" degrees of free-

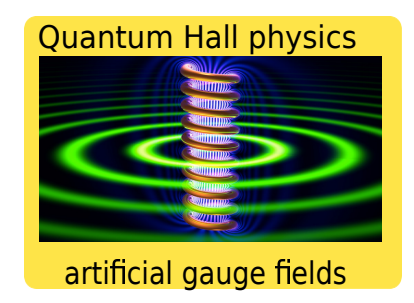


FIGURE 1.15: Artificial Magnetic field

dom or time. It is crucial to note that the technical gauge potential is always treated as a classical external field. This gauge field is not dynamic. On the other hands, particle motion has no effect. The method presented in this work does not reproduce the full gauge theory (such as Maxwell's electromagnetic equations). Let us recall the idea of the magnetic field in quantum mechanics. Suppose there is a free particle in quantum mechanics. The Hamiltonian operator is $H = \frac{p^2}{2M}$. The Hamiltonian is given as follows for the motion of a charged particle in an external, static, and uniform magnetic field

$$H = \frac{(\hat{p} - q'\vec{A}(\hat{r}))^2}{2M} \tag{1.123}$$

where \hat{p} is the canonical momentum which is canonically conjugate to the position. It is not the mechanical momentum. If we see the dispersion curve for a free particle, $\vec{p}=0$ the potential energy is minimum (see figure (1.16)). But, for the charged particle in a magnetic field, minimum at qA in the dispersion curve (see figure (1.16)). Thus, by shifting the dispersion curve one can simulate a vector gauge potential. We design a Hamiltonian with a spatially variable vector potential, by giving $\vec{B}^* = \vec{\nabla} \times \vec{A}^*$ in order to construct an artificial magnetic field \vec{B}^* for charge-less atoms [14]. If we make shift time-dependent we can simulate qA giving $\vec{E} = -\frac{d\vec{A}^*}{dt}$.

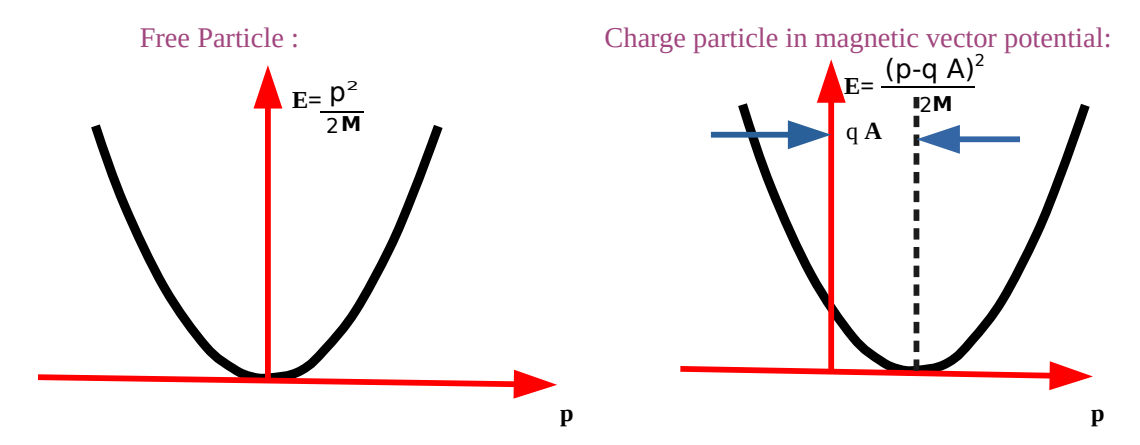


FIGURE 1.16: Shifting the dispersion curve simulates a vector gauge potential.

Researchers can construct and control complex vortex structures with the use of artificial magnetic fields, which is a very powerful tool. Two photons Raman- dressed atom behaves like a charged particle in a magnetic field [14].

1.13 The Artificial de Haas-van Alphen effect

The de Haas-van Alphen (dHvA) effect is a quantum mechanical phenomenon, that causes the magnetization of a pure metal crystal to oscillate by increasing the strength of the magnetic field. A macroscopic manifestation of the Landau level quantization of the electron spectrum in the presence of a magnetic field is the de Haas-van Alphen oscillation. The de Haas-van Alphen oscillations have now developed into a useful tool for describing the electronic states of semimetals and metals with large mean-free paths. We investigate the prospect of finding comparable quantum oscillation phenomena for ultracold gases of fermionic atoms, either by rotating the gas or by employing an artificial gauge field. The effect of rotation or an artificial magnetic field on a non-interacting Fermi gas in a cylindrically symmetric harmonic trap is examined in our study. The rotating harmonically trapped Fermi gas (please see Eqn. (1.96)) exploit the analogy between magnetic field effects on charged particles and rotational effects on rotating systems to predict de Haas-van Alphen-like oscillations in the differential scattering cross-section. When the artificial magnetic field is swept, we demonstrate the quasi-periodic behavior of the differential scattering cross-sections in the low-temperature limit.

Bibliography

- [1] J. F. Annett, Superconductivity, Superfluids and Condensates, sec. 3.2, p. 48-49, Oxford University Press, Oxford (2004)
- [2] H. Z. Cummins and H. L. Swinney, J. Chem. Phys. 45, 4438 (1966)
- [3] A. Bhattacharya and S. Biswas, Quant. Phys. Lett. 6, 5 (2017)
- [4] M. H. Anderson, J. R. Ensher, M. R. Matthews, C. E. Wieman and E. A. Cornell, Science **269**, 198 (1995)
- [5] K. B. Davis, M.-O. Mewes, M. R. Andrews, N. J. van Druten, D. S. Durfee, D. M. Kurn, and W. Ketterle, Phys. Rev. Lett. 75, 3969 (1995)
- [6] C. C. Bradley, C. A. Sackett, J. J. Tollett, and R. G. Hulet, Phys. Rev. Lett. 75, 1687 (1995); Erratum: Phys. Rev. Lett. 79, 1170 (1997)
- [7] F. Dalfovo, S. Giorgini, L. P. Pitaevskii, and S. Stringari, Rev. Mod. Phys. 71, 463 (1999)
- [8] B. DeMarco and D. S. Jin, Science 285, 1703 (1999)
- [9] L. P. Pitaevskii and S. Stringari, *Bose-Einstein Condensation*, Oxford University Press, Oxford (2003)
- [10] S. Stock, B. Battelier, V. Bretin, Z. Hadzibabic, and J. Dalibard, Laser Phys. Lett.2, 275 (2005)
- [11] S. Giorgini, L. P. Pitaevskii, and S. Stringari, Rev. Mod. Phys. 80, 1225 (2008)
- [12] A. L. Fetter, Rev. Mod. Phys. 81, 647 (2009)
- [13] I. Bloch, J. Dalibard, and W. Zwerger, Rev. Mod. Phys. 80, 885 (2008)
- [14] Y. -J. Lin, R. L. Compton, K. Jiménez-García, J. V. Porto, and I. B. Spielman, Nature 462, 628 (2009)
- [15] J. Dalibard, F. Gerbier, G. Juzeliūnas, and P. Öhberg, Rev. Mod. Phys. 83, 1523 (2011)
- [16] M. Mancini, G. Pagano, G. Cappellini, L. Livi, M. Rider, J. Catani, C. Sias, P. Zoller, M. Inguscio, M. Dalmonte, and L. Fallani, Science 349, 1510 (2015)
- [17] V. Galitski, G. Juzeliūnas, and I. B. Spielman, Physics Today 72, 38 (2019)

44 BIBLIOGRAPHY

[18] C. J. Pethick and H. Smith, *Bose–Einstein Condensation in Dilute Gases*, 2nd ed., Cambridge University Press, Cambridge (2008)

- [19] S. Giorgini, L. P. Pitaevskii, and S. Stringari, Phys. Rev. A 54, R4633 (1996); S. Biswas, Phys. Lett. A 372, 1574 (2008)
- [20] W. Krauth, Phys. Rev. Lett. 77, 3695 (1996)
- [21] M. W. Zwierlein, J. R. Abo-Shaeer, A. Schirotzek, C. H. Schunck, and W. Ketterle, Nature 435, 1047 (2005)
- [22] J. R. Abo-Shaeer, C. Raman, J. M. Vogels, and W. Ketterle, Science 292, 476 (2001); C. Raman, J. R. Abo-Shaeer, J. M. Vogels, K. Xu, and W. Ketterle, Phys. Rev. Lett. 87, 210402 (2001)
- [23] A. P. Chikkatur, A. Görlitz, D. M. Stamper-Kurn, S. Inouye, S. Gupta, and W. Ketterle, Phys. Rev. Lett. 85, 483 (2000)
- [24] A. Montina, Phys. Rev. A 66, 023609 (2002)
- [25] Z. Idziaszek, K. Rzazewski, and M. Wilkens, J. Phys. B: At. Mol. Opt. Phys. **32**, L205 (1999)
- [26] A. Bhattacharya, S. Das, and S. Biswas, J. Phys. B: At. Mol. Opt. Phys. **51**, 075301 (2018)
- [27] S. Das and S. Biswas, Phys. Scr. 96, 125037 (2021)
- [28] S. Das, Phys. Lett. A 397, 127249 (2021)
- [29] S. Das, Physica B **635**, 413833 (2022)
- [30] J. W. Strutt, The London, Edinburgh, and Dublin Philosophical Magazine and Journal of Science, 41, 107 (1871); 41, 274 (1871); 41, 447 (1871)
- [31] A. Einstein, Ann. Physik **33**, 1275 (1910)
- [32] C. V. Raman, Indian J. Phys. 2, 387 (1928)
- [33] E. Smith and G. Dent, *Modern Raman Spectroscopy: A Practical Approach*, Wiley, West Sussex (2005)
- [34] S. Chen et al. (CLAS Collaboration), Phys. Rev. 21,483 (2022)
- [35] A. H. Compton, Phys. Rev. 97,07,(2006)
- [36] A. Guinier, X-ray diffraction in crystals, *imperfect crystals and amorphous bodies*, San Francisco and Co.
- [37] J. Als-Nielsen and D. McMorrow. *Elements of Modern X-ray Physics*. Wiley-Blackwell, 2000, see p. 24, 47 and 57.

BIBLIOGRAPHY 45

[38] C. Kittel, *Introduction to Solid State Physics*, 7th ed., ch. 2, p. 42, Wiley, Singapore (1996)

- [39] D. J. Griffiths, *Introduction to Quantum Mechanics*, 2nd ed., Pearson Education, Singapore (2005)
- [40] Lecture 1: *Introduction and Neutron Scattering Theory by Roger Pynn*, Los Alamos National Laboratory.
- [41] D. J. Wineland and Wayne M. Itano, Rev. Mod. Phys. 20, 1521 (1979)
- [42] E. Fermi, Ricerca Sci. 7, 13 (1936); K. Huang and C. N. Yang, Phys. Rev. A 105, 767 (1957)
- [43] I. Mitra, A. DasGupta, and B. Dutta-Roy, Am. J. Phys. 66, 1101 (1998)
- [44] A. Bhattacharya and S. Biswas, Quant. Phys. Lett. 6, 5 (2017)
- [45] C. J. Foot, Atomic Physics. Oxford University Press, (2004).
- [46] L. Pitaevskii, S. Stringari, *Bose-Einstein Condensation and Superfluidity*, Oxford University Press (2016).
- [47] V. Bretin, S. Stock, Y. Seurin, and J. Dalibard, Phys. Rev. Lett. 92, 050403 (2003)
- [48] Tin-Lun Ho, Phys. Rev. Lett. 87, (060403) (2001)
- [49] N. R. Cooper, Advances in Physics 57, 539 (2008)
- [50] V. Schweikhard, I. Coddington, P. Engels, V. P. Mogendorff, and E. A. Cornell Phys. Rev. Lett. **92**, 040404 (2004)
- [51] L. J. O'Riordan, A. C. White, and Th. Busch, Phys. Rev. A 93, 023609 (2015)
- [52] L. J. O'Riordan and Th. Busch, Phys. Rev. A 94, 053603 (2016)
- [53] F. Chevy and J. Dalibard, Europhysics News 37, 12-16 (2006)
- [54] K. W. Madison, F. Chevy, W. Wohlleben, and J. Dalibard, Phys. Rev. Lett. 84, 806 (2000)
- [55] P. C. Haljan, I. Coddington, P. Engels, and E. A. Cornell, Phys. Rev. Lett. 87, 210403 (2001)
- [56] E. Hodby, G. Hechenblaikner, S. A. Hopkins, O. M. Maragò, and C. J. Foot, Phys. Rev. Lett. 88, 010405 (2001)
- [57] V. Bretin, S. Stock, Y. Seurin, and J. Dalibard, Phys. Rev. Lett. 92, 050403 (2004)
- [58] N. K. Wilkin, and G. Gunn, Phys. Rev. Lett. 84, (6) (2000)
- [59] H. E. Hall and W. F. Vinen, Proc. Roy. Soc. A 238, 204 (1956)

46 BIBLIOGRAPHY

- [60] N. R. Cooper, Les Houches Lecture Notes, 2008 (unpublished).
- [61] R. J. Donnelly, *Quantized Vortices in Helium II*, Cambridge University Press, Cambridge, 1991
- [62] L. J. Campbell and R. M. Ziff, Phys. Rev. B 20, 1886 (1979).
- [63] A. A. Abrikosov, J. Exptl. Theoret. Phys. (U.S.S.R.) 32, 1442 (1957); Soviet Phys. JETP 5, 1174 (1957)
- [64] D. A. Butts and D. S. Rokhsar, Nature 397, 327 (1999)
- [65] G. Watanabe, G. Baym, and C. J. Pethick, Phys. Rev. Lett. 93, 190401 (2004)
- [66] Y. Aharonov and D. Bohm, Phys. Rev. A 115, 485 (1959)
- [67] J. Dalibard, F. Gerbier, G. Juzeliūnas, and P. Öhberg, Rev. Mod. Phys. 83, 1523 (2011)
- [68] N. Goldman, G. Juzeliūnas, P. Öhberg, and I.B. Spielman, Rep. Prog. Phys. 72, 126401 (2014)
- [69] N. Goldman, J.C. Budich, and P. Zoller, Nature 12, 639 (2016)
- [70] T. Ozawa, H. M. Price, A. Amo, N. Goldman, M. Hafezi, L. Lu, M. C. Rechtsman, D. Schuster, J. Simon, O. Zilberberg, and I. Carusotto, Rev. Mod. Phys. 91, 015006 (2018)

Chapter 2

Particle scattering by harmonically trapped quantum gases at finite temperatures

2.1 Introduction

In the existing literature, quantum scattering theory is discussed both for classical scatterers (which are either fixed or having classical motions in space [1]) and quantum scatterers e.g. quantum scattering by atoms, molecules, nuclei, etc [2]. 'Particle' can be scattered coherently from each and every point of the region of space of the quantum scatterer if it is fired onto the region, and carries information about the state of the scatterer after being scattered. There are some theoretical discussions on quantum scattering for unfixed quantum scatterer(s) bounded in a region of space, e.g. diffraction of atoms from a standing-wave Schrdinger field [3], scattering of slowly moving atoms by a 3D harmonically trapped Bose-Einstein condensate (BEC) within Bogoliubov-de Gennes formalism [4], particle scattering by a weakly interacting BEC[5, 6, 7, 8, 9, 10], transport of atoms across interacting BECs in a 1D optical lattice [11], a nondestructive method to probe a complex quantum system using multi-impurity atoms as quantum probes [12], particle scattering by quantum scatterers in restricted geometries [13], etc.

In none of the previous works, related to the quantum scatterers, temperature dependence of the scattering amplitude or that of the differential scattering cross-section was studied. Thus, we naturally take up discussion on quantum scattering to introduce quantum scattering with quantized motions of the scatterers in thermal equilibrium in harmonically trapped geometries as probe for Fermi-Huang δ_p^3 interactions (among the 'incident' particle and the scatterers), which although are easy to deal with have huge applications in the field of ultra-cold atoms [14, 15]. We are specially interested in temperature dependence of differential scattering cross-section for scatterers in the harmonically trapped geometry in this regard, as because, thermodynamic properties of ultra-cold gases in harmonic traps are of growing interest [15, 16, 17, 18].

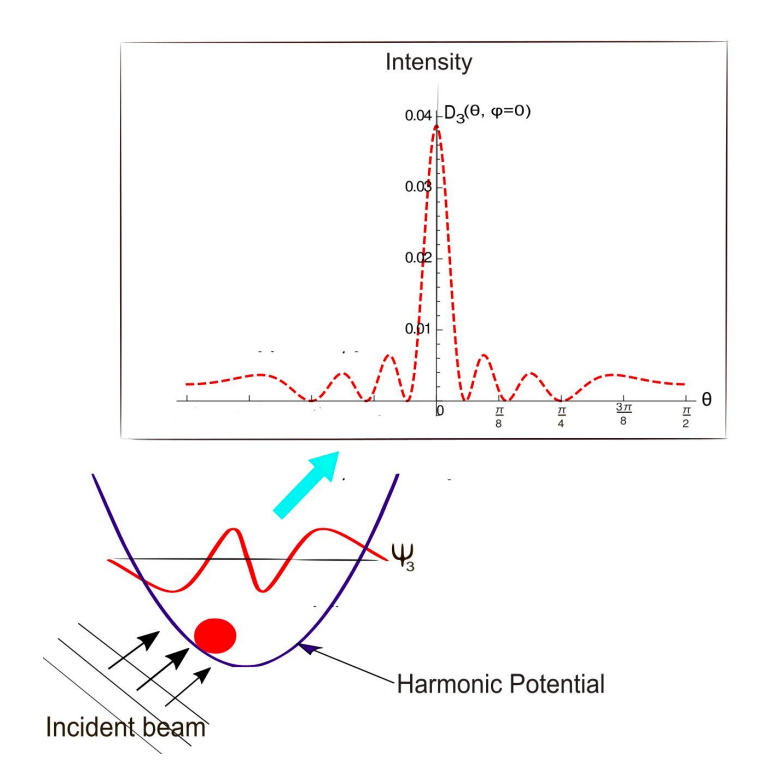


FIGURE 2.1: Intensity distribution $(D_3(\theta,\phi)=|f_3(\theta,\phi)|^2)$ along a line parallel to the x-axis for scattering of a 'particle' (e^{ikz}) by the 1-D harmonic oscillator along x-axis for a_s as unit length, $ka_s=5$, $\bar{\mu}\to m$, and $l_x/a_s=1$. Plots follow from Eqn.(2.8).

If a plane wave (e^{ikz}) associated with a free particle ('particle') of a fixed momentum ($\mathbf{p} = \hbar k \hat{k}$) is scattered by a fixed scatterer (situated at $\mathbf{r} = 0$) with an interacting potential $(V_{int}(\mathbf{r}))$, then spherical wave $(\frac{e^{ikr}}{r})$ goes out of the scatter with a scattering amplitude $(f(\theta, \phi))$ to a particular direction $(\theta \text{ and } \phi)$ with respect to the initial direction (k). Now, if the scatterer is not fixed, say, the scatterer is a particle in a 1-D simple harmonic oscillator ($-\infty < x_0 < \infty$), then the 'particle' would be scattered coherently from all the positions ($\{x_0\}$) with probability density $|\psi_n(x_0)|^2$ where $\psi_n(x_0)$ (n = 0, 1, 2, ...) is the normalized eigenstate of the scatterer. In this case, after being scattered from all of the scattering sources points ($\{x_0\}$), the spherical waves ($\frac{e^{ikr}}{r'}$) will go out. To a particular direction (θ, ϕ) at a distance $\mathbf{r} = \mathbf{x}_0 + \mathbf{r}'$ from the center of the oscillation, all the outgoing spherical waves $(\{\frac{e^{ikr'}}{r'}\})$ interfere with different phases and give rise to a coherent scattering amplitude $f_n(\theta, \phi)$ which now depends on the quantum state ($|\psi_n>$) of the scatterer. Small angle neutron scattering by quantum dots was investigated by Pinero et al without precisely probing quantized motions of the scatterers in them [19]. Particle scattering by coherent media was also studied experimentally by Chikkatur et al [20] and Bromley et al [21]. While Bromley et al did not probe quantized motions of the scatterers in the dense medium, Chikkatur et al, could probe quantized motion of the scatterers, to a certain extent, in a BEC; though they did not probe angular dependence of the scattering amplitude. However, electron scattering by harmonically trapped BEC [22] and Fermi gas [23] was studied theoretically for $T \to 0$. Although temperature dependence in particle scattering by a BEC was studied by Montina [7], he did not consider quantized motions of the bosonic scatterers. About light scattering by a BEC or by ultra-cold atoms in optical trap, the experimental work of Schneble et al in [24], the recent theoretical work of Ezhova et al in [25], Zhu et al in [26] and Kozlowski et al in [27], the review work of Mekhov and Ritsch in [28],and the references therein are quite interesting. Above all, temperature dependence of the differential scattering cross-section, for particle scattering with quantized motion(s) of the scatterer(s) in harmonic/otical trap, has not been studied so far.

This article begins with revisiting of the quantum theory of particle scattering for a fixed (classical) scatterer with Fermi-Huang potential (i.e. regularized δ^3 potential: $V_{int}(\mathbf{r}) = g\delta_p^3(\mathbf{r}) = g\delta^3(\mathbf{r})\frac{\partial}{\partial r}r$). Then we have generalized the theory for quantum scatterer(s) in restricted geometries, in particular, for bosonic/fermionic scatterer(s) in a (i) 1-D harmonic trap, (ii) 2-D harmonic trap, and (iii) 3-D harmonic trap. Then we have calculated the scattering amplitudes, and have plotted the differential scattering cross-sections for all the cases. We also have investigated temperature dependence of the differential scattering cross-sections for the above cases, and specially emphasized on the differential cross-section for particle scattering by BEC(s) in the 3-D harmonic trap [29], double well trap, and the optical lattice.

2.2 Particle scattering by a single scatterer in a harmonic trap

In quantum scattering theory of particle scattering we deal with the time independent Schrödinger equation

$$\left(-\frac{\hbar^2}{2m}\nabla^2 + V_{int}(\mathbf{r})\right)\psi(\mathbf{r}) = E\psi(\mathbf{r}). \tag{2.1}$$

Scattering of an incident particle of mass m and the given momentum $\hbar k \hat{k}$, is recast, as scattering of a 'particle' (i.e. scattering of the plane wave $\psi_{in} \equiv e^{ikz}$) by the interacting potential $V_{int}(\mathbf{r})$, into an outgoing spherical wave $\psi_{out} \equiv \frac{e^{ikr}}{r}$. General form of the solution to Eqn. (2.1), in the radiation zone, takes the form [1]

$$\psi(\mathbf{r}) = \psi(r,\theta,\phi) \simeq A \left[e^{ikz} + f(\theta,\phi) \frac{e^{ikr}}{r} \right], \quad (2.2)$$

where $|A|^2$ is proportional to the intensity of the incident 'particle'. From this information, we can

eikz D Z

FIGURE 2.2: In the figure the scattered wave vector related to incident wave vactor is $\vec{k}' = k(\sin\theta\cos\phi\hat{i} + \sin\theta\sin\phi\hat{j} + \cos\theta\hat{k})$. Only along the z-direction the momentum is shifted.

find out the scattering (probability) amplitude $(f(\theta, \phi))$ of the out going spherical wave to a particular direction (θ, ϕ) in usual convention) with respect to the direction

of the incidence. The scattering amplitude, for $V_{int}(\mathbf{r}) = g\delta_p^3(\mathbf{r})$, with all orders of the Born series, takes the form [30, 31, 32, 15]

$$f(\theta,\phi) = -\frac{mg}{2\pi\hbar^2 (1 + ik\frac{mg}{2\pi\hbar^2})}.$$
 (2.3)

In Eqn. (2.3), The scatterer has been assumed to be fixed. If it is not fixed but is moving relative to the incident particle and the interaction potential is unchanged, then the scattering amplitude would change to

$$f(\theta,\phi) = -\frac{\bar{\mu}g}{2\pi\hbar^2 (1 + ik\frac{\bar{\mu}g}{2\pi\hbar^2})},$$
 (2.4)

where $\bar{\mu} = \frac{mM}{m+M}$ is the reduced mass and M is the mass of the scatterer [15]. The scattering amplitude is independent of θ and ϕ for low energy scattering, so that, s-wave scattering length can be conveniently defined, for low energy scattering, as $a_s = \lim_{k \to 0} -f(\theta, \phi)$. Thus, we quantify the coupling constant, as $g = \frac{2\pi\hbar^2 a_s}{\bar{\mu}}$.

2.2.1 For a single scatterer in a 1D harmonic trap

If **r** be the position of the incident particle such that, $\mathbf{r} = \mathbf{0}$, the center of the trapped potential, is the origin, then the δ_p^3 interaction, as previously expressed, the interaction between the incident particle at **r** and the scatterer at $x0\hat{i}$ can be written as follows:

$$V_{int}(\mathbf{r}) = g\delta_p^3(\mathbf{r} - x_0\hat{i}). \tag{2.5}$$

Eqn. (2.3) can be recast, using Eqn. (2.5), for this problem, as

$$f(\theta,\phi) = -\frac{mg_k}{2\pi\hbar^2}e^{i(\mathbf{k}-\mathbf{k}')\cdot x_0\hat{i}} = -\frac{mg_k}{2\pi\hbar^2}e^{-i\mathbf{k}'\cdot x_0\hat{i}}(2.6)$$

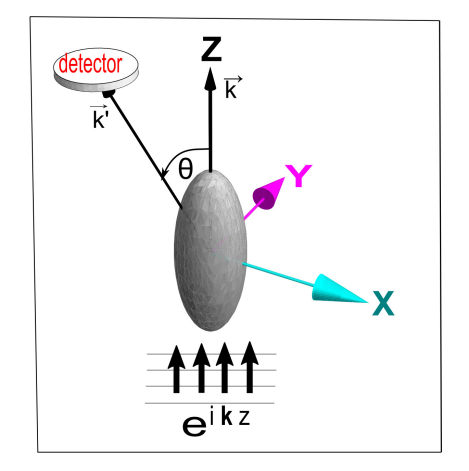


FIGURE 2.3: A schematic diagram for particle scattering by a harmonically trapped BEC.

where $g_k = \frac{g}{1+ika_sm/\bar{\mu}}$. Eqn. (2.6) is correct only if the scattering has happened only from $\mathbf{r} = x_0\hat{i}$, and will not be correct if $x_0\hat{i}$ is not a fixed point. Although we can consider Eqn. (2.6) where there is a relative motion (between the particle and scatterer) by replacing mass of the 'particle' by the reduced mass, yet the scatterer is still classical as we have not quantized the motion of the scatterer. Let us now consider quantized motion of the scatterer(s) into the theory of quantum scattering, and begin with the scatterer as a particle in a 1-D harmonic trap potential $V(\mathbf{r}_0) = \frac{1}{2}M\omega_x^2x_0^2$ where ω_x is the angular frequency of oscillations, $M(M\gg m)$ is the mass and $\mathbf{r}_0=x_0\hat{i}$ is the position of the scatterer such that $-\infty < x_0 < \infty$. We again consider the scatterer to scatter the incident 'particle', Ae^{ikz} , by the interacting potential $V_{int}(\mathbf{r})=g\delta_y^3(\mathbf{r}-x_0\hat{i})$. Scattering amplitude, if the

scatterer is fixed at $\mathbf{r} = x_0 \hat{i}$, would be the same as that in Eqn. (2.6) as $f(\theta, \phi) = -\frac{mg_k}{2\pi\hbar^2}e^{-i\mathbf{k}'\cdot x_0\hat{i}}$. Normalized energy eigenstate of the scatterer, corresponding to the energy eigenvalue $E_{n_x} = (n_x + 1/2)\hbar\omega_x$, can be written, as [1]

$$\psi_{n_x}(x_0) = \sqrt{\frac{1}{\sqrt{\pi}l_x}} \frac{1}{\sqrt{2^n n!}} H_{n_x}(x_0/l_x) e^{-x^2/2l_x^2}, \tag{2.7}$$

where $l_x = \sqrt{\hbar/M\omega_x}$ is the confining length scale of the scatterer, and $H_{n_x}(x_0/l_x)$ is the Hermite polynomial of degree $n_x = 0, 1, 2, ...$ Now, the quantum scattering is happening from all the points $-\infty < x_0 < \infty$ simultaneously with respective probability density $\{|\psi_n(x_0)|^2\}$. Thus, the scattering amplitude for the scatterer in the quantum state $|\psi_n\rangle$, can be written, using Eqn. (2.6), as

$$f_{n_x}(\theta,\phi) = -\frac{mg_k}{2\pi\hbar^2} \int_{-\infty}^{\infty} e^{-i\mathbf{k}'\cdot x_0\hat{l}} |\psi_{n_x}(x_0)|^2 dx_0$$

$$= -\frac{mg_k}{2\pi\hbar^2} e^{-q_x^2 l_x^2} L_{n_x}(2q_x^2 l_x^2), \qquad (2.8)$$

where $q_x = k \sin(\theta) \cos(\phi)/2$ as defined before, and $L_{n_x}(2q_x^2l_x^2)$ is the Laguerre polynomial of degree n_x [33]. We show the profile of the differential scattering cross-section $(D_{n_x}(\theta,\phi) = |f_{n_x}(\theta,\phi)|^2)$ or the 1D case in figure 2.1 for quantum number $n_x = 3$.

2.3 For a single scatterer in a 2D harmonic trap

For 2-D case, the trap potential would be $V(\mathbf{r}_0) = \frac{1}{2}M\omega_x^2x_0^2 + \frac{1}{2}M\omega_y^2y_0^2$ where ω_y is the angular frequency of oscillations along y direction, and $\mathbf{r}_0 = x_0\hat{i} + y_0\hat{j}$ is the position of the scatterer such that $-\infty < y_0 < \infty$. We again consider, that, the scatterer to scatter the incident 'particle', Ae^{ikz} , by the interacting potential $V_{int}(\mathbf{r}) = g\delta_p^3(\mathbf{r} - x_0\hat{i} - y_0\hat{j})$. Thus, scattering amplitude, for the 2-D case, would be, in the separable form

$$f_{n_x,n_y}(\theta,\phi) = -\frac{mg_k}{2\pi\hbar^2} e^{-q_x^2 l_x^2 - q_y^2 l_y^2} L_{n_x}(2q_x^2 l_x^2) L_{n_y}(2q_y^2 l_y^2)$$
(2.9)

where $\psi_{n_x,n_y}(x_0,y_0)$ is the normalized energy eigenstate of the scatterer with energy eigenvalue $E_{n_x,n_y}=(n_x+1/2)\hbar\omega_x+(n_y+1/2)\hbar\omega_y$ and $n_y=0,1,2,...$

2.3.1 For a single scatterer in a 3D harmonic trap

Above generalization, however, is not obvious for the scatterer in a 3-D harmonic trap potential $V(\mathbf{r}_0) = \frac{1}{2}M\omega_x^2x_0^2 + \frac{1}{2}M\omega_y^2y_0^2 + \frac{1}{2}M\omega_z^2z_0^2$ as because we further have to consider momentum transfer mechanism for the motion of the scatterer along the z direction since the incident 'particle' has momentum only along the z direction. For this reason, generalization Eqn.(2.6), for an arbitrary fixed position $\mathbf{r}_0 = x_0\hat{i} + y_0\hat{j} + z_0\hat{k}$ in 3-D, would be $f(\theta,\phi) = -\frac{mg_k}{2\pi\hbar^2}e^{-i\mathbf{k}'\cdot(x_0\hat{i}+y_0\hat{j})+i(\mathbf{k}-\mathbf{k}')\cdot z_0\hat{k}}$. Thus, 3-D

generalization of Eqn. (2.9) would be in the separable form

$$f_{n_{x},n_{y},n_{z}}(\theta,\phi) = -\frac{mg_{k}}{2\pi\hbar^{2}} \int e^{-i\mathbf{k}'\cdot(x_{0}\hat{i}+y_{0}\hat{j})+i(\mathbf{k}-\mathbf{k}')\cdot z_{0}\hat{k}} \\
\times |\psi_{n_{x},n_{y},n_{z}}(x_{0},y_{0},z_{0})|^{2} d^{3}\mathbf{r}_{0} \\
= -\frac{mg_{k}}{2\pi\hbar^{2}} e^{-q_{x}^{2}l_{x}^{2}-q_{y}^{2}l_{y}^{2}-\bar{q}_{z}^{2}l_{z}^{2}} \\
\times L_{n_{x}}(2q_{x}^{2}l_{x}^{2})L_{n_{y}}(2q_{y}^{2}l_{y}^{2})L_{n_{z}}(2\bar{q}_{z}^{2}l_{z}^{2}), \tag{2.10}$$

where $\psi_{n_x,n_y,n_z}(x_0,y_0,z_0)$ is the normalized energy eigenstate of the quantum scatterer in the 3-D harmonic trap with energy eigenvalue $E_{n_x,n_y,n_z}=(n_x+1/2)\hbar\omega_x+(n_y+1/2)\hbar\omega_y+(n_z+1/2)\hbar\omega_z, n_z=0,1,2,...,\omega_z$ is the angular frequency of oscillation of the scatterer along the z direction, $l_z=\sqrt{\hbar/M\omega_z}$, and $\bar{q}_z=-k(1-\cos\theta)/2=-k\sin^2(\theta/2)$ which acts like an obliquity factor. Differential scattering cross-section for the 3-D harmonic scatterer, can be obtained from Eqn. (2.10), as

$$D_{n_{x},n_{y},n_{z}}(\theta,\phi) = \left| \frac{mg_{k}}{2\pi\hbar^{2}} e^{-q_{x}^{2}l_{x}^{2} - q_{y}^{2}l_{y}^{2} - \bar{q}_{z}^{2}l_{z}^{2}} \times L_{n_{x}}(2q_{x}^{2}l_{x}^{2})L_{n_{y}}(2q_{y}^{2}l_{y}^{2})L_{n_{z}}(2\bar{q}_{z}^{2}l_{z}^{2}) \right|^{2}.$$

$$(2.11)$$

Eqn. (2.10), though it goes beyond the first Born approximation, is fully consistent (for $ka_s \ll 1$) with the result obtained by Bodefeld and Wilkens after truncating the Lippmann-Schwinger equation to the level of the first Born approximation [3]. Averaging over the position of the scatterer in Eqn. (2.10) (and that in the preceding two as well) is justified by the fundamental principle of superposition¹, that if we do not know the initial position of the scatterer rather know only its energy eigenstate $|\psi_{n_x,n_y,n_z}\rangle$ then the scattering takes place from all the points $\{\mathbf{r}_0\}$ of the scatterer with the respective probability densities $\{|\psi_{n_x,n_y,n_z}|^2\}$. We are considering the energy eigenstate to be unaltered in the process of scattering. Energy eigenstate $|\psi_{n_x,n_y,n_z}\rangle$ would change in the process of inelastic scattering [3]. We will discuss the reasons in the concluding section to justify less probability of the inelastic scattering in the context of thermal and many-body effects [4].

2.4 Particle scattering by Bose and Fermi gases in thermodynamic equilibrium in 3D harmonic traps

Let us now consider N identical ideal scatterers in the 3-D harmonic trap [16, 15]. Above expression in Eqn. (2.10) can be generalized for these scatterers, all of which scatter the incident 'particle' (Ae^{ikz}) by the same delta potential ($V_{int}(\mathbf{r}) = \sum_{j=1}^{N} g \delta_p^3 (\mathbf{r} - \mathbf{r})$

¹The superposition principle is often applied in a similar way for the light scattering (diffraction) by a double slit. Please see [34] for the same.

 ${\bf r}_{0i}))$, as

$$f_{\mathbf{n}_{1},\mathbf{n}_{2},...,\mathbf{n}_{N}}(\theta,\phi) = -\frac{mg_{k}}{2\pi\hbar^{2}}e^{-||\bar{\mathbf{q}}\cdot\mathbf{l}||^{2}}\sum_{\mathbf{n}_{j=1}}^{\mathbf{n}_{j=N}}L_{n_{jx}}(2q_{x}^{2}l_{x}^{2}) \times L_{n_{iy}}(2q_{y}^{2}l_{y}^{2})L_{n_{iz}}(2\bar{q}_{z}^{2}l_{z}^{2}), \qquad (2.12)$$

where $\mathbf{n}_j = (n_{jx}, n_{jy}, n_{jz})$ represents quantum numbers corresponding the energy eigenstate of the jth oscillator, and $||\mathbf{\bar{q}} \cdot \mathbf{l}||^2 = q_x^2 l_x^2 + q_y^2 l_y^2 + \bar{q}_z^2 l_z^2$. Eqn. (2.12), however, is applicable not only for distinguishable scatterers, but also for Bose and Fermi scatterers as all the energy eigenstates are orthogonal.

Let us now consider the ideal scatterers in thermodynamic equilibrium with its surroundings at temperature T and chemical potential μ . Scattering amplitude for the scatterers would now depend upon the temperature and chemical potential, and can be written, as

$$\bar{f}_{T}(\theta,\phi) = -\frac{mg_{k}}{2\pi\hbar^{2}}e^{-||\bar{\mathbf{q}}\cdot\mathbf{l}||^{2}} \sum_{\mathbf{n}=(0,0,0)}^{(\infty,\infty,\infty)} \bar{n}_{\mathbf{n}}L_{n_{x}}(2q_{x}^{2}l_{x}^{2}) \times L_{n_{y}}(2q_{y}^{2}l_{y}^{2})L_{n_{z}}(2\bar{q}_{z}^{2}l_{z}^{2}), \tag{2.13}$$

where $\bar{n}_{\mathbf{n}} = \frac{1}{e^{(E_{\mathbf{n}}-\mu)/k_BT} + 1}$ represents no. of scatterers in the single-particle quantum state $\psi_{\mathbf{n}}(\mathbf{r}_0) = \psi_{n_x,n_y,n_z}(x_0,y_0,z_0)$ for Bose (–) or Fermi (+) scatterers, and $E_{\mathbf{n}} = E_{n_x,n_y,n_z} = (n_x+1/2)\hbar\omega_x + (n_y+1/2)\hbar\omega_y + (n_z+1/2)\hbar\omega_z$. Eqn. (2.13) is our prediction for the scattering amplitude for a harmonically trapped ideal Bose or Fermi gas at any temperature. For a single particle, $\bar{n}_{\mathbf{n}}$ in Eqn. (2.13) can be replaced by the Boltzmann probability $P_{\mathbf{n}} = e^{-E_{\mathbf{n}}/k_BT}/Z$ where $Z = \sum_{\mathbf{n}} e^{-E_{\mathbf{n}}/k_BT}$ is the partition function. We show temperature dependence of $\bar{D}_T(\theta,\phi) = |\bar{f}_T(\theta,\phi)|^2$ for a single particle in figure (2.5). We also show its statistics dependence in the figure 2.5.

For $T \to 0$, all (N) the Bose scatterers occupy the ground state. Differential scattering cross-section, in this situation, takes the form, from Eqn. (2.13), as

$$\bar{D}_{T\to 0}(\theta, \phi) = |\bar{f}_{T\to 0}(\theta, \phi)|^2 = |Na_k|^2 e^{-2||\bar{\mathbf{q}}\cdot\mathbf{l}||^2}, \tag{2.14}$$

where $a_k = \frac{mg_k}{2\pi\hbar^2} = \frac{a_s m/\bar{\mu}}{1+ika_s m/\bar{\mu}}$. We plot it in figure 2.6 for relevant values of parameters. Eqn. (2.14) leads to the scattering cross-section, for $k \to 0$, as

$$\sigma = \int_0^{\pi} d\theta \int_0^{2\pi} d\phi \bar{D}_{T\to 0}(\theta, \phi) \sin\theta = 4\pi |Na_s m/\bar{\mu}|^2. \tag{2.15}$$

On the other hand, for $T \to 0$, all the (N) Fermi scatterers (of the same spin component, say spin up) will occupy the first N single particle states. Thus, for large N and

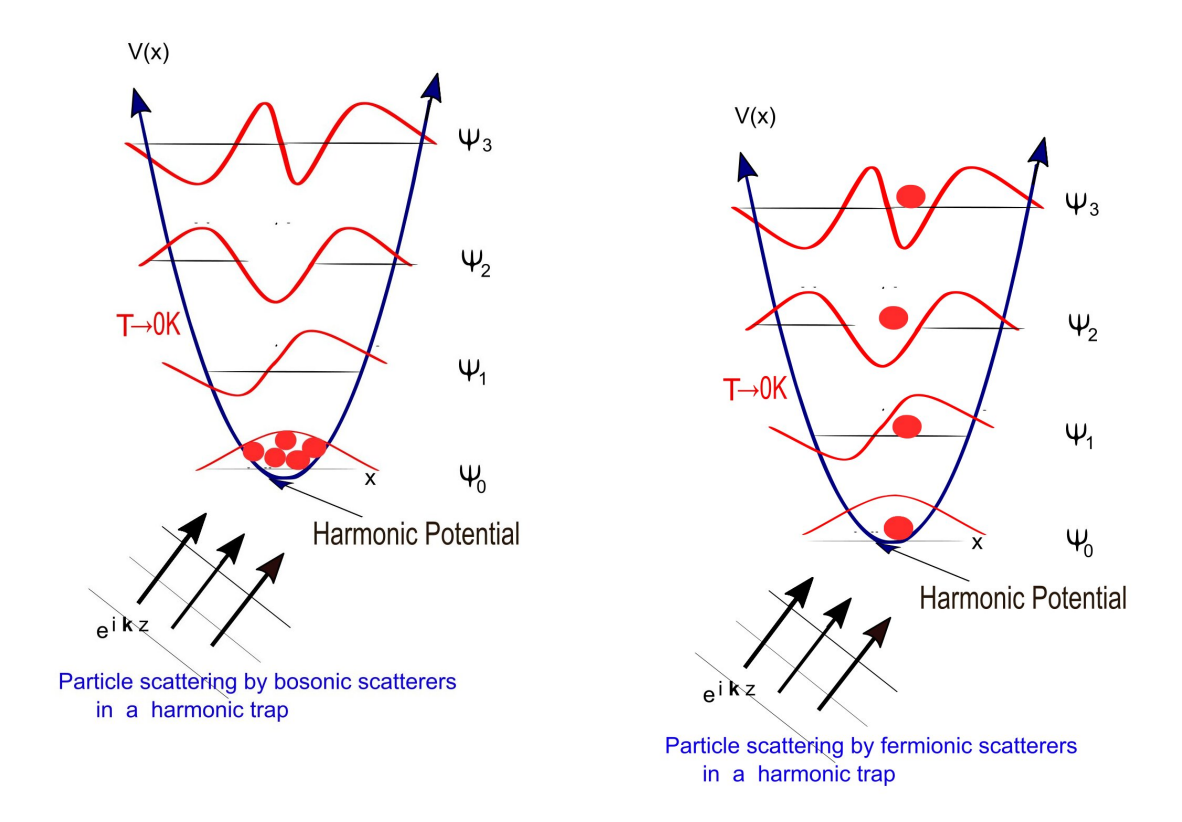


FIGURE 2.4: Particle scattering by a quantum gas of harmonic oscillator at $T \rightarrow 0$.

isotropic case, modulus squared of the r.h.s. of equation (2.13), takes the form², for harmonically trapped Fermi gas as

$$\bar{D}_{T\to 0}(\theta, \phi) = |Na_k|^2 e^{-4||\bar{\mathbf{q}}\cdot\mathbf{l}||^2 N^{1/3}}.$$
(2.16)

For classical scatterers $(n_x, n_y, n_z \to \infty)$, in contrary to the above, the scattering amplitude in Eqn. (2.13) would be infinitely narrow³ as shown in figure (2.6).

2.4.1 Weak interparticle interactions and finite size effects for Bose scatterers in a 3D harmonic trap

Temperature dependence of the scattering amplitude comes from the triple summation in Eqn. (2.13). The summation, in the thermodynamic limit, followed by the Taylor expansions of the Laguerre polynomials about k=0 with $q^2=(q_x^2+q_y^2+\bar{q}_z^2)$,

²As because, we can approximate $\sum_{n=0}^{\infty} e^{-n/N} L_n(x) = \frac{e^{\frac{1}{N} + \frac{x}{1-e^{\frac{1}{N}}}}}{-1+e^{\frac{1}{N}}}$ for $N \gg 1$, as $\sum_{n=0}^{N} L_n(x) \approx Ne^{-Nx}$.

³As because, for $n \gg 1$, we can write $L_n(x) \to e^{-nx}$ from the expression of the polynomial itself.

Dashed: T->0K, Dotted: T= 10^{-7} K, Solid: T-> ∞ ; k a_s = $2,l_x$ = l_y = l_z = a_s ; ω = 10^3 Hz, a_s =1 Unit $\overline{D}_{T}(\theta,0)/a_{s}^{2}$

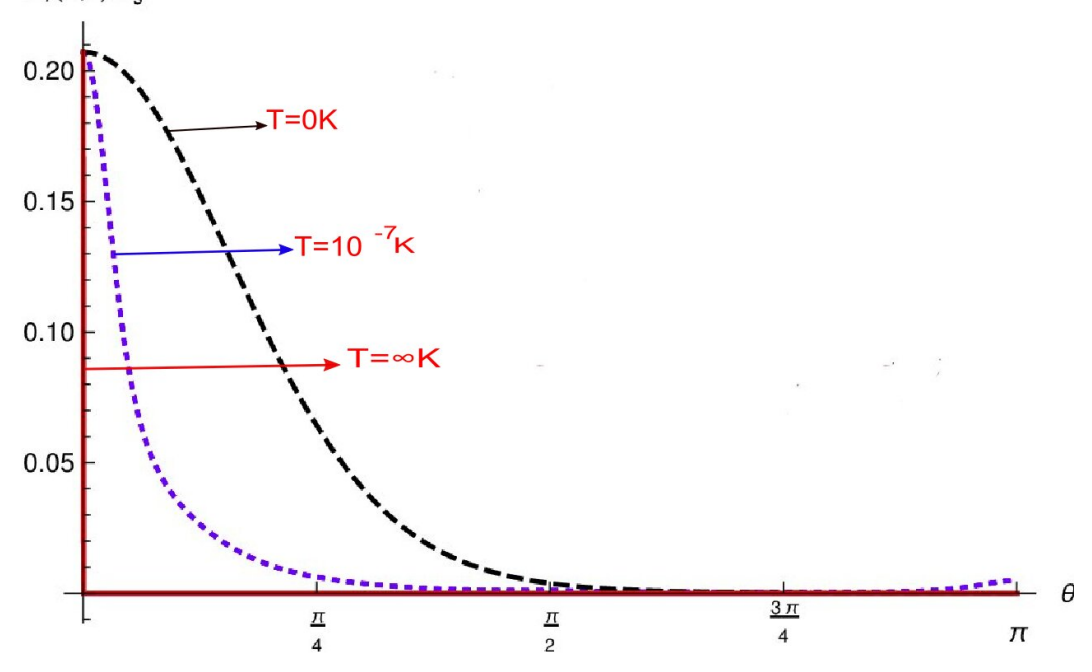


FIGURE 2.5: Intensity distribution or scattering of a particle by a 3D isotropic harmonic oscillator for a_s as unit length and m/M = 0.1 plot flows Eqn.2.13 with \bar{n}_n replaced by P_n . Dashed, dotted and solid lines correspond to $D_T(\theta,0)$ for $T \to 0, T \to 10^{-7}$, and $T \to \infty$

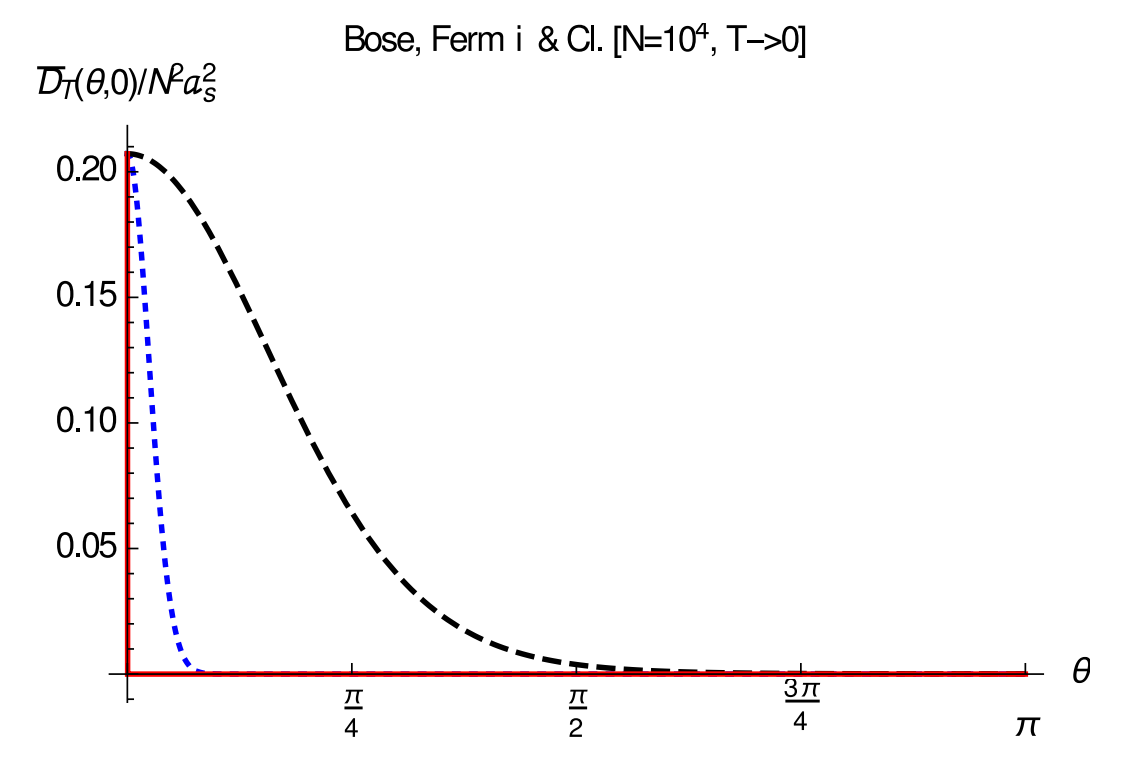


FIGURE 2.6: Intensity distribution for scattering of a 'particle' (e^{ikz}) by a 3-D isotropic harmonic oscillator for a_s as unit length and $\bar{\mu} \rightarrow$ m. Dashed, dotted and solid lines are linked to Bose gas (Eqn.(2.14)), Fermi gas (Eqn.(2.16)), and classical scatterers (Eqn.(2.13) for $n \to \infty$ limit) in the 3-D isotropic harmonic trap.

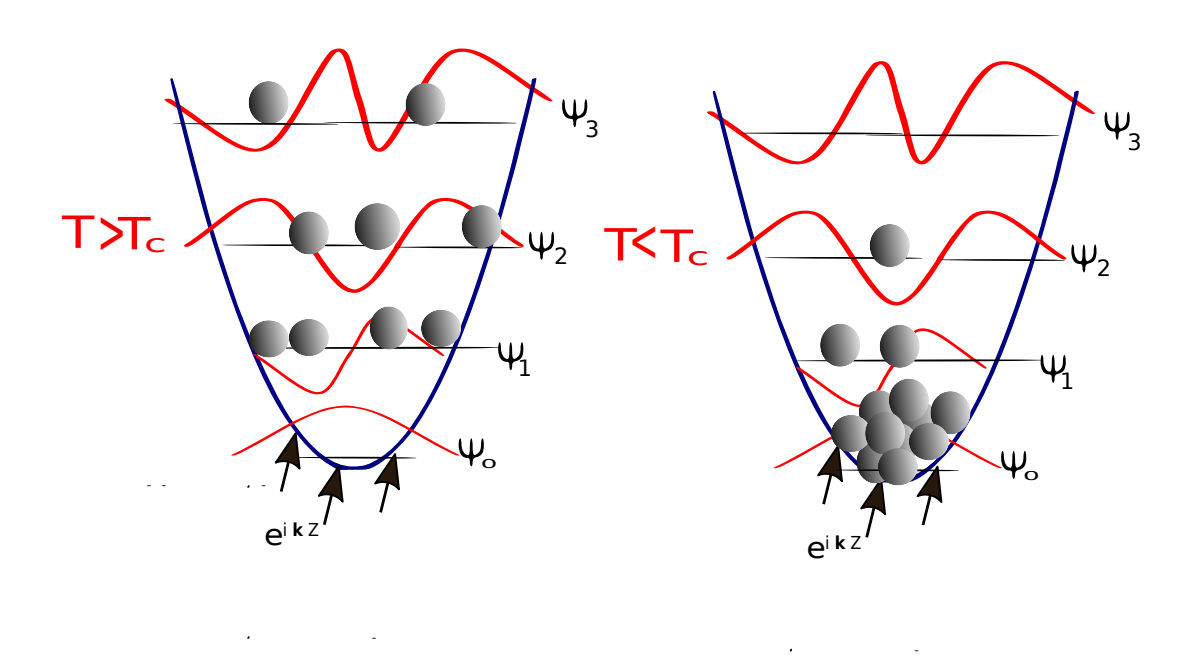


FIGURE 2.7: Particle scattering by Bose gas above and bellow the condensate temperature(T_c)

 $\omega_x=\omega_y=\omega_z=\omega$, $\bar{l}=\sqrt{\hbar/M\omega}$, $t=\frac{k_BT}{\hbar\omega}$, $z=e^{\mu/k_BT}$ and $N=t^3Li_3(z)$ takes the form $S=t^3Li_3(z)-6q^2\bar{l}^2t^4Li_4(z)+(q^2\bar{l}^2)^2[12t^5Li_5(z)+3t^4Li_4(z)]+O(q^6)$ for the Bose gas above the condensation point $(T>T_c=\frac{\hbar\omega}{k_B}[N/\zeta(3)]^{1/3})^4$ For $T< T_c$, similar form also appears with non-condensate fraction $(t/t_c)^3$ where $t_c=\frac{k_BT_c}{\hbar\omega}$. Condensate part shows temperature dependence only in the form of the condensate fraction $\frac{N_0}{N}=1-(t/t_c)^3$. Temperature dependence of $\bar{D}_T(\theta,\phi)=|\bar{f}_T(\theta,\phi)|^2$, for the Bose gas, with the appropriate temperature dependence of the chemical potential [35], is shown in second figure 2.8 . For Fermi gas, only change would be the replacement of $Li_j(z)$ by $-Li_j(-z)$ $\forall j$. For anisotropic trap, forms of the bulk quantities are mostly unaltered with the replacement $\omega=(\omega_x\omega_y\omega_z)^{1/3}$.

For the finite size of the trap and weak inter-scatterer interactions $V_{int} = \frac{4\pi\hbar^2\tilde{a}_s}{M}\sum_{l,j< i}\delta_p^3(\vec{r}_{0i}-\vec{r}_{0j})$, the condensate fraction, to the lowest order in \tilde{a}_s , takes the form $\frac{N_0}{N}=1-(t/t_c)^3-\frac{3t^2\zeta(2)}{2t_c^3\zeta(3)}-\frac{4.932t^{7/2}\tilde{a}_s}{t_c^3\zeta(3)\tilde{l}}$ within the Hartree-Fock (H-F) approximation [15, 36, 37]. Inter-scatterer interactions do not greatly modify Eqn. (2.13) as $N^{1/6}\tilde{a}_s/\tilde{l}\ll 1$. These interactions, apart from modifying the condensate fraction, can substantially scale $(\bar{l}\to\tilde{\ell})$ the typical confining length \bar{l} (i.e. l_x , l_y and l_z) in the exponent in Eqn. (2.13) keeping its form unaltered. Finite temperature scaling of \bar{l} , as prescribed in Ref.[38], is shown in figure 2.8 (a) for repulsive interactions. With both the modifications, we have shown corrections due to the finite size and the

⁴Here $Li_j(z)=z+\frac{z^2}{2^j}+\frac{z^3}{3^j}+\dots$ is a poly-logarithmic function of the argument z and order j. It is also known as a Bose-Einstein integral.

FIGURE 2.8: Second figure shows the temperature dependence of the differential scattering cross-section along the forward ($\theta=0$, dotted line), perpendicular ($\theta=\pi/2$, dashed line) and backward ($\theta=\pi$, solid lines) directions for 3-D harmonically trapped isotropic ideal Bose gas for the relevant parameters as mentioned above. Plots follow from Eqn. (2.13) for $\bar{\mu}\to m$. First figure (a)represents finite temperature scaling ($\bar{l}\to\tilde{\ell}$) of \bar{l} for the same system (within the 4th order in $\tilde{\ell}/\bar{l}-1$ in the H-F energy functional [38]) for the coupling constant $\frac{4\pi\hbar^2\tilde{a}_s}{M}$ with $\tilde{a}_s=90a_0=0.0056\bar{l}$ [39]. Dotted line in the inset-a represents finite size and inter-scatterer effects within the H-F approximation over the solid line which also represents backward scattering in the main figure

1.0

0.5

1.5

inter-scatterer interactions effects⁵ to the temperature dependence of $\bar{D}_T(\theta,\phi)$ specially for the backward scattering below T_c in figure 2.8 (inset-a). From the trend of the scaling, one can neglect the effect of interactions for $T > T_c$. However, effect of the interactions, for $T \to 0$, may not necessarily be perturbative, and can be better described within Thomas-Fermi approximation [4].

In second figure (2.8) inset a) we show the scaling result for the angular dependence θ of the differential scattering cross-section for the weakly interacting case of the BEC for $T \to 0$, and finite temperature and size effects over this result within the H-F approximation according to the prescription described above. It is quite clear from the plots in second figure (2.8)(a) that repulsive interactions lead to narrowing down the profile of the differential scattering cross-section around $\theta = 0$ as the condensate broadens up around $\theta = 0$. This is quite natural, as the scattering amplitude for the extended object (BEC) is Fourier decomposed at all the source points of scattering. However, if temperature increases, probability of excited states being occupied by the scatterers increases, which in turn increases probability of scattering to some larger angles like that shown in figure (2.1). Thus, increase of temperature leads to large angle scattering. However, coherency get reduced if scatterers are found in different energy eigenstates other than the ground state at a finite temperature. It results reduction of the scattering cross-section with the increase of temperature. This is true in general. This is also apparent in figure (2.6) both for ideal Bose and Fermi scatterers in harmonic traps. We will also investigate the same for interacting BECs in other trapped geometries like double-well trap and optical lattice trap.

2.5 Particle scattering by Bose scatters in other 3D optical traps

2.5.1 For Bose scatterers in a double-well potential

Let us now consider an ideal gas of 2N Bose scatterers in a 3-D double-well potential $V(\mathbf{r}_0) = -M\omega_x^2x_0^2/2 + M\omega_x^2x_0^4/4d^2 + 2M\omega_y^2y_0^2/2 + 2M\omega_z^2z_0^2/2$, such that, frequency of oscillation is the same as that in the previous case, and the minima of double-well are separated along x-axis by a distance d [40, 15]. In thermodynamic equilibrium, for $T \to 0$, all the particles condense to the ground state. Within the tight-binding approximation (which is very good for $d \gg l_x$), there would be two distinct condensates of N scatterers in each well, such that each of the condensates scatters the incident 'particle' (Ae^{ikz}) like that in Eqn. (2.14). However, net scattering amplitude would be the superposition of the scattering amplitudes corresponding to the individual condensate as the setup is analogue of the double slit experiment [15, 41].

⁵Both the effects are comparable for $0 \lesssim T \lesssim T_c$.

(a) For a scatterer in a 3-D harmonic trap $D_{n_x,n_y,n_z}(\theta,0)/a_s^2$ 0.20 Dotted: n_x =0, n_y =0, n_z =0 Solid: $n_x = 5$, $n_y = 1$, $n_z = 0$ Dashed: $n_x = 20$, $n_y = 20$, $n_z = 20$ 0.15 0.10 0.05 θ 0.5 1.5 2.5 1.0 2.0 3.0 $\overline{D}_T(\theta,0)/(Na_s)^2$ (b) For a BEC in a 3-D harmonic trap 0.20 0.15 0.10 0.05 θ <u>π</u> 2 <u>3π</u> <u>π</u> π

FIGURE 2.9: The figures shows the total differential scattering cross-section for quantum scatterer(s) in trapped geometry. For all the figures, we have considered the following: $l_x=100$ nm, $l_x=l_y=l_z/2$, $kl_x=2$, $a_s/l_x=1$, and $\bar{\mu}\to m$. Solid, dotted and dashed lines in figure 2.9 (a) follow Eqn. (2.11) for $n_x=5$, $n_y=1$, $n_z=0$, $n_x=0$, $n_y=0$, $n_z=0$ and $n_x=20$, $n_y=20$, $n_z=20$ respectively. While the solid lines in (b) figures represent non-interacting BEC(s), the dotted lines in the same figures represent scaling results for interacting BEC(s) with $\tilde{a}_s=90a_0=0.0056\bar{l}$ as set in figure 2.8, and dashed lines represent finite temperature and size effects over the dotted lines within the H-F approximation for $T/T_c=0.1$

Thus, scattering from the two condensates would interfere, as

$$\bar{D}_{T\to 0}(\theta,\phi) = |Na_k|^2 e^{-2||\bar{\mathbf{q}}\cdot\mathbf{l}||^2} \left[2\cos\left(\frac{\pi d\sin(\theta)}{\lambda}\right)\right]^2. \tag{2.17}$$

Here we did not consider any Josephson oscillation as $d \gg l_x$ [42, 43]. We plot the differential cross-section in figure (2.10)(b) for relevant values of parameters. In the same figure we further present scaling results for weakly interacting Bose scatterers in the double-well trap well below the condensation point and finite temperature and size effects within the H-F approximation on top of the tight binding approximation in a similar way as prescribed in the previous section for the Bose scatterers in the harmonic trap.

2.5.2 For Bose scatterers in a 1D optical lattice

Let us now consider N' 3-D noninteracting BECs in a 1-D optical lattice [44, 17], such that two consecutive condensates are separated along x-axis by the lattice spacing d. Entire system is in thermodynamic equilibrium. For $T \to 0$, all the condensates have the same (N) number of particles. So, the system essentially is a 1-D grating of 3-D condensates. Within the tight-binding approximation, there would be N' distinct condensates of N scatterers in each well, such that each of the condensates scatters the incident 'particle' (Ae^{ikz}) like that in Eqn. (2.14) [45, 15]. However, net scattering amplitude would be the superposition of the scattering amplitudes corresponding to the individual condensate as the setup is now analogue of the 1-D grating experiment. Thus, scattering from the N' condensates would interfere, as

$$\bar{D}_{T\to 0}(\theta, \phi) = |Na_k|^2 e^{-2||\bar{\mathbf{q}}\cdot\mathbf{l}||^2} \left[\frac{\sin(\frac{N'\pi d\sin(\theta)}{\lambda})}{\sin(\frac{\pi d\sin(\theta)}{\lambda})} \right]^2.$$
 (2.18)

Since $d\gg l_x$, Eqn. (2.18) is good for the Mott insulator phase of the condensates. We plot $\bar{D}_{T\to 0}(\theta,\phi)$ in figure 2.11(b) for relevant values of parameters. In the same figure we further present scaling results for weakly interacting Bose scatterers in the optical lattice trap well below the condensation point and finite temperature and size effects within the H-F approximation on top of the tight binding approximation in a similar way as prescribed in the previous section for the Bose scatterers in the harmonic trap.

Again we see, in figures 2.10 b) and 2.11 b), according to our expectation, that repulsive interactions lead to narrowing down the profile of the differential scattering cross-section around $\theta=0$ as the condensates broaden up around $\theta=0$. Increase of temperature, as expected and explained before, leads to large angle scattering also for the scatterers in the double-well trap and the optical lattice trap. Coherency would be lost in presence of the disorders in the BECs. In this situation the differential scattering cross-sections in the figures 2.11 b)and 2.10 b) would be infinitesimally narrow like that shown by the solid lines in the figure 2.5

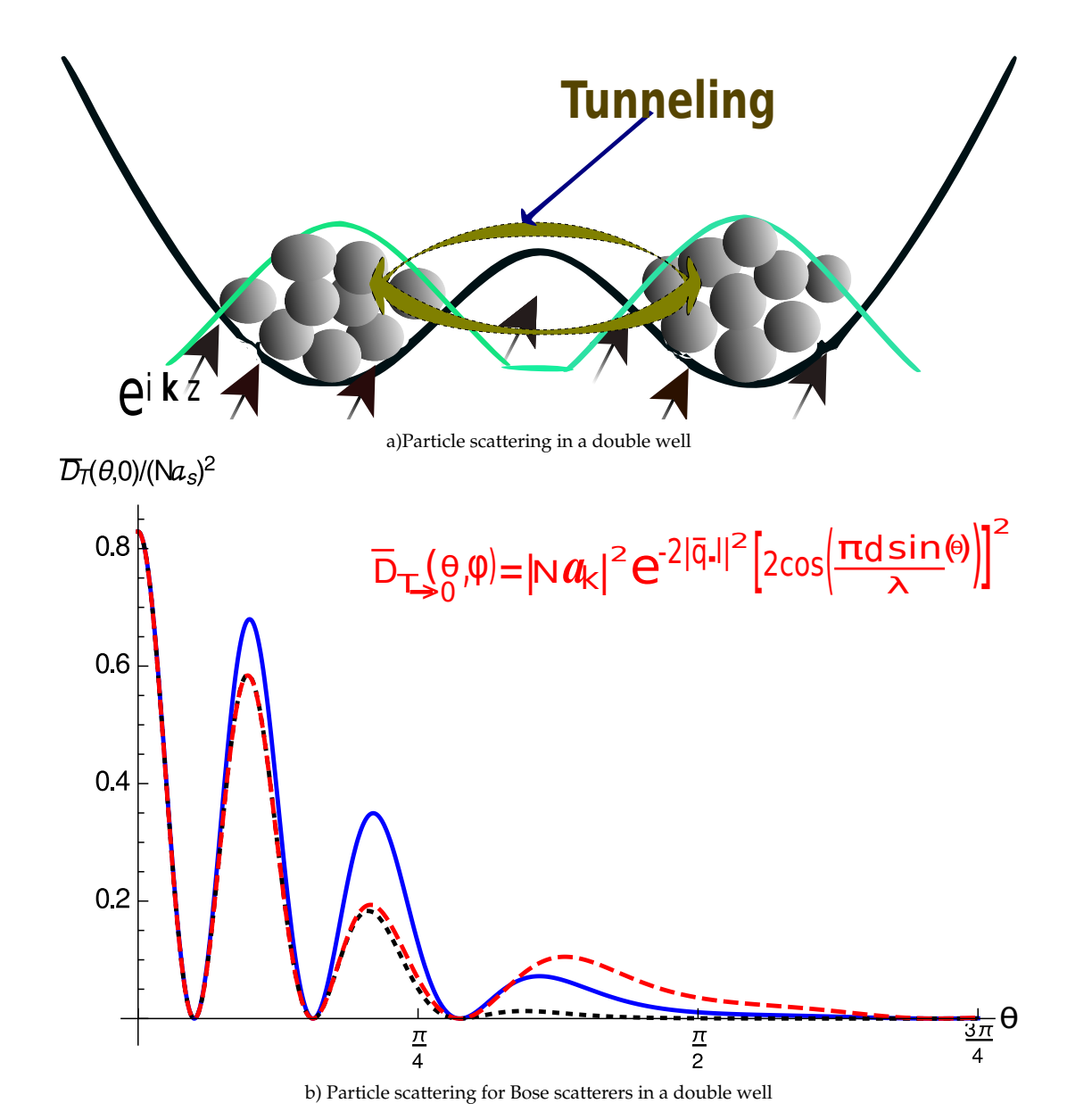
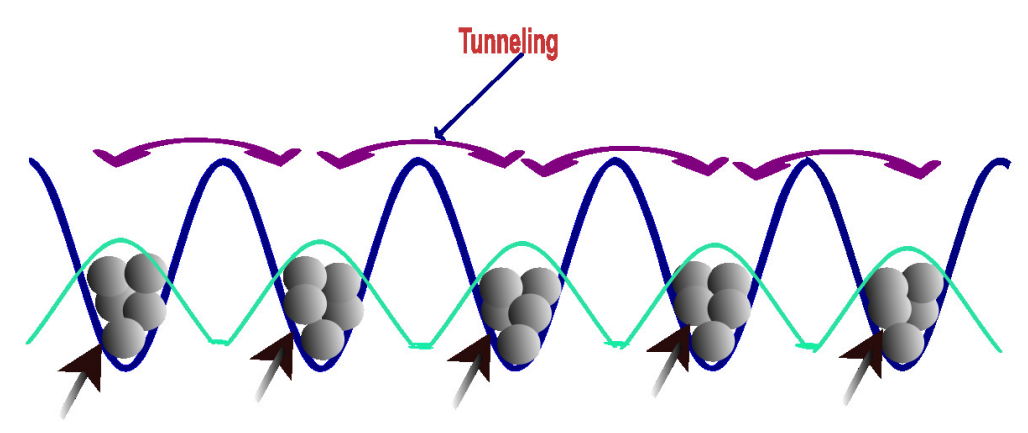
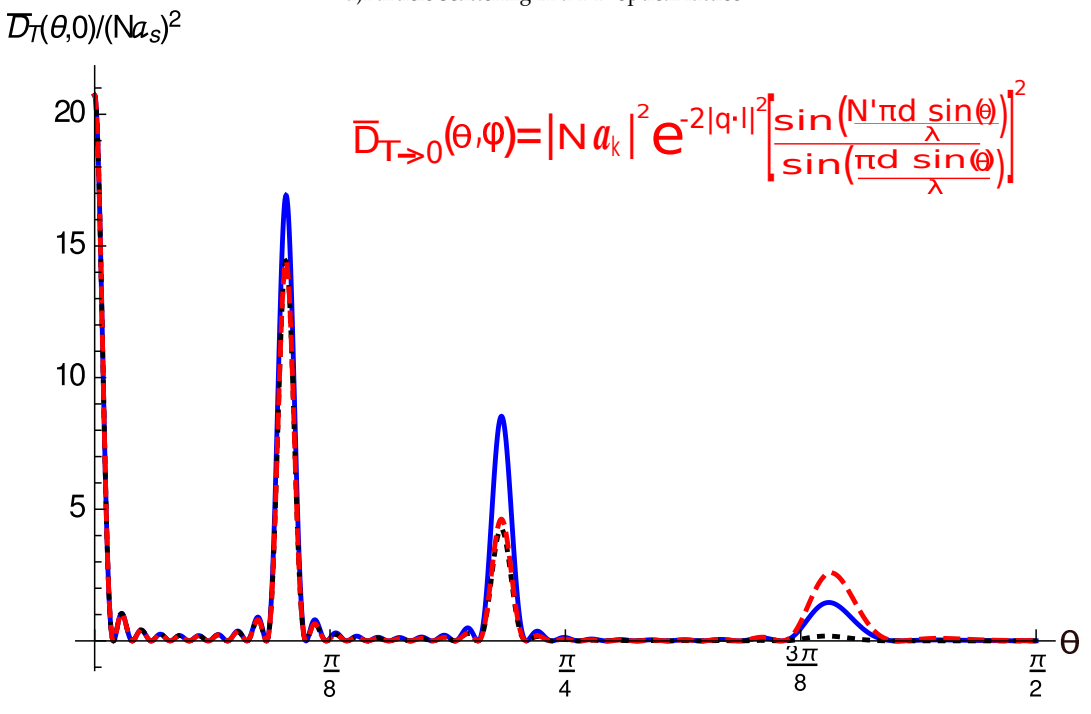


FIGURE 2.10: Figure a) represents a schematic diagram for particle scattering in a double well. Figure 2.10 (b) represents Eqn.(2.17) for $d=10\,l_x$. While the solid lines in (b)figure represents non-interacting BEC(s), the dotted lines in the same figures represent scaling results for interacting BEC(s) with $\tilde{a}_s=90a_0=0.0056\bar{l}$ as set in figure 2.10 b), and dashed lines represent finite temperature and size effects over the dotted lines within the H-F approximation for $T/T_c=0.1$



a)Particle scattering in a 1-D optical lattice



b)Particle scattering for Bose scatterers in a 1D optical lattice.

FIGURE 2.11: Figure a) represents a schematic diagram for particle scattering in a 1-D optical lattice . Fig. 2.11 (b) represents Eqn.(2.18) for $d=10\,l_x$ and N'=10. While the solid lines in (b)figures represent non-interacting BEC(s), the dotted lines in the same figures represent scaling results for interacting BEC(s) with $\tilde{a}_s=90a_0=0.0056\bar{l}$ as set in figure 2.11 b), and dashed lines represent finite temperature and size effects over the dotted lines within the H-F approximation for $T/T_c=0.1$

2.6. Conclusions 63

2.6 Conclusions

To conclude, we have presented quantum theory of particle scattering by quantum scatterers in quantized bound states in harmonically trapped geometry for Fermi-Huang δ_p^3 interactions (between the incident particle and the scatterers), which although are easy to deal with have huge applications in the field of ultra-cold atoms [14, 15]. Particle scattering by the quantum scatterer(s) in thermal equilibrium has not been investigated before us except for $T \to 0$ [4, 23, 22]. Temperature dependence of the differential scattering cross-sections, as shown in Fig.2.6, would be an important tool to distinguish type (bosonic/fermionic) of the scatterers. The discontinuities in the slops of $\bar{D}_T(\theta,\phi)$ s at $T=T_c$, except for the forward scattering as shown in figure 2.8, can be used to detect occurrence of BEC by particle scattering method. Our predictions can be tested within the present day experimental setups.

Just by looking into the scattering intensity-pattern for sufficiently large energy of the incident 'particle', as shown in figure 2.1, and counting the maximum number of the zeros of the differential scattering cross-section along x-axis, one can easily determine energy eigenstate of 1-D harmonic oscillator, as number of the zeros along the x axis is equal to quantum number n_x . From the highest possible peak height of the forward differential scattering cross-section for a scatterer in the harmonic oscillator, one can easily determine scattering length (a_s) of the incident 'particle' as the height, for low energy of the incident 'particle', is proportional to a_s^2 .

We have constructed our theory for a single incident 'particle'. For a beam of \bar{N} incident 'particles', A in Eqn. (2.2) would be replaced by $\sqrt{\bar{N}}A$, and all the results which depend on 'A' would be scaled accordingly. However, the scattering amplitude, the differential scattering cross-section, and the total scattering cross-section are independent of 'A'. So, all our result would be unaltered under this scaling.

Parameters used for plotting the figures are not specific to a particular scattering problem. However, we set m/M = 0.1 which would be appropriate for 40K as (fermionic) scatterer and 4He as the scattered particle. The ratio of m/M though would be even less (0.046) for the combination of ^{87}Rb (bosonic scatterer) and ^{4}He (scatterer particle), our results would not change much, as $m/\bar{\mu}$ for both the cases are approximately 0.91 and 0.96 respectively. We set $a_s/\bar{l}=1$ and $\tilde{a}_s/\bar{l}=0.0056$ (which is appropriate for ⁸⁷Rb atoms) to show a stronger effect due to the particle scattering than that due to inter-scatterer interactions. Values of ω and ka_s are set 1000 and 2 respectively to clearly show effect of temperature on particle scattering by a harmonic oscillator in the ultra-cold regime ($T \sim 10^{-7} K$). If k increases, the number of maxima and minima increases in the profile of the differential scattering cross-section. The number of maxima and minima further increases if the quantum number (i.e. the nodes in the wave function of the scatterer) increases. We set N =10⁴ to show a significant difference between the particle scattering by a Bose gas and that by a Fermi gas in a harmonic trap. The later one shifts towards the classical limit if N increases.

Here, we have considered only elastic scattering. Elementary excitations over the BEC leads to inelastic scattering involving inelastic processes where the trapped particles in scattering out-states are found in different harmonic oscillator states than those in the scattering in-states. Hence, inelastic scattering is less probabilistic at finite temperatures. Moreover, differential scattering cross-section in inelastic channels decays exponentially with the number of scatterers beyond a certain value [4].

Particle scattering by weakly interacting harmonically trapped BEC was already studied, for $T \to 0$, by Idziaszek *et al* with consideration of the first Born approximation for $g\delta^3(\mathbf{r})$ potential [4]. One may suspect their result, as, $g\delta^3(\mathbf{r})$ can not truly scatter a 'particle' except in 1-D [31, 32]. However, the first Born approximation, for $g\delta^3(\mathbf{r})$ interaction, surprisingly gives correct result for $ka_s \to 0$.

Within the last two decades, a lot of experimental observations have been done on harmonically trapped ultracold Bose and Fermi gases. Our prediction of the scattering amplitudes or differential scattering cross-sections in Eqns. (2.13) to (2.18) (or that represented in figures 3.4, 2.8 and 2.9 may open interests to the experimentalists to study temperature dependence in particle scattering by harmonically trapped Bose and Fermi gases.

Our theory can be generalized, without much difficulty, for scatterer(s) in box geometry with further consideration of scattering (diffraction) by the aperture [13], and for weakly interacting scatterers within perturbative formalism. Our work can be further extended with the consideration of the elementary excitations as prescribed in Ref.[4] specially for the condensates in a double well and optical lattice not only for elastic collisions but also for inelastic collisions. However, how to generalize our result for strongly interacting scatterers, e.g. atoms in Feshbach resonance, is an open problem. We consider condensates to be well separated in both the cases of double well and optical lattice. Generalization of results for the Josephson oscillations [42, 43] and superfluid phase specially around superfluid-Mott insulator transition [46, 17] are kept as open problems. In quantum theory, refraction can be thought of a quantum scattering of a 'particle'. In future, our theory can be extended towards the quantum theory of refractive index of a medium of quantum fluid.

Bibliography

- [1] D. J. Griffiths, *Introduction to Quantum Mechanics*, 2nd ed., Pearson Education, Singapore (2005)
- [2] E. Timmermans and R. Côté, Phys. Rev. Lett. 80, 3419 (1998)
- [3] S. Bödefeld and M. Wilkens, Quantum Semiclass. Opt.8,511,1996
- [4] Z. Idziaszek, K. Rzazewski, and M. Wilkens, J. Phys. B: At. Mol. Opt. Phys. 32, L205 (1999)
- [5] A. Wynveen, A. Setty, A. Howard, J. W. Halley, and C E Campbell, Phys. Rev. A 62, 023602 (2000)
- [6] U. V Poulsen, PhD Thesis, 2002, University of Aarhu
- [7] A. Montina, Phys. Rev. A 66, 023609 (2002)
- [8] I. Haring, PhD Thesis TU Dresden, 2003
- [9] U.V Poulsen and K Molmer Phys. Rev. A 67, 013610 (2003)
- [10] J. Brand, I. Haring, and J.M. Rost, Phys. Rev. Lett. 91, 070403 (2003)
- [11] R. A. Vicencio, J. Brand, and S. Flach, Phys. Rev. Lett. 98, 184102 (2007)
- [12] M. Streif, A.Buchleitner, D. Jaksch and J.Mur-Petit, Phys. Rev. A 94, 053634 (2016)
- [13] A. Bhattacharya and S. Biswas, Quant. Phys. Lett. 6, 5 (2007)
- [14] T. Busch, B. G. Englert, K. Rzazewski, and M. Wilkens, Foun. of Phys. 28, 549 (1998)
- [15] L. Pitaevskii and S. Stringari, Bose-Einstein Condensation, Oxford Sc. Pub. (2003)
- [16] F. Dalfovo, S. Giorgini, L. P. Pitaevskii, and S. Stringari, Rev. Mod. Phys. 71, 463 (1999)
- [17] I. Bloch, J. Dalibard, and W. Zwerger, Rev. Mod. Phys. 80, 885 (2008)
- [18] S. Giorgini, Lev P. Pitaevskii, and S. Stringari, Rev. Mod. Phys. 80, 1215 (2008)
- [19] M. Pinero, N. de la Rosa-Fox, R. Erce-Montilla, L. Esquivias, J. Sol-Gel Sci. Tech. **26**, 527 (2003)

[20] A. P. Chikkatur, A. Gorlitz, D.M. Stamper-Kurn, S. Inouye, S. Gupta, and W. Ketterle, Phys. Rev. Lett. **85**, 483 (2000)

- [21] S. L. Bromley, B. Zhu, M. Bishof, X. Zhang, T. Bothwell, J. Schachenmayer, T. L. Nicholson, R. Kaiser, S. F. Yelin, M. D. Lukin, A. M. Rey and J. Ye, Nat. Commun. 7, 11039 (2016)
- [22] H.-J. Wang, X. Yi, X. Ba, and C. Sun, Phys. Rev. A 64, 043604 (2001)
- [23] H.-J. Wang and W. Jhe, Phys. Rev. A 66, 023610 (2002)
- [24] D.Schneble, Y. Torii, M. Boyd, E. W. Streed E W, D.E Pritchard and W. Ketterle, Science 300, 475 (2003)
- [25] V. M Ezhova, L. V Gerasimov and D. V Kupriyanov, J. Phys.: Conf. Ser. 769,012045,(2016)
- [26] B. Zhu, J. Cooper, J. Ye, and A. M. Rey, Phys. Rev. A 94, 023612 (2016)
- [27] W. Kozlowski, S.F Caballero-Benitez and I.B Mekhov, Phys. Rev. A 92, 01613 (2015)
- [28] I. B Mekhov and H. Ritsch J. Phys. B: At. Mol. Opt. Phys. 45, 102001 (2015)
- [29] K. B. Davis, M.-O. Mewes, M. R. Andrews, N. J. van Druten, D. S. Durfee, D. M. Kurn, and W. Ketterle, Phys. Rev. Lett. 75, 3969 (1995)
- [30] For Born series for the δ_p^3 potential, please, see PHYS852 Quant. Mech. II, Spring 2010: HW Assignment 10.
- [31] C. N. Friedman, J. Functional Analysis **10**, 346 (1972); R. M. Cavalcanti, Rev. Bras. Ens. Fis. **21**, 336 (1999)
- [32] I. Mitra, A. DasGupta, and B. Dutta-Roy, Am. J. Phys. 66, 1101 (1998)
- [33] I. S. Gradshteyn and I. M. Ryzhik, *Table of Integrals, Series, and Products*, 7th ed., p.806, Elsevier, AM (2007)
- [34] R.P Feynman, R. B Leighton and M. L Sands,1965, *The Feynman Lectures on Physics: Quantum Mechanics*, vol 3 (Reading, MA: Addison-Wesley) ch 1
- [35] S. Biswas and D. Jana, Eur. J. Phys. 33, 1527 (2012)
- [36] S. Giorgini, L. Pitaevskii, and S. Stringari, Phys. Rev. A 54, R4633 (1996)
- [37] S. Biswas, Phys. Lett. A 372, 1574 (2008)
- [38] S. Biswas, Eur. Phys. J. D 55, 653 (2009)
- [39] J. R. Ensher, D. S. Jin, M. R. Matthews, C. E. Wieman, and E. A. Cornell, Phys. Rev. Lett. 77, 4984 (1996)

[40] M. R. Andrews, C. G. Townsend, H.-J. Miesner, D. S. Durfee, D. M. Kurn, AND W. Ketterle, Science 275, 637 (1997)

- [41] I. Bloch, T. W. Hansch, and T. Esslinger, Nature 403, 166 (2000)
- [42] S. Levy, E. Lahoud, I. Shomroni, and J. Steinhauer, Nature 449, 579 (2007)
- [43] S. Raghavan, A. Smerzi, S. Fantoni, and S. R. Shenoy, Phys. Rev. A 59, 620 (1999)
- [44] B. P. Anderson and M. A. Kasevich, Science 282, 1686 (1998)
- [45] P. Pedri, L. Pitaevskii, S. Stringari, C. Fort, S. Burger, F. S. Cataliotti, P. Maddaloni, F. Minardi, and M. Inguscio, Phys. Rev. Lett. 87, 220401 (2001)
- [46] M. Greiner, M. O. Mandel, T. Esslinger, T. Hansch, and I. Bloch, Nature 415, 39 (2002)

Chapter 3

Particle scattering by rotating trapped quantum gases at finite temperatures

3.1 Introduction

There have been many experimental observations of the collective properties of rotating harmonically trapped ultracold Bose [1, 2, 3, 4] and Fermi [5] gases in their respective condensate or superfluid state since 1999 [6, 7]. Interestingly, an electrically neutral particle in a rotating trapped condensate/superfluid resembles a positively charged particle exposed to a constant magnetic field, say along the z-axis, if the angular trap-frequency (ω_{\perp}) of oscillation in the x-y plane approaches the angular speed of the rotation (Ω) about the z-axis [8, 6]. Consequently, a number of interesting aspects of Landau level physics [9, 10], have been observed in the rotating trapped quantum gases of electrically neutral bosons/fermions. The resemblance has been further achieved for quantum gases in artificial magnetic/gauge fields [11, 12]. All this experimental evidence has motivated immense theoretical progress in the field [13, 14, 15, 16, 17, 18, 19, 20].

Surprisingly, the de Haas-van Alphen effect [21] which belongs to the Landau level physics [22], has not been observed so far in the rotating trapped quantum gas of the neutral fermions, though the effect was theoretically proposed for both the rotating trap and the artificial gauge field [23, 24]. Here, we are proposing how an alternative method, say particle scattering, can be taken up for observing the de Haas-van Alphen effect in the rotating trap. Particle scattering by the rotating trapped quantum gas has not been studied so far, though a number of experimental [25] and theoretical [26, 27, 28, 29, 30, 31, 32, 33, 34] works have been reported for the same in non-rotating traps. Hence, we take up the challenge of studying the particle scattering by the rotating harmonically trapped quantum gases from a theoretical point of view. The particle scattering would be an important tool for probing the collective properties of the rotating trapped Bose and Fermi gases of electrically neutral particles, in particular, the Bose-Einstein condensation [16], vortices in the

3.1. Introduction 69

rapidly rotating Bose-Einstein condensate [1, 15], and the de Haas-van Alphen effect [23, 24].

Our theoretical study essentially takes up the discussion on particle scattering to introduce quantum scattering by the Bose or Fermi gas of electrically neutral scatterers in thermal equilibrium for the Fermi-Huang $g\delta_p^3$ [35] interactions (among the incident 'particle' and the scatterers) in the quantized levels of the rotating harmonic trap. Here, the Fermi-Huang interactions act as a probe potential which although is easy to deal with, has huge applications in the field of ultra-cold atoms [36, 6, 37, 38]. We are especially interested in the temperature dependence of differential scattering cross-section for the rotating trapped Bose or Fermi gas in this regard because thermodynamic properties of ultra-cold gases in rotating traps are of growing interest [39, 16, 40].

It is well known that a spherical wave $(\psi_{out} \equiv \frac{e^{ikr}}{r})$ goes out of the scatter with a scattering amplitude $(f(\theta,\phi))$ to a particular direction (θ,ϕ) with respect to the initial direction of incidence $(\hat{k}=\hat{z})$ if a plane wave $(\psi_{in}\equiv e^{ikz})$ associated with a free particle ('particle') of a given momentum $(\mathbf{p}=\hbar k\hat{k})$ is scattered by a fixed scatterer (at $\mathbf{r}=\mathbf{0}$) [41]. If the scatterer is not fixed, say, the scatterer is a particle in a 3-D simple harmonic trap which is rotating at a constant angular velocity $\Omega\hat{k}$, then according to the superposition principle, the 'particle' would be scattered coherently from all the positions of the scatterer with the respective probability density. This brings the quantum state of the scatterer into the description of the net scattering amplitude. We further have to consider scattering by many-particle scatterers of bosonic or fermionic type at a finite temperature. We must mention in

this regard that we have already explored temperature dependence of the differential scattering cross-section for the particle scattering by the same systems without considering the rotation [34]. However, particle scattering by rotating quantum gases has not been studied so far, and the study of the same would be useful for probing orbital/artificial magnetism of the electrically neutral bosons and fermions.

This article begins with a brief description of the quantum theory of particle scattering by a quantum scatterer in the rotating 3-D harmonic trap for the Fermi-Huang potential (i.e. regularized δ^3 potential: $V_{int}(\mathbf{r}) = g \delta_p^3(\mathbf{r}) = g \delta^3(\mathbf{r}) \frac{\partial}{\partial r} r$ [34]). Then we generalize the theory for quantum gas of scatterers. Then we obtain differential scat-

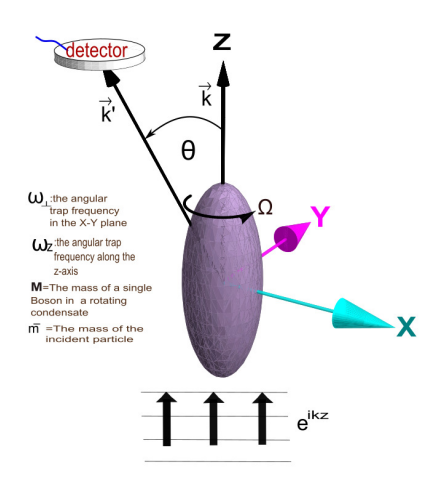


FIGURE 3.1: A schematic diagram for particle scattering by a rotating harmonically trapped BEC.

tering cross-sections and their temperature and angular speed dependencies for both the slow rotation and the fast rotation of the trapped systems. Then we generalize

¹Here, by 'particle' we mean- the wave associated with the incident particle.

our theoretical results for the weakly interacting rotating Bose gases in the harmonic traps. We also discuss the finite-size effect especially on the interacting rotating Bose system in this regard. Then we theoretically probe the lattice-pattern of the vortices in a rapidly rotating weakly interacting Bose-Einstein condensate by the particle scattering method. We also obtain de Haas-van Alphen-like oscillation in the differential scattering cross-section of the ultracold ideal Fermi gas in the rotating trap. Finally, we conclude.

3.2 Particle scattering by a single scatterer in a rotating harmonic trap

Let us consider the rotation of a 3-D harmonically trapped scatterer by a constant angular velocity $\vec{\Omega} = \Omega \hat{k}$ along the z-axis. If we consider a frame, having the same origin as with the lab-fixed frame, same z-axis and rotating with the same angular velocity $\vec{\Omega} = \Omega \hat{k}$ with respect to the lab-fixed frame, then the time-independent Schrödinger equation for the wavefunction $\psi_s'(\mathbf{r}')$

for the particle scattering in the rotating frame would be recast, as [16, 39]

$$\left(-\frac{\hbar^2}{2\bar{m}}\nabla'^2 - \vec{\Omega}\cdot\hat{\mathbf{L}}' + V_{int}(\mathbf{r}')\right)\psi_s'(\mathbf{r}') = E'\psi_s'(\mathbf{r}')(3.1)$$

where not only \mathbf{r}' represents the position vector of the particle but also all other primed quantities including the angular momentum operator $\hat{\mathbf{L}}'$ and energy E' represent respective quantities with respect to the rotating frame. From now onward, we will be considering only the rotating frame for our analyses by replacing the primed quantities by unprimed quantities such as $\psi_s' \to \psi_s$, $f' \to f$, $\mathbf{r}' \to \mathbf{r}$, $E' \to E$, $\hat{\mathbf{L}}' \to \hat{\mathbf{L}}$, $\theta' \to \theta$, $\phi' \to \phi$, etc. Thus, we get solution to Eqn. (3.1) in the radiation zone ($kr \gg 1$), as

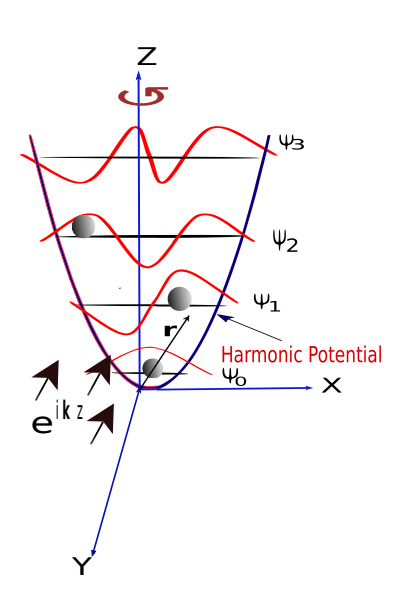


FIGURE 3.2: Rotating harmonic oscillatar quontum gas

$$\psi_s(\mathbf{r}) = \psi_s(r, \theta, \phi) \simeq \bar{A} \left[e^{ikz} + f(\theta, \phi) \frac{e^{ikr}}{r} \right] e^{i\frac{\phi Lz}{\hbar}}$$
 (3.2)

where L_z is the z-component of the angular momentum of the scatterer with respect to the rotating frame. Since the phase part $\frac{\phi L_z}{\hbar}$ is common to both the incident plane wave and the outgoing spherical wave in Eqn. (3.2), as the Fermi-Huang potential is spherically symmetric, the form of the scattering amplitude remains unaltered with its form in the non-rotating frame.

The Fermi-Huang δ_p^3 interaction between the incident particle at **r** and the scatterer at $\mathbf{r}_0 = x_0\hat{i} + y_0\hat{j} + z_0\hat{k}$ can be expressed, as

$$V_{int}(\mathbf{r}) = g\delta_n^3(\mathbf{r} - \mathbf{r}_0). \tag{3.3}$$

The scattering amplitude with respect to the rotating frame takes the form for the pseudo-potential as in Eqn.(3.3), as [34]

$$f(\theta,\phi) = -\frac{\bar{m}g_k}{2\pi\hbar^2} e^{-i[\mathbf{k}'\cdot\mathbf{r}_{\perp_0} + (\mathbf{k}'-\mathbf{k})\cdot\hat{k}z_0]}$$
(3.4)

where $\mathbf{r}_{\perp_0} = x_0\hat{i} + y_0\hat{j}$ is the position vector for the scatterer in the x-y plane, $(\mathbf{k}'-\mathbf{k})\cdot\hat{k} = k[\cos(\theta)-1] = -2k\sin^2(\theta/2)$ is the momentum-transfer in units of \hbar along the z-axis in the process of the elastic scattering $(|\mathbf{k}'| = |\mathbf{k}| = k)$, $g_k = \frac{g}{1+ika_s\bar{m}/\bar{\mu}}$, $\bar{\mu} = \frac{\bar{m}M}{\bar{m}+M}$ is the reduced mass of the incident particle and the scatterer, and $a_s = -(\bar{\mu}/\bar{m})\lim_{k\to 0} f(\theta,\phi) = \frac{\bar{\mu}g}{2\pi\hbar^2}$ is the s-wave scattering length for the scattering [34]. Here, the wave-vector \mathbf{k}' makes an angle θ with the z-axis, the projection of \mathbf{k}' makes an angle $\phi + \phi_0$ with the x-axis once it rotates ϕ_0 with respect to the z-axis, and consequently, the projection of \mathbf{k}' makes an angle $\pi/2 - (\phi + \phi_0)$ with the y-axis.

Let us now consider the quantized motion of the scatterer into the theory of quantum scattering [42, 26, 34] by the scatterer in the 3-D rotating harmonic trap. Let the scatterer be vibrating simple harmonically along the z-axis with the angular frequency ω_z in addition to the uniform rotation with the angular velocity $\Omega \hat{k}$ about the same axis and the simple harmonic motion in the x-y plane with the angular frequency $\omega_x = \omega_y = \omega_\perp$. The normalized energy eigenstate of the scatterer, in this case, is given in terms of the cylindrical polar coordinates within the symmetric gauge (for the artificial vector potential $\mathbf{A} = -\frac{1}{2}\mathbf{r} \times B\hat{k} = -\frac{1}{2}\mathbf{r} \times \frac{2M\Omega}{q'}\hat{k}$; q'=1) [39]) by [43, 44]

$$\psi_{n,m,j}(\mathbf{r}_{0}) = \sqrt{\frac{1}{2\pi} \frac{2}{l_{\perp}^{2}} \frac{(n - [|m| + m]/2)!}{(n + [|m| - m]/2)!}} e^{-im\phi_{0}}$$

$$\times \left(\frac{r_{\perp_{0}}^{2}}{l_{\perp}^{2}}\right)^{\frac{|m|}{2}} e^{-\frac{r_{\perp_{0}}^{2}}{2l_{\perp}^{2}}} L_{n - \frac{|m| + m}{2}}^{|m|} \left(\frac{r_{\perp_{0}}^{2}}{l_{\perp}^{2}}\right)$$

$$\times \sqrt{\frac{1}{\sqrt{\pi} l_{z}}} \frac{1}{\sqrt{2^{j} j!}} H_{j}(z_{0}/l_{z}) e^{-z_{0}^{2}/2l_{z}^{2}}$$
(3.5)

where $\mathbf{r}_0 \equiv (r_{\perp_0},\phi_0,z_0)$ represents the position of the scatterer in the cylindrical coordinate system of the rotating frame, H_j represents the Hermite polynomial of degree $j=0,1,2,...,\infty$ [41], $l_z=\sqrt{\hbar/M\omega_z}$ is the confining length scale of the scatterer along the z-axis, $L_{n-\frac{m+|m|}{2}}^{|m|}$ represents the associated Laguerre polynomial in the usual notation [43, 44], $n=0,1,2,...,\infty$ represents the Landau level when $\omega_\perp=\Omega$, $m=n,n-1,n-2,...,-\infty$ represents the magnetic quantum number for a given $n,l_\perp=\sqrt{\hbar/M\omega_\perp}$ is the confining length scale of the scatterer in the x-y plane.

Energy eigenvalue of the scatterer corresponding to the state $\psi_{n,m,j}(\mathbf{r}_0)$ would be [44, 39]

$$\epsilon_{n,m,j} = (n+1/2)\hbar(\omega_{\perp} + \Omega) + (n-m+1/2)\hbar(\omega_{\perp} - \Omega) + (j+1/2)\hbar\omega_{z}$$
(3.6)

Radial distance (r_{\perp_0} in the x_0-y_0 plane) and azimuthal angle (ϕ_0) parts of the state $\psi_{n,m,j}(\mathbf{r}_0)$ are together called as the Fock-Darwin state [45, 44] which becomes Landau state [46] of infinite degeneracy for $\omega_{\perp}=\Omega$. The symmetric axis (z_0) part of the state, on the other hand, is called as the simple harmonic oscillator state [41]. It is clear from the energy eigenvalues that the Fock-Darwin states are unstable for $\omega_{\perp}-\Omega<0$. Hence, we restrict the angular speed to be $\Omega\leq\omega_{\perp}$ for our entire analysis.

Let us now consider the quantum scattering of the incident 'particle' $(\bar{A}e^{ikz})$ by the scatterer as described in Eqn. (3.5) for the rotating harmonically trapped system. Now, the particle scattering is taking place from all possible positions $\{\mathbf{r}_0\}$ of the scatterer (i.e. for $0 < r_{\perp_0} < \infty$, $0 \le \phi_0 < 2\pi$ and $-\infty < z_0 < \infty$) simultaneously with respective probability densities $\{|\psi_{n,m,j}(\mathbf{r}_0)|^2\}$ for a given energy eigenstate $(|\psi_{n,m,j}\rangle)$. Thus the net scattering amplitude for the scatterer in the quantum state $|\psi_{n,m,j}\rangle$ can be written by applying the superposition principle on the Eqn. (3.4) for the energy eigenstate $\psi_{n,m,j}(\mathbf{r}_0)$ of the Eqn. (3.5), as [47]

$$f_{n,m,j}(\theta,\phi) = -\frac{\bar{m}g_{k}}{2\pi\hbar^{2}} \int_{\phi_{0}=0}^{2\pi} \int_{r_{\perp_{0}}=0}^{\infty} \int_{z_{0}=-\infty}^{\infty} dr_{\perp_{0}} d\phi_{0} dz_{0}$$

$$r_{\perp_{0}} |\psi_{n,m,j}(\mathbf{r}_{0})|^{2} e^{-i[\mathbf{k}' \cdot \mathbf{r}_{\perp_{0}} + (\mathbf{k} - \mathbf{k}') \cdot \hat{k}z_{0}]}$$

$$= a_{k} e^{-\bar{q}_{z}^{2} l_{z}^{2}} L_{j} (2\bar{q}_{z}^{2} l_{z}^{2})$$

$$\times e^{-2q_{\perp}^{2} l_{\perp}^{2}} L_{n} (q_{\perp}^{2} l_{\perp}^{2}) L_{n-m} (q_{\perp}^{2} l_{\perp}^{2})$$
(3.7)

where $a_k = -\frac{\bar{m}g_k}{2\pi\hbar^2} = -\frac{a_s\bar{m}/\bar{\mu}}{1+ika_s\bar{m}/\bar{\mu}}$, $q_\perp = k\sin(\theta)/2$, $\bar{q}_z = k[1-\cos(\theta)]/2$, and $L_j(2\bar{q}_z^2l_z^2)$ [34] is the Laguerre polynomial of degree j. The right-hand side of Eqn. (3.7) by the definition appears as the Fourier transform of the probability density of the energy eigenstate $\psi_{n,m,j}(\mathbf{r}_0)$. The net scattering amplitude $f_{n,m,j}(\theta,\phi)$ can be called as the form factor for the quantum state of the scatterer $|\psi_{n,m,j}\rangle$ [48, 47]. It is clear from Eqn. (3.7) that the scattering amplitude $f_{n,m,j}(\theta,\phi)$ is independent of the azimuthal angle (ϕ) because of the radial symmetry of the Fermi-Huang interaction potential and the rotational symmetry of the probability density $(|\psi_{n,m,j}(\mathbf{r}_0)|^2)$ of the scatterer about the z-axis. However, the translation symmetry along the z-axis is broken because of the harmonic potential $\frac{1}{2}M\omega_z^2z_0^2$.

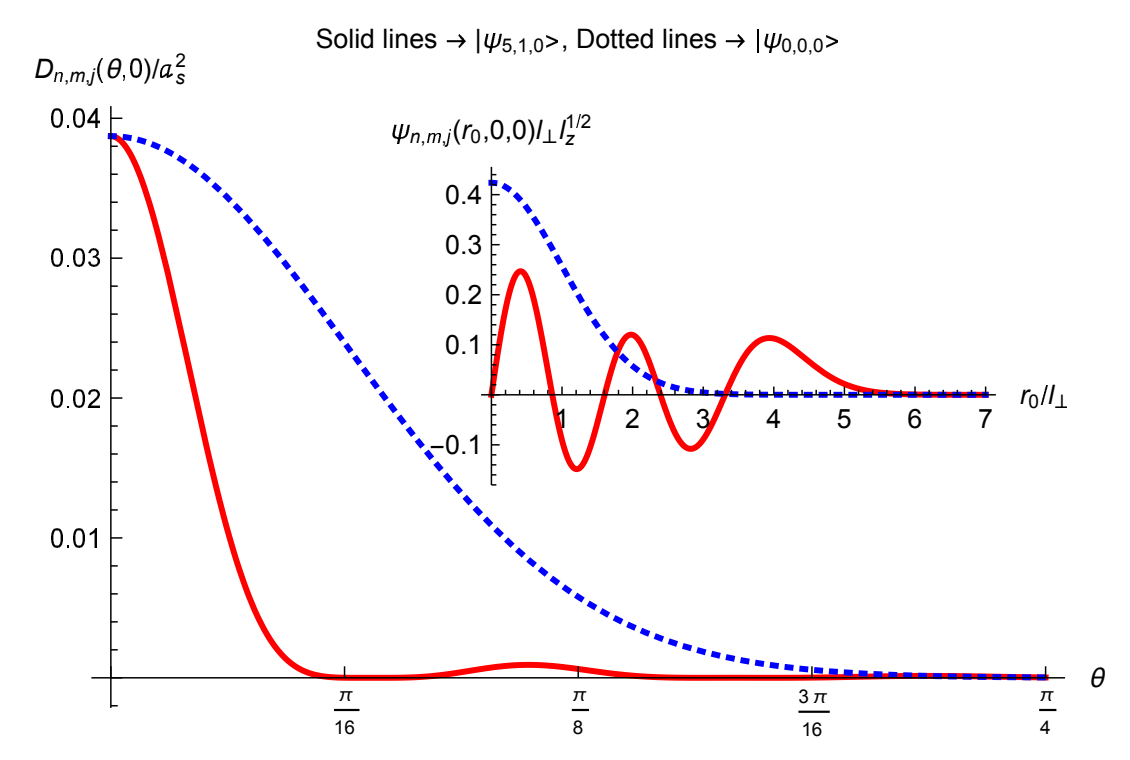


FIGURE 3.3: Net differential scattering cross-section $(D_{n,m,j}(\theta,0))$ for the scattering of a 'particle' $(\bar{A}\mathrm{e}^{ikz})$ by the 3-D rotating harmonic oscillator for a_s as unit length, $\Omega \to \omega_\perp$, $ka_s = 5$, $l_\perp/a_s = 1$, $l_z/a_s = 1$ and $\bar{m}/M = 0.1$. Both the solid line and the dotted line follow Eqn. (3.8) for the bound states $|\psi_{5,1,0}\rangle$ and $|\psi_{0,0,0}\rangle$, respectively. Both the solid line $(|\psi_{5,1,0}\rangle)$ and the dotted line $(|\psi_{0,0,0}\rangle)$ in the inset represent plots of these bound states with respect to the radial coordinate and follow Eqn. (3.5).

The net differential scattering cross-section for the scatterer in the rotating harmonic trap can be obtained from Eqn. (3.7), as

$$D_{n,m,j}(\theta,\phi) = |f_{n,m,j}(\theta,\phi)|^2 = |a_k e^{-\bar{q}_z^2 l_z^2} L_j (2\bar{q}_z^2 l_z^2) \times e^{-q_\perp^2 l_\perp^2} L_n (q_\perp^2 l_\perp^2) L_{n-m} (q_\perp^2 l_\perp^2)|^2.$$
(3.8)

It is to be noted that this result though is independent² of the angular speed (Ω) , it is not the same as that obtained for the scatterer in a 3-D non-rotating anisotropic harmonic trap where there is a ϕ -dependence [34]. If we average over ϕ with the same axial symmetry of vibration ($\omega_x = \omega_y = \omega_\perp$) for the non-rotating case [34], then only we get the same result as we have in Eqn. (3.8). We plot the right-hand side of Eqn. (3.8) in figure 3.3 for two bound states $|\psi_{5,1,0}\rangle$ (solid line) and $|\psi_{0,0,0}\rangle$ (dotted line) of the scatterer. We also plot the bound states in the inset of figure 3.3. While the number of nodes of the bound state wavefunction $\psi_{n,m,j}(r_{\perp_0},\phi_0,z_0)$ is n-[m+|m|]/2 on the radial axis (r_0) , the same on the z_0 axis is j. The 'particle' $(\bar{A}e^{ikz})$ interferes with itself while being scattered from different internodal regions of the scatterer. This causes appearance of 2n - m + j zeros³ on the θ -axis of the net differential scattering cross-section $(D_{n,m,j}(\theta,\phi))$. State of the scatterer can not, however, be fully probed in terms of the zeros of the net differential scattering cross-section by any value of the wavevector (k) of the 'particle'. It needs a large value of the wavevector to probe all the nodes of the bound state of the scatterer. We consider two special cases of the same in figure 3.3. All the zeros of $D_{5,1,0}(\theta,0)$ are not apparent in figure 3.3 for the value of k chosen for it. Parameters taken for plotting this figure, however, are not specific to a particular scattering problem. We set $\bar{m}/M = 0.1$ which would be appropriate for ⁴⁰K atom as a fermionic scatterer and ⁴He as the scattered particle or the projectile. The ratio of \bar{m}/M though would be even less (0.046) for the combination of ⁸⁷Rb atom (bosonic scatterer) and ⁴He (scattered particle), our result would not change much, as $\bar{m}/\bar{\mu}$ for both the cases are approximately 0.91 and 0.96, respectively [34].

Here we have considered the energy eigenstate $|\psi_{n,m,j}\rangle$ to be unaltered in the process of scattering. The energy eigenstate would be altered in the process of inelastic scattering [42]. We will discuss the inelastic scattering in the concluding section for justifying its low probability in the context of thermal and many-body effects [26]. However, role of the angular speed (Ω) is not absolutely redundant, and would be important for determining the net differential scattering cross-section at a temperature T for the scatterer in equilibrium with a thermal bath because the statistical probability of the state $\psi_{n,m,j}(\mathbf{r}_0)$ depends on the energy eigenvalue $\epsilon_{n,m,j}$. Role of the angular speed would also be important in determining the degeneracy of the

²The independence follows from the rotational symmetry of the system along the *z*-axis.

³Number of the zeros follows from Eqn. (3.8).

Landau level for $\Omega \to \omega_{\perp}$. A large value of the wavenumber, however, is not necessarily needed to probe the collective properties of a system of scatterers. The collective property, of course, needs each scattering effect, like the one in figure 3.3, to be taken into account. Our main focus on the article would be on probing the collective properties of systems of scatterers at finite temperatures by the particle scattering method.

The incident particles can be treated as impurity atoms which can propagate at different velocities through the gas of scatterers (atoms/molecules) [25]. The impurity atoms can be produced using a stimulated Raman transition [25]. The Fermi-Huang delta potential can be realized for a low wavenumber of the incident 'particle' so that the de Broglie wavelength of the incident 'particle' can be larger than the linear dimension of the scatterer. The incident particle can not feel the actual potential of the scatterer in such a case. Fermi-Huang delta potential, however, would be a good model potential for a low energy scattering involving only the *s*-wave scattering length [37]. Low energy scattering also makes the recoil effects on the gas (or modifications on the internal structure of the atoms) irrelevant. If the scattered particles are indistinguishable from the scatterers, then the statistics of the scattered particles should be taken into consideration. We are not considering such a case in our analysis.

3.3 Particle scattering by Bose and Fermi gases in rotating harmonic traps

Let us now consider an ideal gas of identical bosonic or fermionic scatterers in the rotating 3-D harmonic trap [39, 6, 16] as described in the previous section. Let \mathbf{r}_{0_i} be the position of the ith scatterer. The scatterer, in this case, scatters the incident 'particle' by the Fermi-Huang delta potential $V_{int}(\mathbf{r}) = g \delta_p^3(\mathbf{r} - \mathbf{r}_{0_i})$. Let us further consider the ideal gas of scatterers to be in the thermodynamic equilibrium with its surroundings at a temperature T and a chemical potential μ . The net differential scattering cross-section for the particle scattering by the many-body system can be obtained from Eqn. (3.8) within the superposition principle with the proper statistical weight of each of the Fock-Darwin states, as

$$\bar{D}_{T}(\theta,\phi) = |a_{k}|^{2} e^{-2[q_{\perp}^{2}l_{\perp}^{2} + \bar{q}_{z}^{2}l_{z}^{2}]} \times \left[\sum_{n=0,m'=0,j=0}^{\infty} \frac{L_{n}(q_{\perp}^{2}l_{\perp}^{2})L_{m'}(q_{\perp}^{2}l_{\perp}^{2})L_{j}(2\bar{q}_{z}^{2}l_{z}^{2})}{e^{(\epsilon_{n,n-m',j}-\mu)/k_{B}T} \mp 1} \right]^{2}$$
(3.9)

where m' is defined as m' = n - m and the factor $\frac{1}{e^{(\epsilon_{n,n-m',j}-\mu)/k_BT}}$ represents the statistical weight i.e. the average number of Bose (upper sign) or Fermi (lower sign) scatterers $(\bar{n}_{n,m,j})$ in the single-particle state $\psi_{n,m,j}(\mathbf{r}_0)$ [37]. The above three summations can be evaluated by expanding the Bose/Fermi factor about

 $e^{[\mu-(\hbar\omega_++\hbar\omega_-+\hbar\omega_z)/2]/k_BT}=0$ and using the generating function formula for the Laguerre polynomials $\sum_{n=0}^{\infty}e^{-n/b}L_n(x)=rac{e^{rac{1}{b}+rac{x}{1-e^{rac{1}{b}}}}}{-1+e^{rac{1}{b}}}$, as

$$\bar{D}_{T}(\theta,\phi) = |Na_{k}|^{2} e^{-2[q_{\perp}^{2}l_{\perp}^{2} + \bar{q}_{z}^{2}l_{z}^{2}]} \times \left[\frac{-\frac{q_{\perp}^{2}l_{\perp}^{2}}{s\hbar\omega_{+}} - \frac{q_{\perp}^{2}l_{\perp}^{2}}{s\hbar\omega_{+}} - \frac{-\frac{q_{\perp}^{2}l_{\perp}^{2}}{s\hbar\omega_{-}}}{\frac{s\hbar\omega_{-}}{1 - e^{-\frac{s\hbar\omega_{+}}{k_{B}T}}} - \frac{e^{\frac{2\bar{q}_{z}^{2}l_{z}^{2}}{s\hbar\omega_{z}}}}{1 - e^{-\frac{s\hbar\omega_{z}}{k_{B}T}}} \frac{e^{\frac{2\bar{q}_{z}^{2}l_{z}^{2}}{1 - e^{-\frac{s\hbar\omega_{z}}{k_{B}T}}}}}{1 - e^{-\frac{s\hbar\omega_{+}}{k_{B}T}}} \frac{1}{1 - e^{-\frac{s\hbar\omega_{+}}{k_{B}T}}} \frac{1}{1 - e^{-\frac{s\hbar\omega_{z}}{k_{B}T}}} \frac{(\pm 1)^{s+1}\bar{z}^{s}}{1}}{1 - e^{-\frac{s\hbar\omega_{+}}{k_{B}T}}} \frac{1}{1 - e^{-\frac{s\hbar\omega_{+}}{k_{B}T}}} \frac{1}{1 - e^{-\frac{s\hbar\omega_{z}}{k_{B}T}}} \frac{(\pm 1)^{s+1}\bar{z}^{s}}{1}}{1} \right]$$
(3.10)

where $\omega_+ = \omega_\perp + \Omega$, $\omega_- = \omega_\perp - \Omega$ and $\bar{z} = \mathrm{e}^{[\mu - (\hbar\omega_+ + \hbar\omega_- + \hbar\omega_z)/2]/k_BT}$ is the fugacity of the system of the scatterers, and N is the total average number of scatterers in the system. The fugacity can be determined from the normalization of the net differential scattering cross-section for the forward scattering, $\bar{D}_T(0,\phi) = |Na_k|^2$, so that the average number of scatterers takes the form

$$N = \sum_{s=1}^{\infty} \frac{1}{1 - e^{-\frac{s\hbar\omega_{+}}{k_{B}T}}} \frac{1}{1 - e^{-\frac{s\hbar\omega_{-}}{k_{B}T}}} \frac{1}{1 - e^{-\frac{s\hbar\omega_{-}}{k_{B}T}}} \frac{(\pm)^{s+1}\bar{z}^{s}}{1}.$$
 (3.11)

This form of N can also be resulted from summing the average occupation numbers $\{\bar{n}_{n,m,j}\}$ in the single-particle states over the quantum numbers n,m', and j. Eqn. (3.10) can be directly used to get the temperature dependence of the net differential scattering cross-section once we know temperature dependence of the fugacity. The fugacity in Eqn. (3.10) can be determined from Eqn. (3.11) in the thermodynamic limit $(N \to \infty, \omega_+, \omega_-, \omega_z \to 0, N\omega_+\omega_-\omega_z = constant)$ for the given number of scatterers N and the given temperature T by following the method as described in Ref.[49]. While the fugacity of the rotating trapped Bose gas below the condensation point $(T_c = \frac{\hbar[\omega_+\omega_-\omega_z]^{1/3}}{k_B} (\frac{N}{\zeta(3)})^{1/3})$ is 1 and is $\bar{z} \simeq \mathrm{e}^{-\frac{3\zeta(3)T_c}{\zeta(2)T}[T/T_c-1]}$ just above the condensation point, it is $\bar{z} \simeq \mathrm{e}^{\frac{T_c}{T}[1-(\pi^3/3)(T/T_F)^2]}$ well below the Fermi temperature $T_F = \frac{\hbar[\omega_+\omega_-\omega_z]^{1/3}}{k_B} (6N)^{1/3}$ for the rotating Fermi gas [49].

We plot Eqn. (3.10) by applying the above temperature dependence of the fugacity with the proper care for the condensation fraction to show the temperature dependence of the net differential scattering cross-section for the rotating 3-D harmonically trapped ideal Bose gas for $\Omega=\omega_{\perp}/3$ and to compare the same with the one obtained for the non-rotating case in figure 3.4. The parameters $N=3\times 10^5$ and $\omega_{\perp}/10=\omega_z=20\pi$ Hz used for plotting this figure are taken from the experimental data for rotating trapped Bose-Einstein condensate [39]. It is clear from figure 3.4 that the differential scattering cross-section decreases as the temperature increases. This is possible because the coherence in the particle scattering gets reduced if the scatterers are found in different energy eigenstates other than the ground state at a finite temperature [34].

The net differential scattering cross-section (Eqn. (3.10)) for the slow rotating system (0 < $\Omega \lesssim \Omega_c$) ⁴ looks similar to that of the non-rotating system [34] with the substantial change of the condensation point for bosons as long as no transfer of angular momentum to the gas of the scatterers is concerned [39].

We have discussed the case of the slow rotation for ideal rotating trapped Bose gas of scatterers. However, the net differential scattering cross-section would be quite different for the fast rotation ($\Omega_c \lesssim \Omega \lesssim \omega_\perp$) especially for $\Omega \to \omega_\perp$ of the ideal trapped Bose gas. The Fock-Darwin states, as described in Eqn. (3.5), become the Landau states which have infinity large degeneracy each for the case of the ultrafast rotation $\Omega = \omega_\perp$. In this situation ω_+ becomes the (angular) cyclotron frequency ($\omega_c = 2\Omega$), ω_- goes to zero, and the cross-sectional area (A') in the x-y plane of the system of scatterers goes to infinity in the thermodynamic limit such that $\omega_z N/A' = constant$. Since the thermodynamic properties of a system do not depend on the choice of the gauge, degeneracy of the Landau level would be same as that $(\frac{q'A'B}{2\pi\hbar} = \frac{M\omega_c A'}{2\pi\hbar}$ [22, 50]) in the Landau gauge. Thus the magnetic quantum number m, though varies from n to $-\infty$, can be taken from n (with unit interval) to $-(s_n-1) = -\lfloor (\frac{M\omega_c A'}{2\pi\hbar} - n) \rfloor$ in the thermodynamic limit. Thus each of the Landau level has $s_0 = \lceil \frac{M\omega_c A'}{2\pi\hbar} \rceil$ degeneracy. The net differential scattering cross-section for the particle scattering can be obtained from Eqn. (3.9), for $\Omega = \omega_\perp$, as

$$\bar{D}_{T}(\theta,\phi) = \left| a_{k} L_{s_{0}-1}^{1} (q_{\perp}^{2} l_{\perp}^{2}) \right|^{2} \times \left[\sum_{n,j} \frac{e^{-2[q_{\perp}^{2} l_{\perp}^{2} + \bar{q}_{z}^{2} l_{z}^{2}]} L_{n}(q_{\perp}^{2} l_{\perp}^{2}) L_{j}(2\bar{q}_{z}^{2} l_{z}^{2})}{e^{\frac{(n+1/2)\hbar\omega_{c} + (j+1/2)\hbar\omega_{z} - \mu}{k_{B}T} \mp 1} \right]^{2}.$$
(3.12)

It is clear from Eqn. (3.12) that infinitely large amount of degeneracy $(s_0 = \lceil \frac{M\omega_c A'}{2\pi\hbar} \rceil)$ of each Landau level washes out the coherence in the net scattering even for $T \to 0$. A quantum phase transition, however, takes place due to quantum fluctuations in the strongly interacting Bose gas once the condensate is destroyed for $\Omega = \omega_{\perp}$ [51, 52].

3.3.1 The case of inter-scatterer interactions for the Bose gas at a finite temperature

We have discussed the case of the rotating trapped ideal Bose gas of scatterers at a finite temperature. Let us now discuss the weak inter-scatterer interactions effect along with the finite temperature effect for the particle scattering by interacting Bose scatterers in the 3-D rotating harmonic trap. We are considering the weak inter-scatterer interactions in the form of the interacting potential energy $U = \frac{4\pi\hbar^2 \tilde{a}_s}{M} \sum_{i,j < i} \delta_p^3 (\mathbf{r}_{0i} - \mathbf{r}_{0j})$ where \tilde{a}_s is the s-wave scattering length for the inter-scatterer collisions.

⁴Here Ω_c is the critical value of Ω for single vortex nucleation in the system of scatterers. Experimentally value of Ω_c for rotating trapped Bose-Einstein condensate is $\Omega_c \simeq 0.7\omega_{\perp}$ [2, 16].

⁵Here we have used the relation $\sum_{n=0}^{j} L_n(x) = L_j^1(x)$.

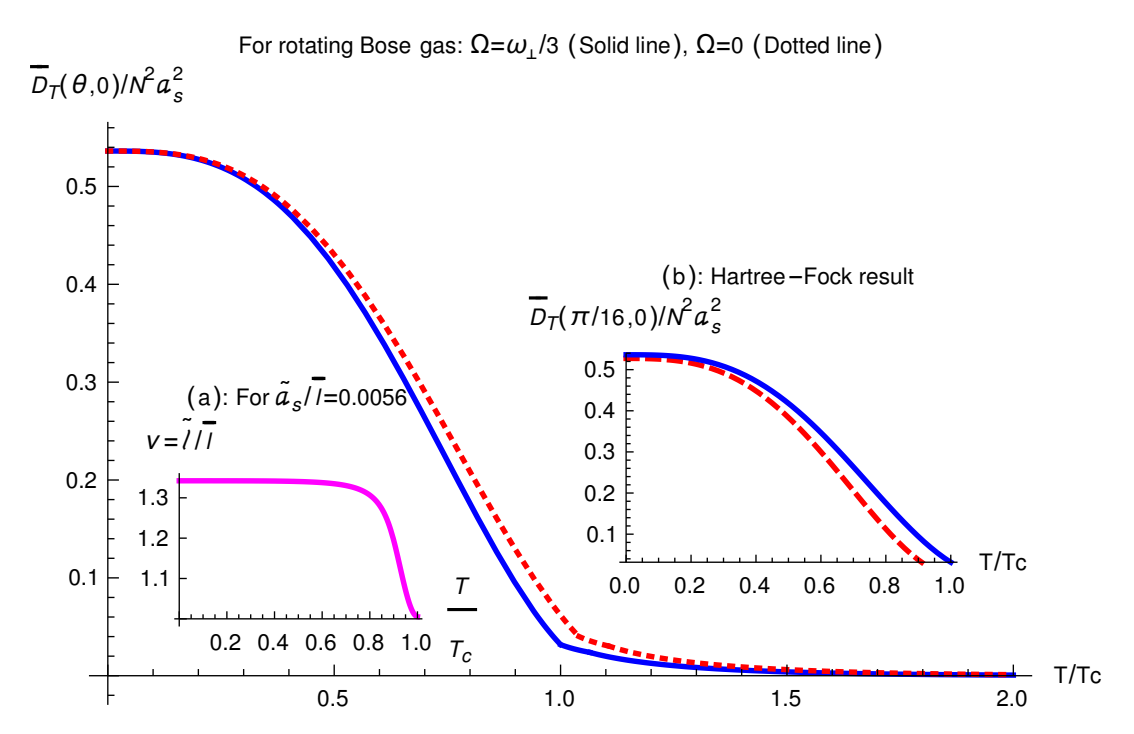


FIGURE 3.4: Temperature dependence of the net differential scattering cross-section for the rotating 3-D harmonically trapped ideal Bose gas for $\theta=\pi/16$, $\bar{m}/M=0.1$, $ka_s=1$, $l_\perp=a_s$, $\omega_\perp/10=\omega_z=20\pi$ Hz, and $N=3\times 10^5$. Both the plots follow from Eqn. (3.10) with proper care of the condensation fraction for $\Omega=\omega_\perp/3$ (solid line) and $\Omega=0$ (dotted line). The plot in the inset-a represents finite temperature scaling $(\bar{l}\to\tilde{\ell}=\nu\bar{l})$ of \bar{l} for the rotating trapped system for $\tilde{a}_s=90a_0=0.0056\bar{l}$ [54] and $N=3\times 10^5$ [39] for the ⁸⁷Rb atom scatterers. The dashed line in the inset-b represents finite-size and inter-scatterer effects on the rotating system within the H-F approximation over the solid line which represents the ideal case ($\tilde{a}_s=0$) for the same set of parameters except \tilde{a}_s .

The case of slow rotation

Temperature dependence of the net differential scattering cross-section for the Bose gas in the 3-D rotating trap ($\Omega < \omega_\perp$) comes from the Eqn. (3.10). The effective length scale of the slow rotating Bose system for $T \to 0$ is given by $\bar{l} = \sqrt{\hbar/M\bar{\omega}}$. It has been shown in Ref. [34] for the non-rotating trapped Bose scatterers that the inter-scatterer interactions do not greatly modify the temperature dependence of the net differential scattering cross-section as long as the weak inter-scatterer interactions ($N^{1/6}\tilde{a}_s/\bar{l}\ll 1$) are concerned. The weak inter-scatterer interactions, apart from substantially modifying the condensate fraction, can substantially change the temperature dependence for the slow rotating ($\Omega \lesssim \Omega_c$) Bose gas. Thus Eqn. (3.10) would be primarily unaltered due to the weak interaction effect except for the scaling of the lengths l_\perp and l_z to $\ell_\perp = \nu l_\perp$ and $\ell_z = \nu l_z$ ($\nu > 1$ for repulsive interactions), respectively. The scaling parameter is the same for both the length scales (l_\perp and l_z) because the inter-scatterer interactions are isotropic. Further substantial change of the condensation point arises due to the finite-size effect [55, 56].

The condensate fraction of a non-rotating Bose gas, for the finite-size of the trap and weak inter-scatterer interactions $(\frac{4\pi\hbar^2\tilde{a}_s}{M}\sum_{i,j< i}\delta_p^3(\mathbf{r}_{0i}-\mathbf{r}_{0j}))$, takes the form $\frac{N_0}{N}=$ $1 - (T/T_c)^3 - \frac{3T^2\zeta(2)}{2T_c^2\zeta(3)} \frac{[2\omega_{\perp} + \omega_z]/3}{\bar{\omega}} \frac{\hbar\bar{\omega}}{k_BT_c} - \frac{4.932T^3\tilde{a}_s}{T_c^3\zeta(3)\bar{l}} \sqrt{\frac{k_BT}{\hbar\bar{\omega}}} \text{ within the Hartree-Fock (H-F) ap-}$ proximation to the lowest order in the s-wave scattering length \tilde{a}_s [37, 57, 56]. This form of the condensate fraction would not change for the slow rotating ($\Omega \lesssim \omega_{\perp}$) Bose gas, though its values of T_c , geometric mean of the angular frequencies ($\bar{\omega} =$ $\sqrt[3]{\omega_+\omega_-\omega_z}$) and the effective length scale $\bar{l}=\sqrt[3]{l_\perp^2l_z}$ would substantially change. The condensate part contributes in the temperature dependence of the differential scattering cross-section according to its weightage $\frac{N_0}{N} = 1 - (T/T_c)^3$. The weak interactions and slow rotation, apart from modifying the condensate fraction, can substantially scale the typical confining length scales $l_{\perp} \rightarrow \nu l_{\perp}$, $l_z \rightarrow \nu l_z$ so as $\bar{l} \rightarrow \tilde{\ell} = \nu \bar{l}$ at the first exponent in Eqn. (3.10) keeping its form unaltered. Finite temperature scaling of \bar{l} has been prescribed in Ref. [53] for the weak attractive interactions ($\tilde{a}_s < 0$) corresponding to the potential energy $\frac{4\pi\hbar^2\tilde{a}_s}{M}\sum_{i,j< i}\delta^3(\mathbf{r}_{0i} - \mathbf{r}_{0j})$ for ultracold bosons in a harmonic trap. We adopt the method prescribed in Ref. [53] for the finite temperature scaling of \bar{l} for the weak repulsive interactions ($\tilde{a}_s > 0$) of the same system under rotation. This scaling theory with a single scaling parameter ν is useful for both the cases of the zero temperature and the finite temperature, especially for $0 \le T < T_c$, because the linear dimensions of the condensate (\bar{l}) and the thermal cloud $(\bar{l}\sqrt{k_BT/\hbar\bar{\omega}}$ [37]) are proportional to each other. Inset-a of figure 3.4 represents finite temperature scaling $(\bar{l} \to \tilde{\ell} = \nu \bar{l})$ of \bar{l} for a weakly interacting rotating harmonically trapped Bose gas within the 4th order in $\tilde{\ell}/\bar{l}-1$ in its H-F energy functional⁶. Thus we show correction due to the finite-size and the inter-scatterer interactions effects to the temperature dependence of $\bar{D}_T(\theta,\phi)$ especially for a smallangle scattering below T_c in the inset-b of figure 3.4. However, the dashed line in the inset-b represents finite-size and inter-scatterer effects on the rotating system within the H-F approximation over the solid line which represents the ideal case for the same set of parameters. One can neglect the effect of interactions from the trend set for $T > T_c$. The effect of the interactions, however, may not necessarily be perturbative for $T \rightarrow 0$ and can be better described within the Thomas-Fermi approximation [26].

The repulsive interactions lead to narrowing of the profile of the net differential scattering cross-section because the condensate broadens up at around $\theta = 0$ due to the repulsive interactions and the scattering amplitude is Fourier decomposed at all the source points of the particle scattering [34]. However, if temperature increases, the occupation probability of the excited states of the scatterers increases which, in turn, leads to large-angle scattering. Coherence is reduced, on the other hand, as

⁶The definition of the H-F energy functional can be found for the harmonically trapped Bose gas for the δ^3 interactions in Refs. [37, 53]. The form of the H-F energy functional does not change under rotation except the modification on the geometric mean ($\bar{\omega}$) of the angular frequencies ω_+ , ω_- and ω_z . Minimization of the H-F energy functional is further needed to determine the scaling parameter ν [53]. Minimization of the grand free energy, however, is not necessarily required to determine the scaling parameter ν for the case of finite temperature because the entropy of the system, which depends on the number distribution of particles, does not change under scaling [53].

the scatterers are found in different energy eigenstates other than the ground state at a finite temperature. Thus reduction of the scattering cross-section is resulted for the increase of the temperature [34]. The temperature, interactions, and finite-size dependencies of the differential scattering cross-section for the particle scattering by the rotating trapped Bose scatterers as described in this sub-section are quite similar to that described in Ref. [34] for the non-rotating case. This is true only for the very slow rotating case ($0 < \Omega \lesssim \Omega_c$). The description would be dramatically different for the fast-rotating case ($\Omega_c \lesssim \Omega \lesssim \omega_{\perp}$) of the interacting scatterers in quasi 2-D.

The case of rapid rotation with the formation of the vortex lattice

Abrikosov lattice of vortices [58] has been experimentally observed on the cross-sectional plane (i.e. x_0-y_0 plane) of the fast rotating ($\Omega_c \lesssim \Omega \lesssim \omega_\perp$) Bose-Einstein condensate (BEC) [2, 3]. The lattice-pattern becomes equilateral triangular with the area of the unit cell $\pi[l_\perp/\sqrt{2}]^2$ in the limiting case of the ultra-fast rotation ($\Omega \to \omega_\perp$) of the BEC [51]. The number of vortices (N_v) becomes comparable to the number of particles in the condensate (N_0) keeping the surface density of vortices ($n_v = M\Omega/\pi\hbar$ [59]) constant in this situation [39, 52]. Melting of the vortices takes place due to the quantum fluctuations in the fast rotating condensate, especially if the boson filling factor ($v_0 = N_0/N_v$) goes below the critical number ~ 8 [60, 51]. However, if Ω is not very close to ω_\perp , then the number of vortices becomes much smaller ($v_0 \lesssim 8$) than the number of particles [52]. The rotating BEC falls into the mean-field quantum Hall regime in this situation [61, 62], and obeys the Gross-Pitaevskii equation [39]

$$\left(-\frac{\hbar^{2}}{2M}\nabla_{0}^{2} - \Omega\hat{L}_{z} + \frac{M}{2}(\omega_{\perp}^{2}r_{\perp_{0}}^{2} + \omega_{z}^{2}z_{0}^{2}) + \tilde{g}|\psi_{0}(\mathbf{r}_{0})|^{2}\right)\psi_{0}(\mathbf{r}_{0}) = \mu\psi_{0}(\mathbf{r}_{0})$$
(3.13)

where μ is the chemical potential of the interacting BEC, the z-axis is chosen to be the symmetric axis of rotation, $\tilde{g}=\frac{4\pi\hbar^2\tilde{a}_s}{M}$ is the coupling constant for hard-core interscatterer interactions as mentioned before, and $\psi_0(\mathbf{r}_0)$ is the many-body ground-state wavefunction for the rapidly rotating BEC. It should be mentioned in this regard that the Gross-Pitaevskii equation though can not capture any finite temperature effect, it is the heart of the description of the rotating trapped BEC [16].

We assume $\mu \ll \hbar \omega_z$, so that the z_0 motion is frozen to its ground state $\phi_0(z_0) = \sqrt{\frac{1}{l_z\sqrt{\pi}}} \mathrm{e}^{z_0^2/2l_z^2}$ [39]. The coupling constant, however, takes the form $\tilde{g} = \frac{2\sqrt{2\pi}\hbar^2\tilde{a}_s}{Ml_z}$ in the case of quasi 2-D ($l_\perp \gg l_z \gg a_s$) [52]. The theory simplifies in the quasi 2-D, rapid rotation ($\Omega \gg \sqrt{\omega_\perp^2 - \Omega^2}$) and weak-interaction ($\tilde{g}n_{2D} \ll \hbar\omega_z$ and $\tilde{g}n_{2D} < 2\hbar\omega_\perp^7$) limit [51]. The radial part (i.e the $x_0 - y_0$ part) of the many-body wavefunction in this situation, takes the form of the linear superposition of the single-particle states

⁷Here n_{2D} is the areal number density of bosons at the center of the trap while it was not rotating.

For rapidly rotating Bose-Einstein condensate

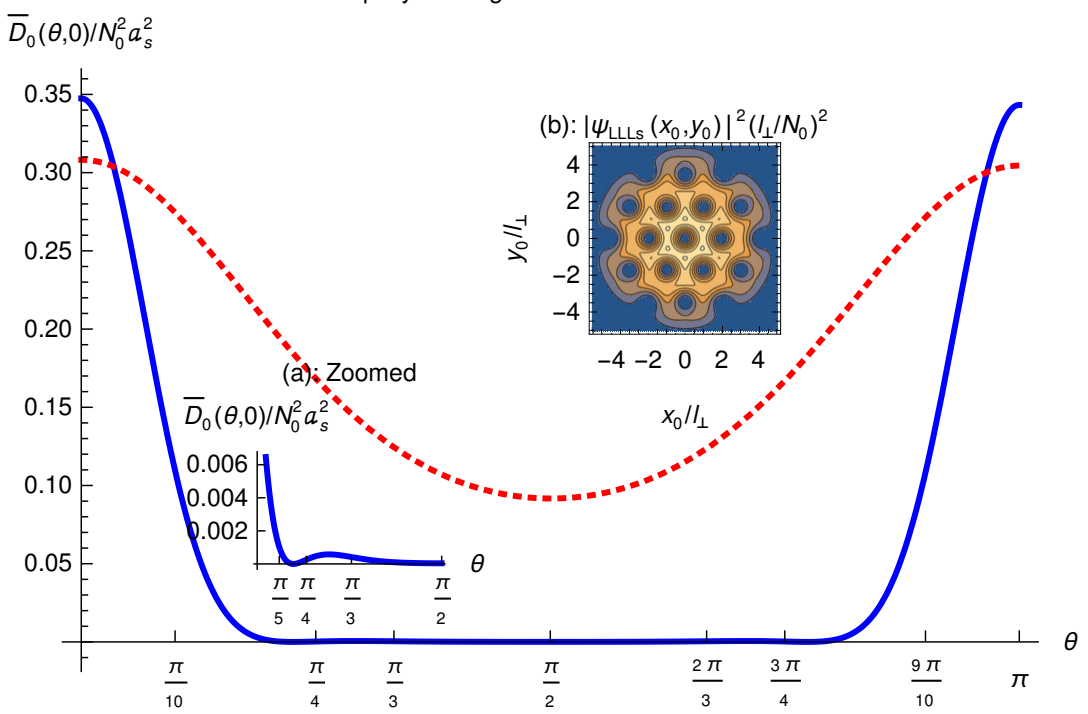


FIGURE 3.5: Net differential scattering cross-section (solid line) for the scattering of a 'particle' $(\bar{A}e^{ikz})$ by the rapidly rotating quasi 2-D weakly interacting trapped Bose-Einstein condensate. The solid line follows Eqn. (3.16) for $\bar{m}/M=0.1$, $a_s=l_\perp$, $l_z=20l_\perp$, $kl_\perp=\frac{2\bar{\pi}}{(3/2)(4\pi/\sqrt{3})^{1/2}}$, and $R=5l_\perp$. Inset-a represents zoom of the same around $\theta=\pi/4$. Inset-b follows from modulus square of the r.h.s. of Eqn. (3.14), and represents the Contour plot for the symmetric-axis integrated probability distribution of bosons as well as the distribution of vortices in the x_0-y_0 plane for the same parameters. The dotted line follows Eqn. (3.10) and represents the net differential scattering cross-section for the same parameters except for the change $\tilde{a}_s=0$ and $T\to 0$.

 $(\psi_{LLLs}(\mathbf{r}_{\perp_0})$ [62]) in the lowest Landau level (LLL), so that the many-body ground state (within the symmetric gauge in the cylindrical coordinate system) takes the form $\psi_0(\mathbf{r}_0) = \psi_{LLLs}(\mathbf{r}_{\perp_0})\phi_0(z_0)$, where [52]

$$\psi_{LLLs}(\mathbf{r}_{\perp_0}) = \sqrt{N_0} \frac{\tilde{f}(r_{\perp_0}, \phi_0)}{l_{\perp}} e^{-r_{\perp_0}^2/2l_{\perp}^2}, \tag{3.14}$$

$$\tilde{f}(r_{\perp_{0}},\phi_{0}) \simeq \frac{(2\nu')^{\frac{1}{4}}}{\sqrt{\alpha\beta}} \sum_{j=-\infty}^{\infty} \sum_{m'=0}^{\lfloor \frac{R^{2}}{l_{\perp}^{2}} \rfloor} \frac{r_{\perp_{0}}^{m'} e^{i(\phi_{0} + \frac{\pi}{2})m'}}{l_{\perp}^{m'} 2^{m'/2} m'!} \sqrt{\frac{R^{2}}{l_{\perp}^{2}} - m'} \\
(-1)^{\frac{j(j-1)}{2}} H_{m'} \left(\sqrt{\frac{\pi\nu'}{2}} (2j+1)\right) e^{-\frac{\pi\nu'(2j+1)^{2}}{4}}, \tag{3.15}$$

 $v'=\sqrt{3}/2$, $\alpha\simeq 1.1596$ (for triangular lattice), $\beta=N_0\tilde{g}/[l_\perp^2\hbar(\omega_\perp-\Omega)]$ and $R=\sqrt{\mu/[\hbar(\omega_\perp-\Omega)]}l_\perp=(2\alpha\beta/\pi)^{1/4}l_\perp$ is the Thomas-Fermi radius of the rotating BEC [52]. It should be mentioned in this regard that the Thomas-Fermi approximation can give rise to effective densities of the harmonically trapped BEC for $T\to 0$ [36, 37]. The Thomas-Fermi approximation can also be applicable to the slow rotating harmonically trapped BEC. The global density profile of the rapidly rotating harmonically trapped BEC is of the Thomas-Fermi form if the number of vortices is very large [62]. The Thomas-Fermi approximation, however, is not directly useful to determine the local density profiles around the vortices in the rapidly rotating harmonically trapped BEC [52]. Hence we have avoided direct use of the Thomas-Fermi approximation in Eqn. (3.14). This equation can, of course, be applicable for $T\to 0$, but not for T>0.

We represent the distribution of the probability density of bosons (as well as the pattern of the Abrikosov vortex lattice) in the x_0-y_0 plane by the Contour-plot in figure 3.5 (inset b). The net scattering amplitude $(-\frac{\bar{m}g_k}{2\pi\hbar^2}\int |\psi_0(\mathbf{r}_0)|^2 \mathrm{e}^{-i[\mathbf{k}'\cdot\mathbf{r}_{\perp_0}+(\mathbf{k}'-\mathbf{k})\cdot\hat{k}z_0]}\mathrm{d}^3\mathbf{r}_0)$ for the macroscopic scatterer (i.e. for the rapidly rotating interacting quasi 2-D trapped BEC) can now be evaluated, as

$$\bar{f}_{0}(\theta,\phi) = a_{k} \frac{(2\nu')^{\frac{1}{2}}}{\alpha\beta} e^{-\bar{q}_{z}^{2}l_{z}^{2}} \sum_{j=-\infty}^{\infty} \sum_{j'=-\infty}^{\infty} \sum_{m'=0}^{\infty} \frac{1}{2^{m'}(m'!)^{2}} \times \left[\frac{R^{2}}{l_{\perp}^{2}} - m' \right] (-1)^{\frac{j(j-1)}{2}} (-1)^{\frac{j'(j'-1)}{2}} \times H_{m'} \left(\sqrt{\frac{\pi\nu'}{2}} (2j+1) \right) H_{m'} \left(\sqrt{\frac{\pi\nu'}{2}} (2j'+1) \right) \times e^{-\frac{\pi\nu'(2j+1)^{2}}{4}} \times \pi\Gamma(1+m') L_{-(1+m')} (-q_{\perp}^{2}l_{\perp}^{2}). \tag{3.16}$$

The first exponent in Eqn. (3.16) is coming from the frozen motion along the z_0 axis and is negligible for $l_z \ll l_{\perp}$. While the radial (r_{\perp_0}) part of the integration results in the Laguerre polynomial in Eqn. (3.16), the angular (ϕ_0) part of the integration results in ϕ -independence in $\bar{f}_0(\theta,\phi)$ even for the discrete symmetry in the lattice structure. We plot the net differential scattering cross-section $\bar{D}_0(\theta,\phi) = |\bar{f}_0(\theta,\phi)|^2$ (solid line) in figure 3.5 for the scattering of the 'particle' ($\bar{A}e^{ikz}$) by the rapidly rotating BEC for parameters as shown in the figure caption. The Thomas-Fermi radius $R = 5l_{\perp}$ of the rotating condensate is taken to be smaller $(R = 5l_{\perp})$ than the one observed for ultra-fast rotation [63] for plotting figure 3.4. However, the triangular lattice of vortices for such a small Thomas-Fermi radius of the rotating BEC, was also experimentally observed [2]. We also compare the same with the one (dotted line) having no inter-scatterer interactions into account. It is clear from figure 3.4 (insetb) that the repulsive interaction lowers the differential scattering cross-section near around the forward direction. This causes substantial narrowing of the scatteringintensity distribution as clear in figure 3.5. It can also be qualitatively explained from the fact that the repulsive interactions flattens the many-body wavefunction at the center of the trap [37]. However, the 'particle' can pass through the vortices and interfere thereafter causing significant increment of the forward differential scattering cross-section and significant narrowing of the scattering-intensity distribution. The first zero of the scattering-intensity distribution can be qualitatively obtained from the diffraction-grating's intensity distribution formula, and is expected to be at around the polar-angle θ_1 , such that $N_{x_0}d\sin(\theta_1)\sim 1\frac{2\pi}{k}$ where $d=\sqrt{4\pi/\sqrt{3}l_{\perp}/\sqrt{2}}$ is the lattice constant [51] and $N_{x_0}=3$ is the number of vortices in a row along the x_0 axis as shown in figure 3.5 (inset b). The wave-number $k = \frac{2}{3} \frac{2\pi}{\sqrt{4\pi/\sqrt{3}l_{\perp}}}$ is chosen in such a way that at least one scattering-intensity minimum with zero intensity takes place in the domain $0 < \theta_1 < \pi$ especially at $\theta_1 \simeq 0.785$ which is close to the actual minimum in the inset-a of figure 3.5. The dotted line, which follows Eqn. (3.10) for $T \rightarrow 0$, however, does not have such a minimum with zero intensity as shown in figure 3.5 because the lattice of vortices is absent for the ideal case of the rotating BEC. Both the curves in figure 3.5 have appeared symmetric around $\theta = \pi/2$ because we have taken a small value for the wavenumber of the incident 'particle'. Such a symmetry would not have been apparent if we had taken a large value of the wavenumber. In such a case the magnitude of the momentum transfer $-k[1-\cos(\theta)]$, which is associated with the term \bar{q}_z in Eqns. (3.16) and (3.10), would reduce the probability of the backscattering.

Purpose of plotting figure 3.5 was to theoretically probe the lattice-pattern of the vortices in a rapidly rotating Bose-Einstein condensate by the particle scattering method. We have taken large wavelength⁸ of the incident 'particle' for this purpose. Incident 'particle' of smaller wavelength could better probe the lattice-pattern resulting in more maxima and more minima of the net differential scattering cross-section on the θ -axis due to the interference of the 'particle' with itself while passing through

⁸Here large wavelength means wavelength comparable to the lattice constant.

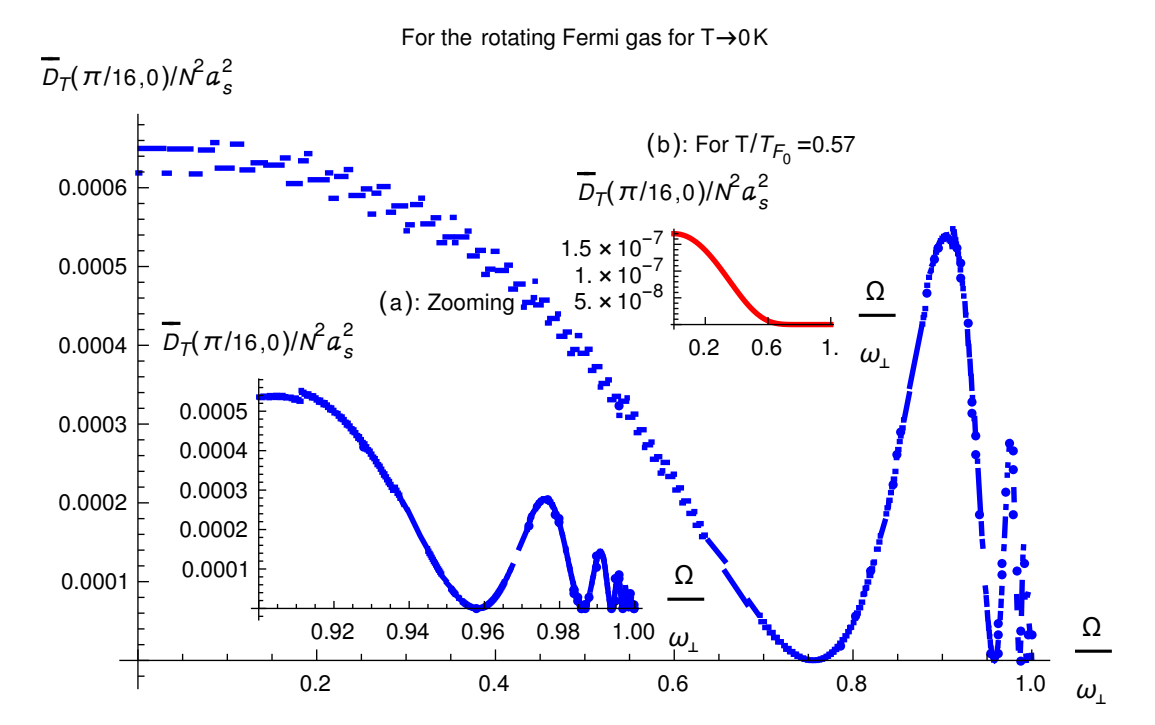


FIGURE 3.6: The angular speed dependence of the net differential scattering cross-section for the scattering of a 'particle' ($\bar{A}e^{ikz}$) by the ideal Fermi gas of rotating 3-D harmonic oscillators (40 K atoms) for $T \to 0$ K, $\bar{m}/M = 0.1$, $ka_s = 2$, $l_\perp = a_s$, $\omega_\perp/10 = \omega_z = 20\pi$ Hz, and $N = 0.5 \times 10^5$. The plot follows Eqn. (3.17). The plot in the inset-a represents zooming of the same for $0.9 < \Omega/\omega_\perp < 1$. The plot in the inset-b follows Eqn. (3.10) for the same parameters except for the temperature T = 0.88 T_{F0} .

the vortices. Probability of the large-angle scattering by the vortex lattice, however, is low for the small wavelength of the incident 'particle'. For this reason, we have not considered the small wavelength for plotting figure 3.5. However, Fermi gas can also form an Abrikosov lattice [5] and therefore one can expect similar scattering results.

3.4 Probing artificial de Haas-van Alphen effect by elastic particle scattering

Artificial de Haas-van Alphen effect [23, 24] can be theoretically probed by the particle scattering method for a gas of uncharged fermions (at a temperature T and chemical potential μ) in the rotating trap because the Lorentz force is analogous to the Coriolis force in the rotating frame. To use the particle scattering method, let us consider the ideal case of a rotating harmonically trapped Fermi gas of identical uncharged particles, each with spin $s_z=1/2$ and mass M. Weak inter-scatterer interactions $(\frac{4\pi\hbar^2\tilde{a}_sn(0)}{M}\ll k_BT_F^9)$ will again not lead to any significant change as long as the Fermi gas is concerned [37].

⁹Here $n(\mathbf{0})$ is the number density of fermions at the center of the trap.

We need to study the angular velocity dependence of the net differential scattering cross-section for probing the artificial de Haas-van Alphen effect at a low temperature, say, zero temperature. The net differential scattering cross-section, for both the slow rotation and the fast rotation (0 < Ω < ω_{\perp}) of the Fermi system, can be obtained by following Eqn. (3.9), for $T \to 0$, as

$$\bar{D}_{T\to 0}(\theta,\phi) = |Na_{k}|^{2} e^{-2[q_{\perp}^{2}l_{\perp}^{2} + \bar{q}_{z}^{2}l_{z}^{2}]} \times \left[\frac{L^{1}_{\sqrt{\frac{6N\bar{\omega}^{3}}{\omega_{\perp}^{3}}} - 1}(q_{\perp}^{2}l_{\perp}^{2})}{\lceil \sqrt[3]{\frac{6N\bar{\omega}^{3}}{\omega_{\perp}^{3}}} \rceil} \times \frac{L^{1}_{\sqrt{\frac{6N\bar{\omega}^{3}}{\omega_{\perp}^{3}}} - 1}(q_{\perp}^{2}l_{\perp}^{2})}{\lceil \sqrt[3]{\frac{6N\bar{\omega}^{3}}{\omega_{\perp}^{3}}} \rceil} \frac{L^{1}_{\sqrt{\frac{6N\bar{\omega}^{3}}{\omega_{z}^{3}}} - 1}(2\bar{q}_{z}^{2}l_{z}^{2})}{\lceil \sqrt[3]{\frac{6N\bar{\omega}^{3}}{\omega_{\perp}^{3}}} \rceil} \right]^{2}}{\lceil \sqrt[3]{\frac{6N\bar{\omega}^{3}}{\omega_{\perp}^{3}}} \rceil}$$
(3.17)

where $\sqrt[3]{6N\hbar^3\bar{\omega}^3} = \epsilon_F$ is the Fermi energy of the system and $\frac{1}{w_+}:\frac{1}{w_-}:\frac{1}{w_-}:\frac{1}{\omega_z}$ is the ratio of the occupation numbers of the Fermi-scatterers distributed to the quantum numbers n, m and j of the single-participle states $\{|n,m,j\rangle\}$.

We plot Eqn. (3.17) in figure 3.6 for the parameters as shown in the figure caption. The plot (solid line) in figure 3.6 (so as that in the inset-a) represents the angular speed dependence of the net differential scattering cross-section for the scattering of a 'particle' ($\bar{A}e^{ikz}$) by the Fermi gas of rotating 3-D indistinguishable harmonic oscillators (40K atoms). Fermi temperature is varying in figure 3.6 as it depends on Ω . However, the Fermi temperature of the system in the non-rotating situation is a fixed quantity, say $T_{F_0} = 2.70976 \times 10^{-7}$ K, for the parameters as mentioned in the figure caption. Zeros of the differential scattering cross-section in figure 3.6 is coming from the zeros of associated Laguerre polynomial $(L^1_{[x]}(y))$ for fixed argument in Eqn. (3.17). Since the zeros are appearing in the quasi-regular interval of the inverse of the angular speed of rotation (Ω) and the angular speed (Ω) corresponds to the magnetic field B for the analogy of the Coriolis force and the Lorentz force, the appearance of the zeros in the quasi-regular interval of $\frac{\omega_{\perp}}{\Omega}$ of the net differential scattering cross-section corresponds to the artificial de Haas-van Alphen effect. The zeros appear in the regular interval of the inverse of the external magnetic field in the actual de Haas-van Alphen effect on a homogeneous Fermi system of charged particles [50]. The quasi-periodicity is appearing for the inhomogeneity of the system of our consideration. Thus one can probe the artificial de Haas-van Alphen effect by the particle scattering method in the ultra-cold situation with the experimentally achievable parameters as mentioned in the caption of figure 3.6. This was the main purpose of plotting figure 3.6. The artificial de Haas-van Alphen effect would be prominent at a lower temperature [50]. We plot Eqn. (3.10) in the inset-b of figure 3.6 for comparing the same effect at a higher temperature with that at absolute zero. The discontinuities in the differential scattering cross-section are coming due to the shifts of population to the higher energy eigenstates as the angular speed is lowered

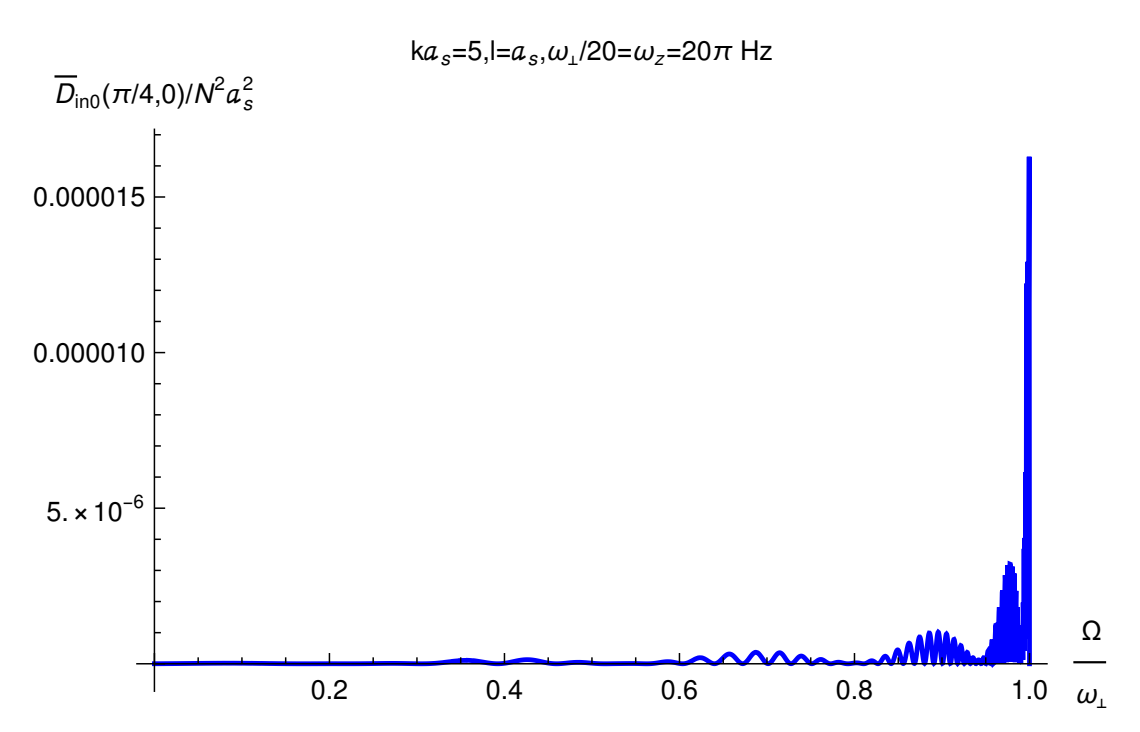


FIGURE 3.7: Net differential scattering cross-section variation with angular speed for the inelastic particle scattering by rotating harmonic oscillator at temperature $T \to 0$ K with $N = 3 \times 10^5$,and $\bar{m}/M = 0.1$.

from $\Omega = \omega_{\perp}$ for $T \to 0$ K. The discontinuities in the de Haas-van Alphen-like oscillations are coming in singlets, doublets and triplets because of the shifts of the occupation from the quantum numbers j; j, m'; and j, m', n, respectively, in single-particle energy eigenstate $|\psi_{n,n-m',j}\rangle$. These discontinuities would be disappeared at a non-zero finite temperature, as all the energy levels $\{\epsilon_{n,n-m',j}\}$ are now populated due to thermal excitations in the system [50]. The de Haas-van Alphen-like oscillations would be further disappeared at a higher temperature $(T \gtrsim T_F)$, as clear from the inset-b of figure 3.6 [50].

3.5 Probing artificial de Haas-van Alphen effect by inelastic particle scattering

This section contributes an intuitive explanation of the oscillatory behavior of net inelastic differential scattering cross-section at low temperatures. The inelastic scattering of a particle by a rotating harmonic trap has been explained in detail in Ref.[64]. Let us consider the case of a rotating trapped spin $s_z=1/2$ identical charge-less non-interacting particles each mass M at T=0. The figure. 3.7 represents the net differential scattering cross-section as a function of the angular speed of rotation . We have shown the possibility of observing similar de Haas-van Alphen oscillation effects for ultra-cold fermionic gas(40 K atoms), by placing the gas in rotation. As shown in the figure 3.7 the slow-rotating region differential scattering cross-sections

3.6. Conclusions 87

show oscillations with a small amplitude. The quasi-periodicity appears in the figure) due to the inhomogeneity of the system. In the fast-rotating region in figure 3.7, differential scattering cross-sections show the most pronounced oscillations with a large amplitude. The oscillation becomes less pronounced with increasing temperature. This happens due to the loss of the sharpness of the Fermi surface. So, one can say, quantum oscillations are controlled by the sharpness of the Fermi surface. Inelastic scattering takes part crucial role near the Fermi surface. The trapped scatterers are disturbed by the fermi-energy level n^*-1 . Some remarkable properties like electric, transport properties of solid, and optical properties are closely related to the Fermi surface. Those properties are analogous to the dHvAE oscillations of the magnetization in the solid-state context.

3.6 Conclusions

To conclude, we have presented the quantum theory of particle scattering by quantum scatterers in their quantized bound states in rotating harmonically trapped geometry for Fermi-Huang δ_p^3 [35] interaction (between the incident particle and a scatterer) which, though is easy to deal with, has huge applications in the field of ultracold systems [65, 37]. We have obtained results for all possible values of the angular speed of rotation ($\Omega \leq \omega_\perp$) so as for the slow and the fast rotations. We have theoretically probed the lattice-pattern of the vortices in a rapidly rotating Bose-Einstein condensate by the particle scattering method. Particle scattering by the quantum scatterers in thermal equilibrium in the rotating geometry of optical traps has not been investigated before us. The particle scattering would be an important tool for probing the collective properties of the rotating trapped Bose and Fermi gases, in particular, the Bose-Einstein condensation [16], vortices in the rapidly rotating Bose-Einstein condensate [1, 15], and the artificial Haas-van Alphen effect on the rotating gas of neutral atomic fermions [23, 24].

The discontinuity in the slope of the net differential scattering cross-section at $T = T_c$ for the nonzero polar angle, as shown in figure 3.4, can be used to detect the onset of the Bose-Einstein condensation by the particle scattering method. Our result in figure 3.5 can be used to study scalar diffraction by the Abrikosov vortex lattices. We have proposed how an alternative method, say the particle scattering method as resulted in figures 3.6, 3.7, can be taken up for observing the artificial de Haas-van Alphen effect on the rotating trapped Fermi gas of neutral scatterers. Our predictions can be tested within the present-day experimental setups.

Parameters taken for plotting figures 3.4, 3.5 and 3.6 are not specific to a particular scattering problem. Some of the parameters though are taken from available experimental data, question still comes – whether the results we have obtained in these figures are really observable in the particle scattering experiments. While most of the Bose scatterers are found in the single-particle ground state and scatter the incident particle coherently at a low temperature, the Fermi scatterers are distributed

among the single-particle states and scatter the incident particle incoherently even at the low temperature. This has caused a lowering of the net differential scattering cross-section for the Fermi systems with respect to that for the Bose systems. While the increase of the number of scatterers (N) would ease experimentalists to verify our results on the Bose systems, choosing an optimal number 10 of scatterers would ease experimentalists to verify our results on the Fermi systems.

Here, we have considered only elastic scattering. Inelastic scattering has a low probability at a finite temperature. Moreover, differential scattering cross-section in inelastic channels decays exponentially with the number of scatterers beyond a certain value [26]. Inelastic scattering at a low temperature, however, would be important and experimentally observable [25] in the resonance condition i.e. when the energy of the incident particle matches with the energy gap of the two consecutive energy levels of a single scatterer.

Here, we have considered only repulsive interactions among the Bose scatterers. The behaviour of Bose gases with attractive interactions differs significantly from those with repulsive interactions. Attractively interacting Bose gas is metastable below a critical number of particles and it undergoes a collapse beyond the critical number [66, 67, 68, 53]. However, as long as the Bose gas is metastable, the attractive interactions lead to broadening up of the profile of the net differential scattering cross-section around $\theta=0$ because the condensate narrows down around the center of the trap due to the attractive interactions.

A large number of experimental observations have been made on the harmonically trapped ultracold Bose and Fermi gases within the last two decades. Coherent scattering by the rotating trapped Bose or Fermi gas in the finite geometry gives rise to a tool of probing its quantum statistical properties [34]. Our prediction of the net differential scattering cross-sections, especially those in Eqns. (3.10), (3.17), and (3.16) (or those represented in figures 3.4, 3.5, and 3.6) may open interests to the experimentalists for studying the temperature dependence in particle scattering by the slow and fast rotating trapped Bose and Fermi systems.

It needs generalization of Sommerfeld asymptotic expansion for analysing the de Haas-van Alphen-like oscillations at a low-temperature ($T \ll T_F$). We have done the same for $T \to 0$ as shown in figure 3.6. Derivation of the Sommerfeld asymptotic expansion for the net differential scattering cross-section at a non-zero low temperature is kept as an open problem.

Our work on the temperature dependence of the net differential scattering cross-section can be extended for weakly interacting rotating trapped Fermi scatterers, in particular, for attractive interactions which lead to the formation of the Cooper pairs [38, 69]. The s-wave scattering length (\tilde{a}_s) of such a Fermi system, however, changes its sign across the BCS-BEC crossover and the two-body interactions become strongly attractive [70]. Eventually, there emerge two kinds of "bound" states,

 $^{^{10}}$ We are talking about an optimal number about the Fermi scatterers because the differential scattering cross-section according to Eqn. (3.17) increases as N^2 and decreases as $\sim e^{-\alpha N^{1/3}}$ [34].

3.6. Conclusions

such as the Cooper pairs (in the BCS regime) and the diatomic molecules formed by the pairs of the Fermi atoms (in the BEC regime) [38, 69, 70]. Further study of the particle scattering on the same system under rapid rotation across the BCS-BEC crossover would be even more interesting because (i) the elementary excitation spectra are different in the BCS and BEC regimes [38, 69] and (ii) number of vortices, which form Abrikosov lattice in the system, changes across the BCS-BEC crossover [5]. Our work can also be extended for both the elastic scattering and inelastic scattering of particles by the Bose-Einstein condensates or Fermi superfluids in a rotating double-well [71] or optical lattice [72].

Scaling theory can not, however, be applied to the study of the particle scattering for the attractively interacting rotating trapped Fermi gas because the excitation spectrum of the Cooper pairs, which form bound states, look completely different from that of the free particle spectrum [69]. Scaling theory can, of course, be applied to the repulsively interacting rotating trapped Fermi gas because the fermions don't form bound states and the number density of the fermions decreases at the centre of the trap due to its expansion for the repulsive interactions [38, 73]. The issue with the scaling theory for the repulsively interacting rotating trapped Fermi gas is kept as an open problem.

Bibliography

- [1] M. R. Matthews, B. P. Anderson, P. C. Haljan, D. S. Hall, M. J. Holland, J. E. Williams, C. E. Wieman, and E. A. Cornell, Phys. Rev. Lett. 83, 3358 (1999)
- [2] K. W. Madison, F. Chevy, W. Wohlleben, and J. Dalibard, Phys. Rev. Lett. 84, 806 (2000)
- [3] J. R. Abo-Shaeer, C. Raman, J. M. Vogels, and W. Ketterle, Science 292, 476 (2001)
- [4] P. C. Haljan, I. Coddington, P. Engels, and E. A. Cornell, Phys. Rev. Lett. 87, 210403 (2001)
- [5] M. W. Zwierlein, J. R. Abo-Shaeer, A. Schirotzek, C. H. Schunck, and W. Ketterle, Nature 435, 1047 (2005)
- [6] I. Bloch, J. Dalibard, and W. Zwerger, Rev. Mod. Phys. 80, 885 (2008)
- [7] R. Srinivasan, Pramana J. Phys. **66**, 3 (2006)
- [8] R. P. Feynman, Int. J. Theor. Phys. 21, 467 (1982)
- [9] L. D. Landau and E. M. Lifshitz, *Quantum Mechanics*, 3rd ed., Sec. 112, p. 458, Butterworth-Heinemann, Oxford (1980)
- [10] V. Schweikhard, I. Coddington, P. Engels, V. P. Mogendorff, and E. A. Cornell Phys. Rev. Lett. **92**, 040404 (2004)
- [11] Y. -J. Lin, R. L. Compton, K. Jiménez-García, J. V. Porto, and I. B. Spielman, Nature 462, 628 (2009)
- [12] J. Dalibard, F. Gerbier, G. Juzeliūnas, and P. Öhberg, Rev. Mod. Phys. 83, 885 (2011)
- [13] P. Rosenbusch, D. S. Petrov, S. Sinha, F. Chevy, V. Bretin, Y. Castin, G. Shlyapnikov, J. Dalibard, Phys. Rev. Lett. 88, 250403 (2002)
- [14] A. Jacob, P. Öhberg, G. Juzeliūnas, and L. Santos, New J. Phys. 10, 045022 (2008)
- [15] N. R. Cooper, Advances in Physics **57**, 539 (2008)
- [16] A. L. Fetter, Rev. Mod. Phys. 81, 647 (2009)
- [17] A. L. Fetter and C. J. Foot, *Bose Gas: Theory and Experiment*, Ch. 2 of *Ultracold Bosonic and Fermionic Gases*, Ed. by K. Levin, A. L. Fetter, and Dan M. Stamper-Kurn, Elsevier, Amsterdam, Netherlands (2012)

[18] N. Goldman, G. Juzeliunas, P. Ohberg, and I. B. Spielman, Rep. Prog. Phys. 77, 126401 (2014)

- [19] B. Lacroix-A-Chez-Toine, S. N. Majumdar, and G. Schehr, Phys. Rev. A 99, 021602(R) (2019)
- [20] S. Medjedel, K. Bencheikh, Phys. Lett. A 383, 1915 (2019)
- [21] W. J. de Haas and P. M. van Alphen, Proc. Netherlands Roy. Acad. Sci. 33, 680 (1930)
- [22] L. D. Landau and E. M. Lifshitz, *Statistical Physics*, Part 1, 3rd ed., sec. 59 and 60, p. 171-176, Butterworth-Heinemann, Oxford (1980)
- [23] G. Juzeliūnas and P. Öhberg, Phys. Rev. Lett. Phys. Rev. Lett. 93, 033602 (2004)
- [24] B. Farias and C. Furtado, Physica B: Cond. Matt. 481, 19 (2016)
- [25] A. P. Chikkatur, A. Görlitz, D.M. Stamper-Kurn, S. Inouye, S. Gupta, and W. Ketterle, Phys. Rev. Lett. 85, 483 (2000)
- [26] Z. Idziaszek, K. Rzazewski, and M. Wilkens, J. Phys. B: At. Mol. Opt. Phys. **32**, L205 (1999)
- [27] A. Wynveen, A. Setty, A. Howard, J. W. Halley, and C. E. Campbell, Phys. Rev. A **62**, 023602 (2000)
- [28] H.-J. Wang, X.-X. Yi, X.-W. Ba, and C.-P. Sun, Phys. Rev. A 64, 043604 (2001)
- [29] U. V. Poulsen, Ph.D. Thesis, University of Aarhus (2002)
- [30] A. Montina, Phys. Rev. A 66, 023609 (2002)
- [31] H.-J. Wang, and W. Jhe, Phys. Rev. A 66, 023610 (2002)
- [32] I. Haring, Ph.D. Thesis, TU Dresden (2003)
- [33] U. V. Poulsen and K. Molmer, Phys. Rev. A 67, 013610 (2003)
- [34] A. Bhattacharya, S. Das, S. Biswas, J. Phys. B: At. Mol. Opt. Phys. **51**, 075301 (2018)
- [35] E. Fermi, Ricerca Sci. 7, 13 (1936); K. Huang and C. N. Yang, Phys. Rev. 105, 767 (1957)
- [36] F. Dalfovo, S. Giorgini, L. P. Pitaevskii, and S. Stringari, Rev. Mod. Phys. 71, 463 (1999)
- [37] L. P. Pitaevskii and S. Stringari, *Bose-Einstein Condensation*, Oxford Sc. Pub. (2003)
- [38] S. Giorgini, L. P. Pitaevskii, and S. Stringari, Rev. Mod. Phys. 80, 1215 (2008)

[39] S. Stock, B. Battelier, V. Bretin, Z. Hadzibabic, and J. Dalibard, Laser Phys. Lett. **2**, 275 (2005)

- [40] Y. Li and Q. Gu, Phys. Lett. A 378, 1233 (2014)
- [41] D. J. Griffiths, *Introduction to Quantum Mechanics*, 2nd ed., Pearson Education, Singapore (2005)
- [42] S. Bodefeld and M. Wilkens, Quantum Semiclass. Opt. 8, 511 (1996)
- [43] M. Wakamatsu, Y. Kitadono, and P.-M. Zhang, Annals of Physics 392, 287 (2018)
- [44] V. Halonen, Solid State Communications 92, 703 (1994)
- [45] V. Fock, Z. Physik 47, 446 (1928); C. G. Darwin, Math. Proc. Cambridge Philos. Soc. 27, 86 (1931)
- [46] L. D. Landau, Z. Physik 64, 629 (1930)
- [47] P. Lederer and M. O. Goerbig, Lecture Notes *Introduction to the Quantum Hall Effects*, p. 48-49, Universite de Paris-Sud, Orsay (2006). The result in this reference was obtained for symmetric gauge in the Cartesian coordinate system with n m in $L_{n-m}(q_1^2 l_1^2)$ of Eqn.(3.5) be replaced by m' = 0, 1, 2, ...
- [48] A. H. MacDonald, H. C. A. Oji, and K. L. Liu, Phys. Rev. B 34, 2681 (1986); A. S. Alexandrov, W. H. Beere, and V. V. Kabanov, Phys. Rev. B 54, 15363 (1996)
- [49] S. Biswas and D. Jana, Eur. J. Phys. 33, 1527 (2012)
- [50] S. Biswas, S. Sen, and D. Jana, Phys. Plasmas 20, 052503 (2013)
- [51] J. Sinova, C. B. Hanna, and A. H. MacDonald, Phys. Rev. Lett. 89, 030403 (2002)
- [52] S. I. Matveenko, D. Kovrizhin, S. Ouvry, and G. V. Shlyapnikov, Phys. Rev. A 80, 063621 (2009)
- [53] S. Biswas, Eur. Phys. J. D 55, 653 (2009)
- [54] J. R. Ensher, D. S. Jin, M. R. Matthews, C. E. Wieman, and E. A. Cornell, Phys. Rev. Lett. 77, 4984 (1996)
- [55] S. Dey, P. Manchala, S. Basu, D. Banerjee, and S. Biswas, Phys. Scr. **95**, 075003 (2020)
- [56] S. Biswas, Phys. Lett. A **372**, 1574 (2008)
- [57] S. Giorgini, L. P. Pitaevskii, and S. Stringari, Phys. Rev. A 54, R4633 (1996)
- [58] A. A. Abrikosov, J. Exptl. Theoret. Phys. (U.S.S.R.) 32, 1442 (1957); Soviet Phys. JETP 5, 1174 (1957)

[59] R. P. Feynman, in: C.J. Gorter (ed.), *Progress in Low Temperature Physics*, vol. 1, chapter 2, North-Holland, Amsterdam (1955)

- [60] N. R. Cooper, N. K. Wilkin, and J. M. F. Gunn, Phys. Rev. Lett. 87, 120405 (2001)
- [61] T.-L. Ho, Phys. Rev. Lett. 87, 060403 (2001)
- [62] G. Watanabe, G. Baym, and C. J. Pethick, Phys. Rev. Lett. 93, 190401 (2004)
- [63] V. Bretin, S. Stock, Y. Seurin, and J. Dalibard, Phys. Rev. Lett. 92, 050403 (2004)
- [64] S. Das, Phys. Lett. A 397, 127249 (2021)
- [65] T. Busch, B. G. Englert, K. Rzazewski, and M. Wilkens, Foun. of Phys. 28, 549 (1998)
- [66] C. C. Bradley, C. A. Sackett, R. G. Hulet, Phys. Rev. Lett. 78, 985 (1997)
- [67] J. L. Roberts, N. R. Claussen, S. L. Cornish, E. A. Donley, E. A. Cornell, and C. E. Wieman, Phys. Rev. Lett. 86, 4211 (2001)
- [68] G. Baym, C. J. Pethick, Phys. Rev. Lett. 76, 6 (1996)
- [69] M. M. Parish, *The BCS-BEC Crossover*, Ch. 9 of *Quantum Gas Experiments Exploring Many-Body States*, Ed. by P. Törmä and K. Sengstock, Imperial College Press, London (2014)
- [70] M. Randeria and E. Taylor, Annual Rev. Cond. Matt. Phys. 5, 209 (2014)
- [71] S. Hofferberth, I. Lesanovsky, B. Fischer, J. Verdu, and J. Schmiedmayer, Nat. Phys. 2, 710 (2006)
- [72] S. Tung, V. Schweikhard, and E. A. Cornell, Phys. Rev. Lett. 97, 240402 (2006)
- [73] S. Biswas, D. Jana, and R. K. Manna, Eur. Phys. J. D 66, 217 (2012)

Chapter 4

Particle scattering by harmonically trapped quantum gases exposed to an artificial magnetic field

4.1 Introduction

The role of magnetic fields on the nature of physical systems is important in the study of problems in plasma physics, astrophysics, and solid-state physics, where magnetic fields play an important role in their properties [1, 2]. There are several existing works that have been reported on the structure of matter in the presence of a magnetic field [1, 2]. The electron gas subjected to an artificial magnetic field has been of interest since the early days of quantum mechanics and is connected with several interesting consequences of the quantum origin. The Fermi system has connected with it several interesting phenomena, such as de Haas-van Alphen oscillations, the integer and fractional quantum Hall effect and the fractal energy spectrum of the Hofstadter butterfly, etc. The de Haas - van Alphen (dHvA) effect[3, 4], which is concerned with the oscillation in the magnetic moment with a varying magnetic field, is one of them. It was predicted long before by Landau and has played an important role ever since. There are a few excellent examples where trapping is required, the Bose-Einstein condensate has been reached in various atomic species[5],molecules formed with the support of light [6, 7], threshold scattering characteristics have been investigated [8], and quantum phase transitions has been observed using optical lattices [9]. In most of these phenomena's, atomic collisions are crucial. In the context of ultra-cold atom traps, the experimental observation of scattered light at very narrow angles has already been done. Coherently diffracted light was used to capture the thrilling images of condensation into an atomic trap ground state. The Bragg scattering has been investigated for identifying the phase singularity of a single vortex [10]. There are some existing works related to particle scattering by trapped quantum gases [11, 12, 13] have been reported before. There is some theoretical evidence related to the dHvA effect for neutral atomic Fermions in an artificial magnetic field [14]. But they did not study the particle scattering method to show the dHvA effect. The electron scattering from atomic gases trapped in a 4.1. Introduction 95

magneto-optical trap (MOT) has been investigated experimentally [15]. All those evidences encourage us to continue our theoretical progress. In the existing literature, we have seen scattering is the only method one can obtain some information about the structure and properties of metal. Theoretical investigations of particle scattering from trapped scatterer in an artificial gauge field plays a crucial role since the scattering spectra can contributes the trapped scatter thermodynamic, magnetic properties, etc. A synthetic magnetic field is formed by the gradient of a real magnetic field [16] and is called for having the same effect on neutral particles as a true magnetic field has on a charged particles. The synthetic magnetic field can be generated for atoms trapped in an optical lattice by inducing an asymmetry in the atomic tunnelling between the lattice sites [17, 18]. Without trapping in lattice, an artificial magnetic field for cold atoms can be created. This case, several laser beams are used to create position-dependent transitions between distinct atomic internal states [14, 19]. Mainly, Juzeliūnas et al [14] demonstrated how a degenerate gas of electrically neutral Fermionic atom can be used to generate an artificial magnetic field using slow light having an orbital angular momentum. The synthetic magnetic fields can be created in a laboratory, by hitting two counterpropagating laser beams on an ultracold gas cloud of ⁸⁷Rb atoms[20]. In a synthetic magnetic field, the neutral atoms are manipulated in such a way, as if they behave as charged particles in a real magnetic field [16]. It is then necessary to know how neutral particles interact in the presence of a homogeneous magnetic field at low energy. The major goal of our study is to figure out how the trapped neutral Bose and Fermi scatterers are influenced by the magnetic field. To our knowledge, there is no theoretical progress of this problems. This article gives a very intriguing path to investigate several fundamental physical problems such as the artificial dHvA effect, atomic optics, phase transition, and various statistical topics in condensed matter physics.

We assume that the incident particle's beam spreads the entire trap uniformly. We show how confinement affects scattering and calculate the total scattering amplitude associated with collision-induced transitions between scatterer states in the confining potential. We study the temperature dependence of the differential crosssection of scattering for a plane wave incident on a harmonic trap containing N number of non-interacting scatterers in an artificial magnetic field. We find that scattered particle intensity can exhibit oscillatory and this oscillatory behaviour looks at zero Kelvin temperature, and the intensity depends on geometric shapes of trapped fermionic cloud. All of our calculations are obtained at finite temperatures, but the thermodynamic properties of the Fermi scatterer are greatly important at lowtemperature (say zero Kelvin temperature). In this paper, we employed Born approximation scattering for a plane wave of the particle in an in-homogeneous medium of Bosonic and Fermionic scatterers as a function of scattering angle and temperature. The quantum statistics of trapped scatterers have a big impact on small angle particle scattering from a quantum gas of degenerate cloud. A transition between trap states of recoiling scatterers characterize the scattering of an incident incoming

particle. The scatterer's trap state remains unaltered in an elastic scattering process, and the scattered particle's momentum is equal to the incoming particle's momentum. For inelastic scattering process $|\mathbf{k}| \neq |\mathbf{k}'|$ which means that the incident particle gives up some of its kinetic energy to the confined scatterer, and the internal states

of the both scatterers are not equal. For this reason the energy being transformed into vibrations that can be interpreted as heat, waves (sound), or vibrations between the component particles between the particles of the two collision partners. However, in both elastic and inelastic scattering, momentum is conserved.

4.2 Scattering by trapped quantum gases in an artificial magnetic field at finite temperatures

In this section, we will show the expressions of the differential cross sections for the elastic scattering as well as the inelastic particle scattering by the trapped scatterers. The differential scattering cross-section is an essential physical quantity to explain the scattering characteristics. The starting point in our study, we consider a system of non-interacting neutral quantum gases in an artificial magnetic field. The Hamiltonian for single non-interacting particle can be represented as

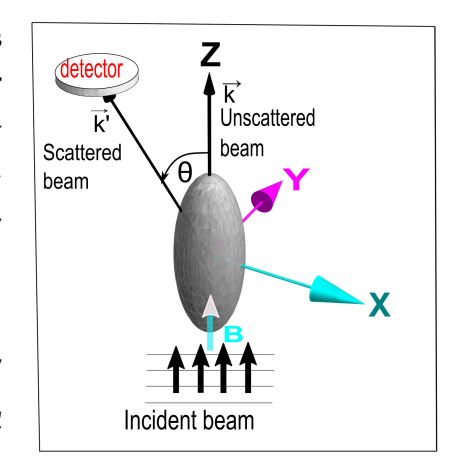


FIGURE 4.1: A schematic scattering geometry for the scattering of a particle by the 3-D harmonically trapped scatterers in an artificial magnetic field. The incident direction defines the Z-axis in a Cartesian coordinate system. The scattering plane is defined by the incident direction and scattering direction. \mathbf{k}' is the scattered wave vector makes an angle θ with the Z-axis.

$$H = \left[\frac{(\mathbf{p} - q'\mathbf{A})^2}{2M} + \frac{1}{2}M(\omega_{\perp}^2 r_{\perp}^2 + \omega_z^2 z^2) \right]$$
 (4.1)

where M is the mass of a harmonically trapped particle. The charge q' feeling an external applied magnetic field and the linear momentum of the particle is \mathbf{p} . $r_{\perp} = \sqrt{x^2 + y^2}$ is the radius in the transverse plane. We have applied the magnetic field along the z-axis and considering the symmetric gauge $\mathbf{A} = \frac{1}{2}B(-y,x,0)$. In our discussion, we have neglected all static atom-atom interaction effects. While the properties of a magnetic system are gauge independent. We consider the Zeeman spin splitting is neglected. It is well known that the solution of Eqn. (4.1) can be

written in the from at position \mathbf{r}_0 [21, 22]

$$\psi_{n,m,j}(\mathbf{r}_{0}) = \sqrt{\frac{1}{2\pi}} \frac{2}{l^{2}} \frac{(n - [|m| + m]/2)!}{(n + [|m| - m]/2)!} e^{-im\phi_{0}} \times \left(\frac{r_{\perp_{0}}^{2}}{l^{2}}\right)^{|m|/2} e^{-\frac{r_{\perp_{0}}^{2}}{2l^{2}}} L_{n-\frac{|m|+m}{2}}^{|m|} \left(\frac{r_{\perp_{0}}^{2}}{l^{2}}\right) \times \sqrt{\frac{1}{\sqrt{\pi}l_{z}}} \frac{1}{\sqrt{2^{j}j!}} H_{j}(z_{0}/l_{z}) e^{-z_{0}^{2}/2l_{z}^{2}}.$$
(4.2)

There are two length scales $l=\sqrt{\frac{\hbar}{M\sqrt{\omega_{\perp}^2+\Omega^2}}}$ and $l_z=\sqrt{\frac{\hbar}{M\omega_z}}$, for the transverse and the axial direction respectively. $L_n^m(x)$ is associated Laguerre polynomial of order n and $H_i(z)$ is the Hermite polynomial of order j. Neutral particle (cold scatterer) does not feel a force from the external magnetic field and does not have cyclotron frequency. Here we have defined parametrize the synthetic field strength = $\frac{q'B}{M} = 2\Omega$. The corresponding single-particle energies of the scatterer are [21, 23]

$$\epsilon_{n,n-m',j} = (n+\frac{1}{2})\hbar\Omega_{+} + (m'+\frac{1}{2})\hbar\Omega_{-} + (j+\frac{1}{2})\hbar\omega_{z}$$
(4.3)

where $\Omega_- = \sqrt{\omega_\perp^2 + \Omega^2} - \Omega$, $\Omega_+ = \sqrt{\omega_\perp^2 + \Omega^2} + \Omega$. The quantum number $n \ge 0$ is known as Fock- Darwin level index [24, 25]. The quantum number $m \ge 0$ is the azimuthal quantum number. Hence, m' = n - m varies from 0 to ∞ . When $\frac{\Omega}{\omega_{\perp}} \to 0$ the single-particle energies reduce to Landau-level energies $E_{n,m}=(n+\frac{1}{2})\hbar\Omega$. The contributions of all energy levels are included in thermodynamics. With the increasing magnetic field, the neutral particle behaviour prevails over the confinement. For high magnetic field $\Omega \gg \omega_{\perp}$, then in x-y plane the energy $\to (2n+1)\hbar\omega_{\perp}$ for positive m. For B = 0 one get usually spaced spectrum of 3-D symmetric harmonic oscillator, where the degeneracy goes larger with higher energies. We consider the incident particle beam is propagating along the z-direction which is orthogonal to the x-y plane of confinement of the scatterer. The Fermi-Huang interaction describes the short-range interaction between the incident particle and the scatterer

$$V_{int}(\mathbf{r}) = g\delta_v^3(\mathbf{r} - \mathbf{r}_0). \tag{4.4}$$

Here, r is the incident particle position such that the scattere's center trapped potential is at $\mathbf{r} = 0$ and scatterer position is at \mathbf{r}_0 . We chose the above potential because it is short enough to distinguish between the scattered and unscattered states. To introduce the scattering theory, let us start the quantize motion of the scatterers in a harmonically trap geometry in the presence of artificial magnetic field. The particle scattering occurs at all the possible positions $\{r_0\}$ of the scatterer inside a harmonically trap geometry i.e $0 < r_{0\perp} < \infty$, $-\infty < z_0 < +\infty$, and $0 < \phi_0 < 2\pi$. The probability of finding the scatterers inside the trap in elementary volume d^3r_0 is $|\psi_{n,m,j}(\mathbf{r}_0)|^2 d^3 r_0$ for the given state $\psi_{n,m,j}$ w.r.t initial state of momentum **k**. The

Coulomb interactions between the particle and the scatterer in a quantum dot are negligible when we take the harmonic oscillator confinement length is small enough compared with the effective Bohr radius. When evaluating the scattered amplitude from two atoms, there will be a phase difference because the atoms are spatially distributed. The phase factor is fully independent of the scattering potential and is determined only by the position of the atoms. The key matrix element that determines the elastic scattering amplitude relating the trap state $|\psi_{n,m,j}\rangle$ [11] for a single scatterer the following expression

$$f_{n,m,j}(\theta,\phi) = -\frac{\tilde{m}g_k}{2\pi\hbar^2} \langle \psi_{n,m,j} | e^{-i[\mathbf{k}' \cdot \mathbf{r}_{\perp_0} + (\mathbf{k} - \mathbf{k}') \cdot \hat{k}z_0]} | \psi_{n,m,j} \rangle$$

$$= A_k e^{-2q_\perp^2 l^2} L_n(q_\perp^2 l^2) L_{n-m}(q_\perp^2 l^2) e^{-\bar{q}_z^2 l_z^2} L_j(2\bar{q}_z^2 l_z^2)$$
(4.5)

where $A_k = -\frac{mg_k}{2\pi\hbar^2} = -\frac{a_s m/\mu}{1+ika_s m/\mu}$ [11], $q_\perp = k\sin(\theta)/2$, $\bar{q}_z = k[1-\cos(\theta)]/2$, and $\mathbf{k} - \mathbf{k}'$ is the momentum transfer in the direction of the magnetic field. However,the scattering amplitude always depends on the chosen gauge and all the physical observables are gauge invariant. For inelastic scattering case, the transition amplitude denoting an excitation of the final trap state from the state initial trap state. This means that any change of its momentum in the direction of the magnetic field is associated with the transition between Landau levels. The scatterer gas is assumed to be formed by either Bose or Fermi atoms which initially are considered to be ideal. Effects of the statistics of the scattered particle are considered irrelevant. The scattering amplitude is presented by the Fourier transform of the mean atomic density distribution. The elastic scattering processes differential cross sections for the single atom can be expressed explicitly by

$$D_{n,m,j}(\theta,\phi) = |A_k e^{-q_\perp^2 l^2} L_n(q_\perp^2 l^2) L_{n-m}(q_\perp^2 l^2) e^{-\bar{q}_z^2 l_z^2} L_j(2\bar{q}_z^2 l_z^2)|^2.$$
 (4.6)

The above expression for the coherent spectrum taken for the case of non-interacting atoms. From the scattering amplitude expression Eqn. (4.5), the node of oscillation can be determined along the θ -axis after counting the sum of quantum number 2n-m+j. As we can see, all that is required to evaluate the coherent spectrum is knowledge of the mean atomic density at equilibrium. For the purpose of figure plotting, we set $\tilde{m}/M=0.1$, which is suitable for a Fermionic scatterer with 40 K atom and 4 He scattered particle or projectile. Although the ratio of \tilde{m}/M for the combination of 87 Rb atom (Bosonic scatterer) and 4 He (scattered particle) would be even lower (0.046), our result would not alter significantly [11]. For the elastic scattering process figure 4.2 shows, we get the central maximum peak at zero incident scattering angle and broadened as a consequence of the finite transverse and axial size of the atomic cloud. The scattering cross-section quickly decays due to the exponential factor in Eqn. (4.6) far from the central maximum peak. At higher values of the θ the scattering contribution to the diffraction pattern almost vanishes.

Of course, the scattering cross-section and its thermal properties may themselves

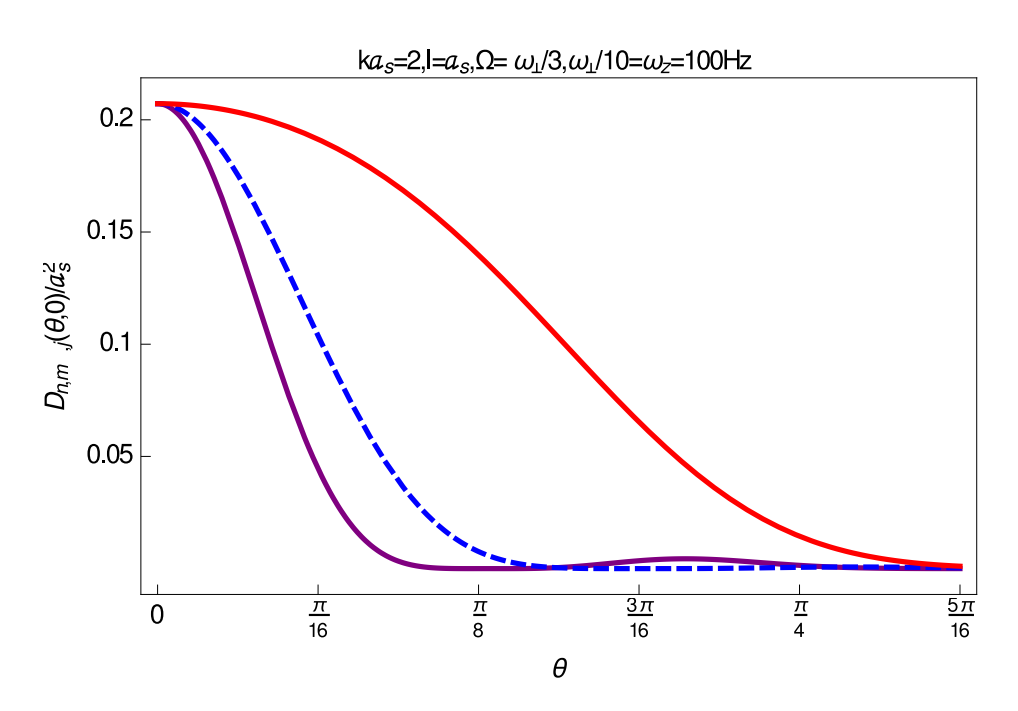


FIGURE 4.2: The elastic differential cross section as a function of the scattering angle θ . The purple thick line, blue dashed thick line, and red thick lines lead the cross-sections of scattering $D_{5,1,0}$, $D_{2,0,0}$, $D_{0,0,0}$ respectively.

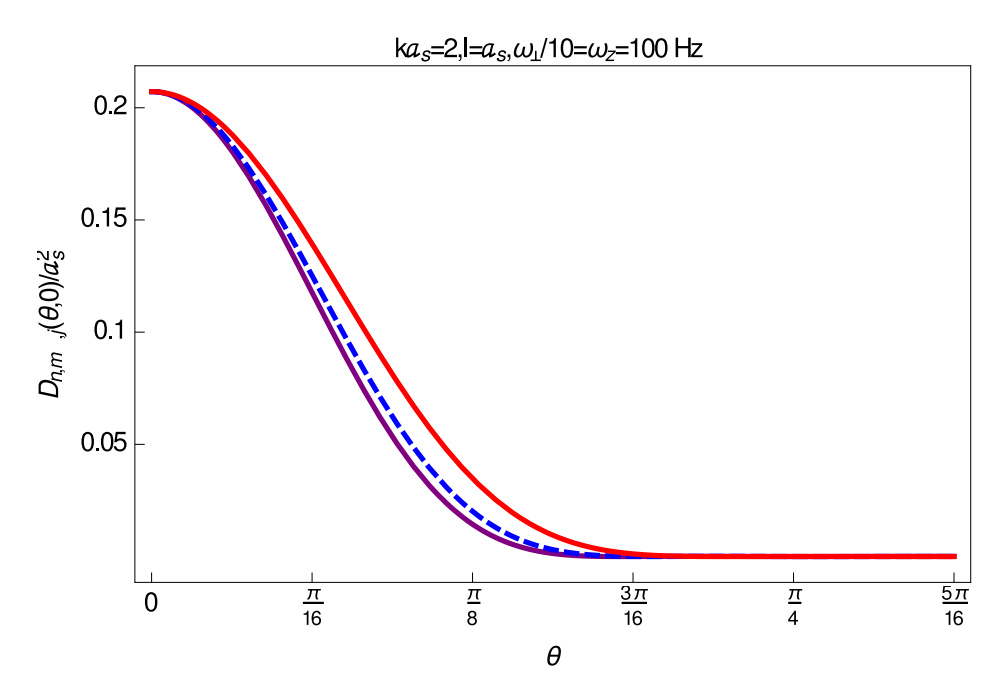


FIGURE 4.3: Angular dependencies of elastic scattering cross-section with difference synthetic magnetic field parameter. The blue dashed thick line, purple thick and red thick lines lead the cross-sections of scattering for wave function $\psi_{2,1,0}$ with $\frac{\Omega}{\omega_{\perp}}$ ratio $\frac{1}{2}$, 0 and 1 respectively.

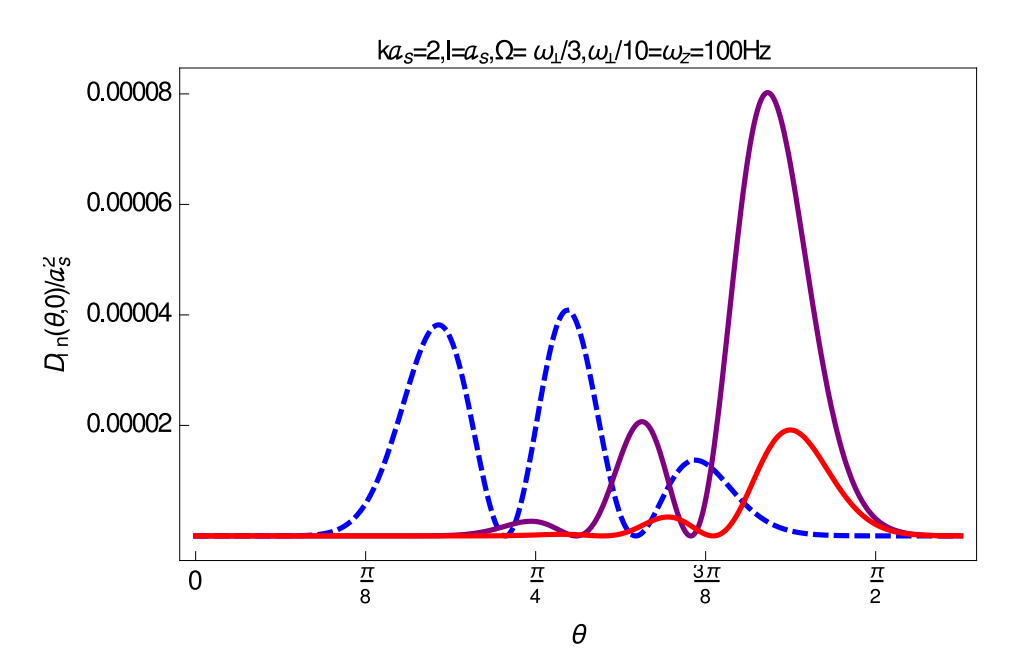


FIGURE 4.4: The inelastic differential cross section as a function of the scattering angle θ . The value of $\{(n,h1),(m',h2),(j,h3)\}$ are taken $\{(2,1),(2,3),(2,4)\}$ respectively.

be profoundly dependent on quantum statistics. Let us imagine all the ideal scatterers remain in the thermodynamic equilibrium with its surroundings at temperature T having the chemical potential μ . Now consider the many body case, the temperature dependence elastic cross-section of scattering for ideal scatterers can be denoted as

$$\bar{D}_{T}(\theta,\phi) = \left[\sum_{n=0,m'=0,j=0}^{\infty,\infty,\infty} \frac{f_{n,m,j}(\theta,\phi)}{e^{(\epsilon_{n,n-m',j}-\mu)/k_{B}T} \mp 1}\right]^{2}.$$
(4.7)

The strong magnetic field situation at low temperature is special interest in quantum dots. A quantum dot is usually defined as an artificial atom, in which a confinement potential substitutes the attractive potential of the nucleus and the extended length scale allows access to experiments that are not usable on real atoms [26, 27]. Another interesting phenomenon dHvA effect be observed only in high magnetic fields and at low temperatures. With the increase of magnetic field the oscillation of crosssection increases. Now we are esspecially interested to study thermodynamic properties of neutral Fermi scatterers in particular at low temperatures. The Fermionic system has many stacked energy levels at low temperatures [28, 29]. The Bosonic system, on the other hand, condenses nicely to a few of the lowest energy levels. At zero temperature limit, there are $n = 0, 1, \dots n^* - 1$ Landau levels completely occupied, n^* level only occupied partially. n^* is the principal quantum number corresponds to the Fermi surface. When k_BT falls below the Fermi energy E_F , phase matching becomes less significant. Then the importance of quantum statistics of gases grow. When k_BT is less than one-half of E_F , quantum statistics kick in, which is compatible with evaporative cooling [30] and experimental study [31]. As a result,

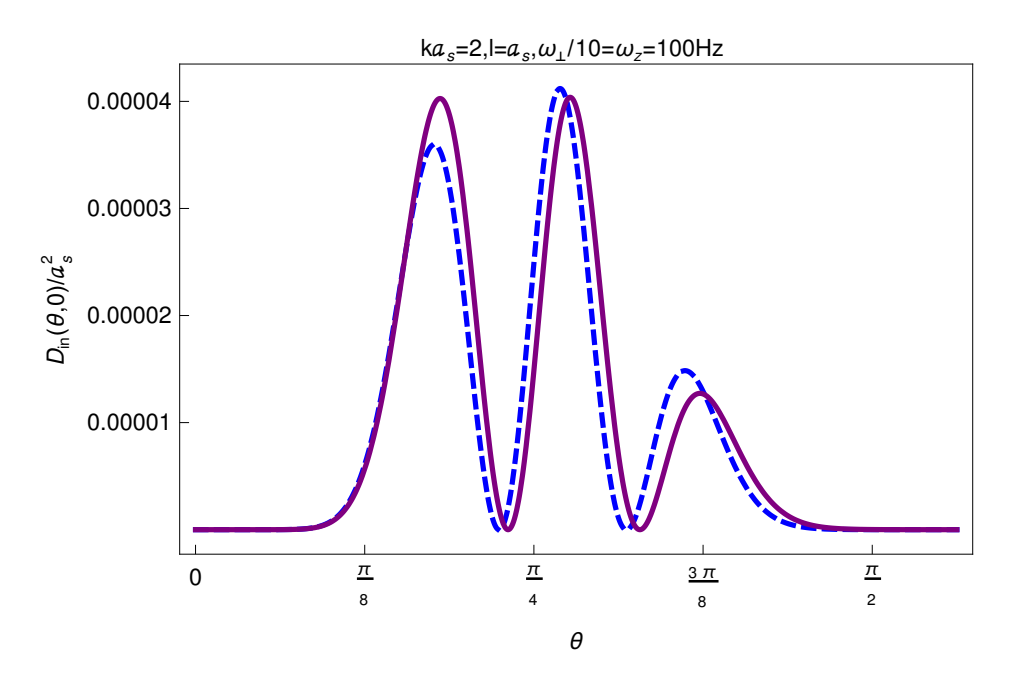


FIGURE 4.5: The differential cross section for the inelastic scattering of neutral scatterers as a function of the scattering angle θ for the different values of synthetic magnetic strength parameter. The blue dashed thick line and purple thick lines represent the inelastic differential scattering cross-sections $D_{(2\to1,2\to1,2\to1)}$ for $\frac{\Omega}{\omega_\perp}$ ratio $\frac{1}{2}$ and 0

Eqn. (4.7) in the zero-temperature limit one can reduce to the simple expression

$$\begin{split} \bar{D}_{T\to 0}(\theta,\phi) &= |NA_{k}|^{2} \mathrm{e}^{-2(q^{2}l^{2} + \bar{q}_{z}^{2}l_{z}^{2})} \left[\frac{L^{1}_{\sqrt[3]{\frac{6N\bar{\Omega}^{3}}{\Omega_{+}^{3}}} - 1}(q_{\perp}^{2}l^{2})}{\sqrt[3]{\frac{6N\bar{\Omega}^{3}}{\Omega_{+}^{3}}}} \right] \\ &\times \frac{L^{1}_{\sqrt[3]{\frac{6N\bar{\Omega}^{3}}{\Omega_{-}^{3}}} - 1}(q_{\perp}^{2}l^{2})}{\sqrt[3]{\frac{6N\bar{\Omega}^{3}}{\Omega_{-}^{3}}}} \frac{L^{1}_{\sqrt[3]{\frac{6N\bar{\Omega}^{3}}{\alpha_{z}^{3}}} - 1}(2\bar{q}_{z}^{2}l_{z}^{2})}{\sqrt[3]{\frac{6N\bar{\Omega}^{3}}{\Omega_{-}^{3}}}} \right]^{2}. \quad (4.8) \end{split}$$

The Eqn. (4.8) has been given by making use of recursion relations for Laguerre polynomials $\sum_{n=0}^{n*} L_n^{\beta}(x) = L_{n*}^{\beta+1}(x)$. At zero Kelvin temperature, the Fermi energy of the harmonic trap is $\hbar \sqrt[3]{6N\bar{\Omega}^3}$ [32] with $\bar{\Omega} = \sqrt[3]{\Omega_+\Omega_-\omega_z}$. The Fermi energy is determined by the number of fermionic scatterers in the trap. The oscillations of elastic cross section occur at low temperature due to the shell effects. There is the shift of cross-section due to the elastic scattering process depends on the Fermi surface at T=0. For the inelastic scattering process, the c.m. and internal states of a scatterer can be excited simultaneously or separately. In the inelastic scattering process, the kinetic energy of the incident particle is transferred to the trapped Fermionic scatterer and this leads to the excitation of the scatter internal state or the c.m. state.

The inelastic-collision cross-section strongly depends on the incident scattering angle. We obtain the expression for the inelastic scattering cross-section for a single scatterer is given by

$$D_{in}(\theta,\phi) = |A_{k}\frac{\mathbf{k}'}{\mathbf{k}}|^{2}e^{-2[q_{\perp}^{2}l^{2} + \bar{q}_{z}^{2}l_{z}^{2}]} \times \left[\frac{n!}{(n+h1)!}(q_{\perp}^{2}l^{2})^{h1}[L_{n}^{h1}(q_{\perp}^{2}l^{2})]^{2} \times \frac{m'!}{(m'+h2)!}(q_{\perp}^{2}l^{2})^{h2}[L_{m'}^{h2}(q_{\perp}^{2}l^{2})]^{2} \times \frac{j!}{(j+h3)!}(2\bar{q}_{z}^{2}l_{z}^{2})^{h3}[L_{j}^{h3}(2\bar{q}_{z}^{2}l_{z}^{2})]^{2}\right]$$
(4.9)

where h1 = n' - n, h2 = m'' - m, h3 = j' - j. Here, h is an integer w.r.t a single-scatterer excitation of the harmonic oscillator. The total scattering amplitude due to transition for initial state to final state as a function of magnetic field strength. Consider the many body effects at zero Kelvin temperature, the inelastic cross-sections is given bellow the following expression

$$\begin{split} \bar{D}_{in_{T\to 0}}(\theta,\phi) &= |NA_{k}\frac{\mathbf{k}'}{\mathbf{k}}|^{2}\mathrm{e}^{-2[q_{\perp}^{2}l^{2}+\bar{q}_{z}^{2}l_{z}^{2}]} \\ &\times \left[\sum_{n=\max\{N_{x}-h1,0\}}^{N_{x}-1} \frac{n!}{(n+h1)!} (q_{\perp}^{2}l^{2})^{h2} [L_{n}^{h1}(q_{\perp}^{2}l^{2})]^{2} \right. \\ &\times \sum_{m'=\max\{N_{y}-h2,0\}}^{N_{y}-1} \frac{m'!}{(m'+h2)!} (q_{\perp}^{2}l^{2})^{h2} [L_{m'}^{h2}(q_{\perp}^{2}l^{2})]^{2} \\ &\times \sum_{j=\max\{N_{z}-h3,0\}}^{N_{z}-1} \frac{j!}{(j+h3)!} (2\bar{q}_{z}^{2}l_{z}^{2})^{h3} [L_{j}^{h3}(2\bar{q}_{z}^{2}l_{z}^{2})]^{2} \right] \quad (4.10) \end{split}$$

where N_x , N_y , N_z are the maximum allowed value for the quantum number n, m, j respectively. From figure 4.4, the inelastic particle scattering process we do not obtain the central peak for incident angle $\theta = 0$. The inelastic scattering cross-section is much weaker than the elastic scattering cross-section. Thus, if we plot the inelastic scattering cross-sections vs magnetic field strength, we get clear oscillation behaviour. We have taken in figure 4.6 along the x-axis level the parameter $\frac{B}{\alpha}$. Where the parameter $\alpha = \frac{2m\omega_{\perp}}{q'}$. The period of the oscillations in figure 4.6 is thought to be mainly determined by the energy level spacing between two energy states of the scatterers. Consider the many body effect, the normalized form of elastic cross section of scattering can be written bellow after transforming a triple sum in Eqn. (4.7)

$$\bar{D}_{T}(\theta,\phi) = |NA_{k}|^{2} \left[\frac{\sum_{i=1}^{\infty} \frac{e^{-2q_{\perp}^{2}l^{2} \coth(\frac{i\hbar\Omega_{+}}{2k_{B}T})}}{1 - e^{-\frac{i\hbar\Omega_{+}}{k_{B}T}}} \frac{e^{-2q_{\perp}^{2}l^{2} \coth(\frac{i\hbar\Omega_{-}}{2k_{B}T})}}{1 - e^{-\frac{i\hbar\Omega_{+}}{k_{B}T}}} \frac{e^{-2q_{\perp}^{2}l^{2} \coth(\frac{i\hbar\Omega_{-}}{2k_{B}T})}}{1 - e^{-\frac{i\hbar\Omega_{-}}{k_{B}T}}} \frac{e^{-2q_{\perp}^{2}l^{2} \coth(\frac{i\hbar\Omega_{-}}{2k_{B}T})}}{1 - e^{-\frac{i\hbar\Omega_{-}}{k_{B}T}}} \frac{e^{-2q_{\perp}^{2}l^{2} \coth(\frac{i\hbar\Omega_{-}}{2k_{B}T})}}{1 - e^{-\frac{i\hbar\Omega_{-}}{k_{B}T}}} (\pm 1)^{i+1}\bar{z}^{i}} \frac{1}{1 - e^{-\frac{i\hbar\Omega_{-}}{k_{B}T}}} \right]^{2} (4.11)$$

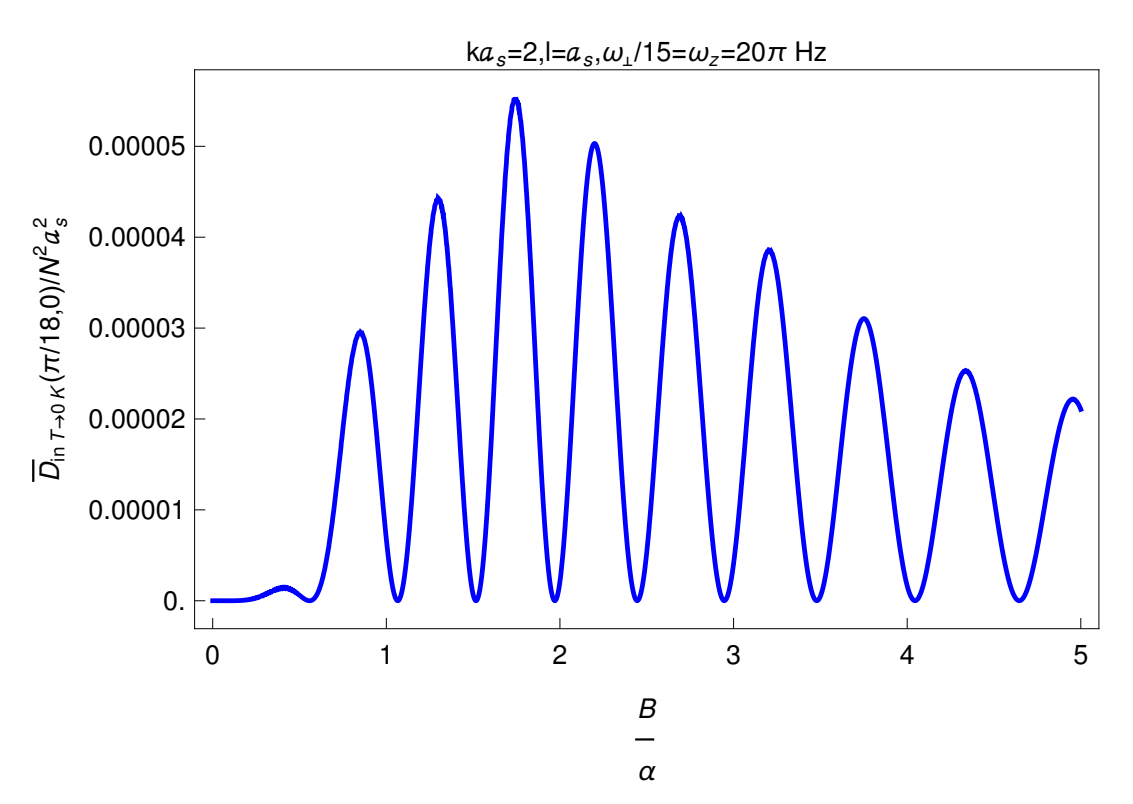


FIGURE 4.6: Magnetic field dependence of the net inelastic differential cross-section of scattering of a 'particle' by 3-D harmonically trapped ideal Fermi gases (40K atoms) in an artificial magnetic field for $T \rightarrow 0$ K, $\tilde{m}/M = 0.1$ and $N = 3. \times 10^5$.

where the fugacity of the system is $\bar{z} = e^{\frac{1}{k_B T} (\mu - \frac{\hbar}{2} (\Omega_+ + \Omega_- + \omega_z))}$. N is the total number of scatterer in the trap. At $N \to \infty$ Eqn. (4.11) can only be suitable for $T > T_c$. It can theoretically be employed at any temperature for finite N, but as $T \to 0$, the convergence of the series in Eqn. (4.11) turns quite slow. Above the Eqn. (4.11) provides the exact differential scattering cross-section for an ideal, harmonically trapped 3D Fermi scatterer at arbitrary temperature and magnetic field strength. The sharpness of the Fermi surface is decreased as temperature rises, resulting in less pronounced oscillations. Of course, at very high temperatures limit the quantum effects are totally washed out. From the figure 4.8, we conclude that the scatterers behave like a classical particle and the Eqn. (4.11) can be described by the Boltzmann's kinetic theory. The scattering cross-section becomes broader as the temperature falls. One can except for a narrow cone in the forward scattering direction, phase matching effects display dominant at high-temperature regime for light scattering situation, when destructive interference attenuates scattering. As T drops, more terms in the sum over i in Eqn. (4.11) involve, resulting in a large number of particles being emitted. At T = 0 K temperature, figures 4.6 and show that the scattering cross-section behaves oscillatory behavious with artificial magnetic field strength and intensity becomes less with higher magnetic field strength. The jumps occur in $\bar{D}_{T\to 0}(\theta,\phi)$.As the artificial magnetic field is increased the figures 4.6 and 4.7 show, the peaks

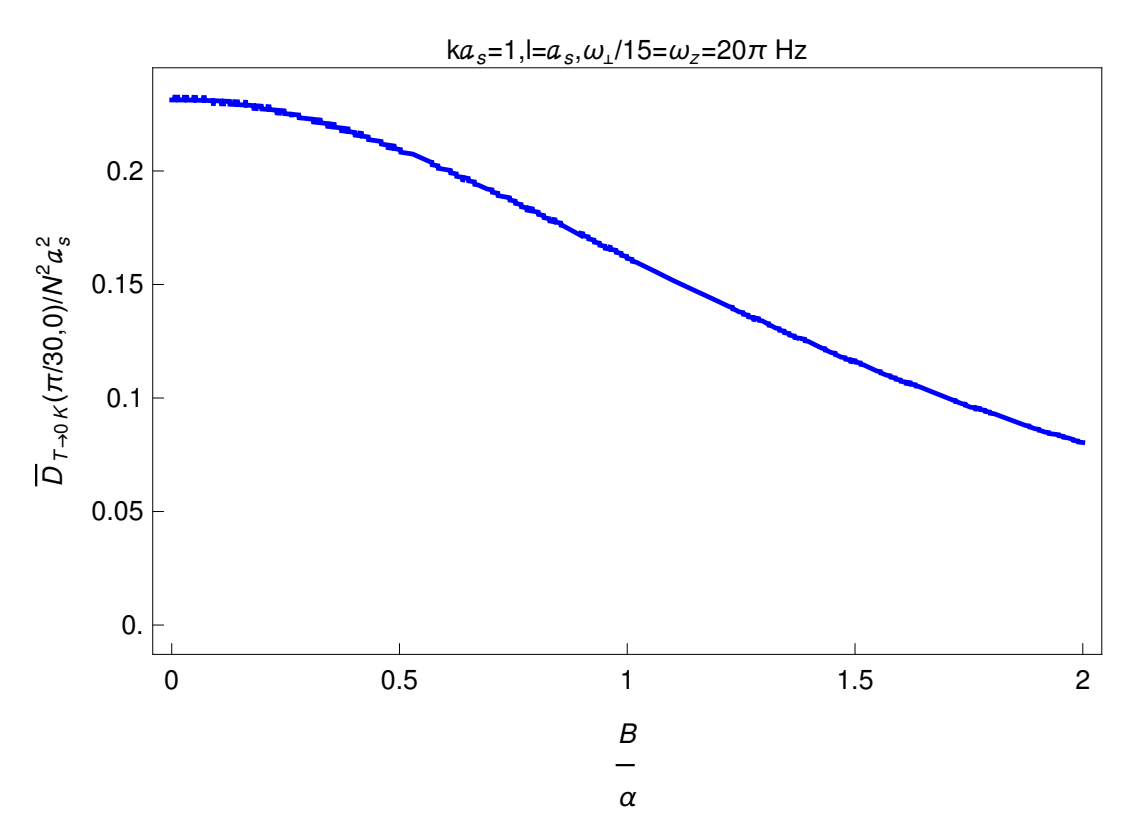


FIGURE 4.7: Magnetic field dependence of the net elastic differential cross-section of scattering of a 'particle' by 3-D harmonically trapped ideal Fermi gases (40 K atoms) in an artificial magnetic field for $T \rightarrow 0$ K, $\tilde{m}/M = 0.1$ and $N = 3 \times 10^5$.

become more and more spaced. For the small numbers of scatterer quantum statistical effect is not clear. But, for huge scatterer numbers quantum statistical outcomes can be more clearly explained in terms of the cross-section of scattering. The intensity for inelastic scattering is discrete due to the external harmonic confinement. But it can be approximated as a continuum in the limit at $\Omega >> \omega_{\perp}, \omega_{z}$. Notably, the oscillations period of the cross section is controlled by the magnetic field strength. With the system parameters, the amplitude of the oscillations will vary significantly. The oscillations are most reasonable when there are enough particle numbers. The oscillation of the cross-section is observable due to its strong dependency on the sharpness of the Fermi surface. The cross-section of scattering figure 4.7 exhibits oscillations with varying the synthetic magnetic field strength. It's worth noting that effects like the Schubnikw-van Alphen and de Haas-van Alphen have identical behaviour for electric resistivity and magnetic susceptibility [34]. The oscillation of the magnetic moment of the atoms as a function of the static magnetic field is known as de Hass-van Alphen oscillation. One observes this for the specimens at low temperature and high magnetic field. Due to the existence of finite Landau sub-levels, one observes the de Haas-van Alphen oscillations at low temperature. The inelastic cross-section of scattering at finite temperature with the presence of a magnetic field for the Bosons is given by

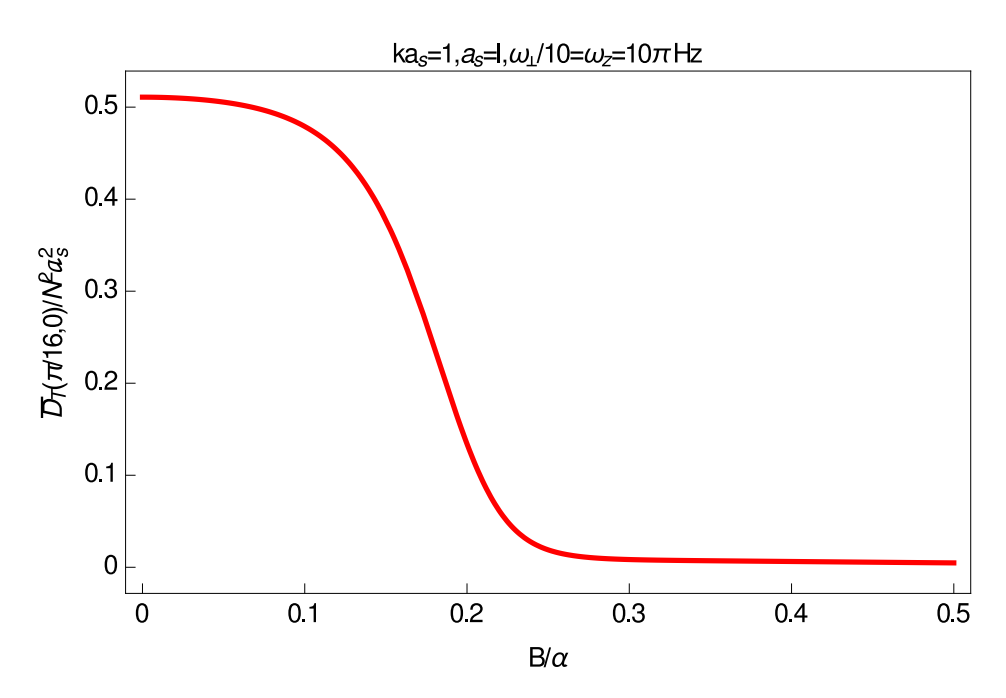


FIGURE 4.8: The elastic cross-section of scattering is plotted with $\frac{B}{\alpha}$ for $N = 3.5 \times 10^5$ number of scatterers at high temperatures.

$$\bar{D}_{T}^{\{n,m',j\to n',m'',j'\}}(\theta,\phi) = |A_{k}\frac{\mathbf{k}'}{\mathbf{k}}|^{2} \sum_{i_{1},i_{2}=1}^{\infty} \bar{z}^{i_{1}+i_{2}} \bar{D}_{+} \bar{D}_{-} \bar{D}_{z}$$
(4.12)

where
$$\bar{D}_{+} = \sum_{n=0,n'=0}^{\infty} e^{-(i_{1}n+i_{2}n')\frac{\hbar\Omega_{+}}{k_{B}T}} e^{-2q_{\perp}^{2}l^{2}} \frac{n!}{(n+h1)!} (q_{\perp}^{2}l^{2})^{h1} [L_{n}^{h1}(q_{\perp}^{2}l^{2})]^{2}$$

$$= \frac{1}{1-e^{-\frac{(i_{1}+i_{2})\hbar\Omega_{+}}{k_{B}T}}} e^{-4q_{\perp}^{2}l^{2}\frac{(1-e^{-\frac{i_{1}\hbar\Omega_{+}}{k_{B}T}})(1-e^{-\frac{i_{2}\hbar\Omega_{+}}{k_{B}T}})}{1-e^{-\frac{(i_{1}+i_{2})\hbar\Omega_{-}}{k_{B}T}}},$$

$$\bar{D}_{-} = \frac{1}{1-e^{-\frac{(i_{1}+i_{2})\hbar\Omega_{-}}{k_{B}T}}} e^{-4q_{\perp}^{2}l^{2}\frac{(1-e^{-\frac{i_{1}\hbar\Omega_{-}}{k_{B}T}})(1-e^{-\frac{i_{2}\hbar\Omega_{-}}{k_{B}T}})}{1-e^{-\frac{(i_{1}+i_{2})\hbar\Omega_{-}}{k_{B}T}}}}$$
and $\bar{D}_{z} = \frac{1}{\frac{(i_{1}+i_{2})\hbar\omega_{z}}{(i_{1}+i_{2})\hbar\omega_{z}}} e^{-4q_{z}^{2}l^{2}\frac{(1-e^{-\frac{i_{1}\hbar\omega_{z}}{k_{B}T}})(1-e^{-\frac{i_{2}\hbar\omega_{z}}{k_{B}T}})}{1-e^{-\frac{(i_{1}+i_{2})\hbar\omega_{z}}{k_{B}T}}}}.$

The inelastic scattering spectrum for the Fermion $\bar{z} < 1$ is retrieved as

$$\bar{D}_{T}^{\{n,m',j\to n',m'',j'\}}(\theta,\phi) = |A_{k}\frac{\mathbf{k}'}{\mathbf{k}}|^{2}\sum_{i_{1},i_{2}=1}^{\infty}(-\bar{z})^{i_{1}+i_{2}}\bar{D}_{+}\bar{D}_{-}\bar{D}_{z}.$$
(4.13)

This limit applies only at high temperatures, when the average energy per atom is significantly higher than the Fermi temperature. Both elastic and inelastic scattering spectra reflect quantum statistical features of atoms because they are completely reliant on \bar{n}_n , which is represented by Bose-Einstein and Fermi-Dirac distributions for Bosons and Fermions, respectively. In the limiting case when $\Omega=0$ and $\Omega_+ = \Omega_- = \omega_z = \omega$, then the simplified form of the many-body net inelastic

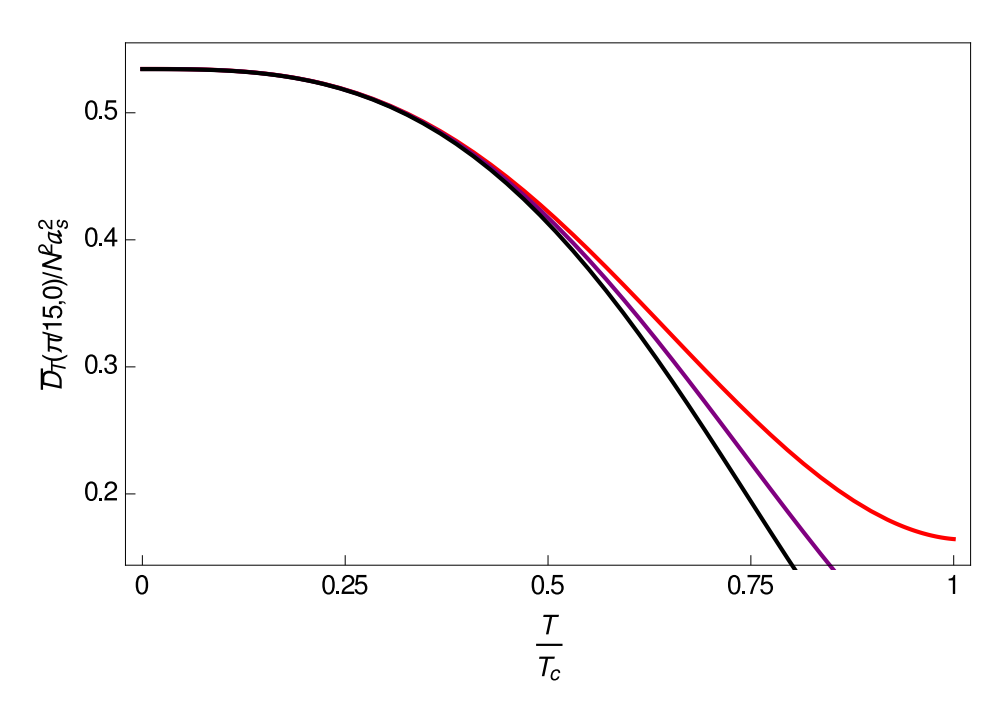


FIGURE 4.9: The dependency of an elastic cross-section of scattering as a function of condensate fraction $\frac{T}{T_c}$ for different values of magnetic field strength and particle numbers. Here we take $\omega_\perp=10\omega_z=10\pi$ The values of $\frac{\Omega}{\omega_\perp}$ and N correspond to the black thick, purple thick, and the red thick lines are $\{\frac{1}{2},1.5\times10^6\},\{\frac{1}{3},1.5\times10^5\}$ and $\{\frac{1}{4},1.5\times10^4\}$ respectively.

cross-section at finite temperature can be expressed as

$$\bar{D}_{T}^{\{n,m',j\to n',m'',j'\}}(\theta,\phi) = |A_{k}\frac{\mathbf{k}'}{\mathbf{k}}|^{2}$$

$$\times \sum_{i_{1},i_{2}=1}^{\infty} (\pm \bar{z})^{i_{1}+i_{2}} \frac{e^{-4q^{2}L^{2}\frac{(1-e^{-\frac{i_{1}\hbar\omega}{k_{B}T}})(1-e^{-\frac{i_{2}\hbar\omega}{k_{B}T}})}}{(1-e^{-\frac{(i_{1}+i_{2})\hbar\omega}{k_{B}T}})^{3}}$$
(4.14)

where the form of L and q are explicitly mentioned in the following section.

4.3 Scattering properties of Bose gases in an artificial magnetic field

A plot of an elastic cross-section of scattering as a function of (T/T_c) for different values of the magnetic field strength B and particle number N is shown in figure 4.9. The figure 4.9 shows that, the case when $N \to \infty$, the condensate fraction reduce to $(1 - \frac{T^3}{T_c^3})$ then the change of magnetic field B will not affect the cross-section of scattering. While in the finite Bose scatterers case, it is obvious that when the value of N decreases or B increases, the value of cross-section of scattering will be lowered as shown in figure 4.9. As the magnetic field increases, the density of the scatterers

4.4. Conclusions 107

in the centre of the trap becomes flatter. For this reason, the value of the condensate temperature shifts towards the origin with the increase of the magnetic field. The elastic differential scattering cross section for Bose scatterer are proportionate to the square of the number of the condensed atoms. This dramatic behaviour of the scattering cross-section is due to the coherence nature of the condensate. The differential scattering cross-sections decrease with increase of temperatures at $T > T_c$ because of coherency reduces. At higher temperatures the particle exist higher excited states rather than the ground state. At $T > T_c$ the large angle scattering is more suitable. But bellow condensate temperatures the particle always ground state. Due to coherent nature of the scattering bellow the T_c the differential scattering cross-sections increase. The small angle scattering is more preferable bellow the T_c . It is possible to achieve external field control of contact inter-particle interactions, for example, by manipulating the scattering length via Feshbach resonance, where the magnetic field, the optical fields [36, 37] can be applied to trap ultracold gases. The experimental realization of fundamental quantum phase transitions, such as the Berezinskii-Kosterlitz-Thuless transition [38] for cold Bosonic atoms confined to 2D and the BEC-BCS crossover in atomic Fermi gases [39], requires this control over interactions and confinement. The fluctuations of the scattering length play a significant role in quantum technologies in association with BEC's as evidenced from the recent theoretical advancement [40].

4.4 Conclusions

In summary, we study the elastic and inelastic scattering processes of an incoming particle by a harmonically trapped neutral 3D Fermi or Bose scatterer in the presence of a synthetic magnetic field. At finite temperature and arbitrary magnetic field strength, we have obtained an exact expression for the differential scattering crosssection. As T becomes less than T_c , intensity distributions of scattered Bosons as well as their numbers vary dramatically. The role of the magnetic field is to control the net differential scattering cross-section for the scattered atoms. The scattering would occur without the magnetic field, as evidenced by recent theoretical progress [11]. The elastic scattering process has an intrinsic coherent property of the atomic BEC. However, the trapped Fermionic scatterer does not have this property. When the number of atoms becomes large enough, the coherent scattering dominates. This kind of method was used to investigate electron impact ionization utilizing 8/Rb atoms trapped in MOT as a target [41]. The temperature dependency of the scattered spectrum shows significant changes. At zero Kelvin temperature, we have illustrated the characteristic oscillations of the differential cross section with magnetic field strength. We have obtained that the atomic gas shows a dHvA type behavior where oscillations in thermodynamic properties depend on magnetic field strength. Incoherent scattering dominates at smaller numbers of atoms and has a weak temperature dependence. When the total number of atoms in a confined Fermi gas is large enough, temperature-dependent qualitative changes in the differential cross-section can be used to investigate quantum degeneracy. The oscillatory behavior of scattering cross-section is especially interesting due to its temperature sensitivity. The elastic scattering of particles (electrons) from atomic nuclei is used to investigate the nuclear charge distribution and the tunability of the elastic scattering cross-section in an optically trapped spin mixture of lithium atoms at high magnetic fields[42], etc.

Bibliography

- [1] Ed. R. Smith, R. J. W. Henry, G. L. Surmelian, R. F. O Connell, and A. K. Rajagopal, Phys. Rev. D 6, 3700 (1972)
- [2] A. R. P. Rau, R. O. Mueller, and Larry Spruch, Phys. Rev. A 11, 1865 (1975)
- [3] W. J. de Haas and P. M. van Alphen, Proc. Netherlands Roy. Acad. Sci. 33, 680 (1930)
- [4] L. D. Landau and E. M. Lifshitz, *Statistical Physics*, Part 1, 3rd ed., sec. 59 and 60, p. 171-176, Butterworth-Heinemann, Oxford (1980)
- [5] M. H. Anderson, J. R. Ensher, M. R. Matthews, C. E. Wieman, and E. A. Cornell, Science **296**, 198 (1995)
- [6] M. Patterson, T. Takekoshi, and R. J. Knize, Phys. Rev. A 59, 2508 (1999)
- [7] R. Wynar, R.S Freeland, D.J Han, C. Ryu, D.J Heinzen, Science 287, 1016 (2000)
- [8] J. Weiner, Vanderlei S. Bagnato, Sergio Zilio, and Paul S. Julienne, Rev. Mod. Phys. 71, 1 (1999)
- [9] M. Greiner, O. Mandel, T. Esslinger, T. W Hansch, I. Bloch, Nature 415, 39 (2002)
- [10] P. B. Blakie and R. J. Ballagh, Phys. Rev. Lett. 86, 3930 (2001)
- [11] A. Bhattacharya, S. Das, S. Biswas, J. Phys. B: At. Mol. Opt. Phys. 51, 075301 (2018)
- [12] S. Das and S. Biswas, Phys. Scr. 96,125037(2021)
- [13] S. Das, Phys. Lett. A 397, 127249 (2021)
- [14] G. Juzeliūnas and P. Öhberg, Phys. Rev. Lett. 93, 03360 (2004)
- [15] R. S. Schappe, P. Feng1, L. W. Anderson, C. C. Lin, and T. Walker, Europhys. Lett. **29**, 439 (1995)
- [16] Y. -J. Lin, R. L. Compton, K. Jiménez-García, J. V. Porto, and I. B. Spielman, Nature 462, 628 (2009)
- [17] D. Jaksch and P. Zoller, New J. Phys. 5, 56 (2003)
- [18] E. J. Mueller, Phys. Rev. A 70, 041603(R) (2004)

110 BIBLIOGRAPHY

[19] K. J. Günter, Marc Cheneau, Tarik Yefsah, Steffen P. Rath, and Jean Dalibard, Phys. Rev. Lett. 93, 03360 (2004)

- [20] please, see synthetic magnetic field
- [21] M. Saito, T. Sasaki, and H. Fukayama, JPSJ.72, 2556 (2003)
- [22] V. Halonen, Solid State Communications. 92, 703 (1994)
- [23] P. Shea and B.P van Zyl, J. Phys. A: Math. Theor. 41, 135305 (2008)
- [24] V. Fock, Z. Physik 47(1928)446; C. G. Darwin, Math. Proc. Cambridge Philos. Soc. 27(1931)86
- [25] L. D. Landau, Z. Physik 64(1930)629
- [26] Marc A. Kastner, Physics Today 46, 1,24 (1993)
- [27] T. Chakraborty, Quantum Dots A survey of the properties of artificial atoms, Elsevier, Amsterdam, 1999
- [28] D. A. Butts and D. S. Rokhsar, Phys. Rev. A 55, 4346 (1997)
- [29] K. Mølmer, Phys. Rev. Lett. 80, 1804 (1998)
- [30] W. Geist, A. Idrizbegovic, M. Marinescu, T. A. B. Kennedy, and L. You, Phys. Rev. A 61, 013406 (1999)
- [31] B. DeMarco, D.S Jin, Science 285, 5434.1703 (1999)
- [32] D. J. Toms, Annals of Physics **04**, 018 (2005)
- [33] A. P. Koller, M. L. Wall, J. Mundinger, and A. M Rey, Phys. Rev. Lett. 117, 195302 (2016)
- [34] A. Zujev, please, see de Haas-van Alphen Effect
- [35] M. Brack, B. P. van Zyl, Phys. Rev. Lett. 86, 1574 (2001)
- [36] I. Bloch, J. Dalibard, W. Zwerger, Rev. Mod. Phys. 80, 885 (2008)
- [37] M. Greiner and S. Fölling, Nature 453, 736 (2008)
- [38] Z. Hadzibabic, P. Krüger, M. Cheneau, B. Battelier, J. Dalibard, Nature 441, 1118 (2006)
- [39] M. Inguscio, W. Keterle, and C. Salomon, *Proceedings of the International School of Physics Enrico Fermi*, Course CLXIV, Varenna, 20-30 June 2006; IOP Press: Amsterdam, 2008
- [40] D. Tsarev, A. Alodjants, T. V. Ngo, and R.K. Lee, New J. Phys. 22, 113016 (2020)

BIBLIOGRAPHY 111

[41] S. Schappe, T. Walker, L. W. Anderson, and Chun C. Lin, Phys. Rev. Lett. **76**, 4328 (1996)

[42] S. Jochim, M. Bartenstein, G. Hendl, J. Hecker Denschlag, R. Grimm, A. Mosk and M. Weidemuller, Phys. Rev. Lett. 89, 273202 (2002)

Chapter 5

Conclusions and future scopes

5.1 Conclusions

Chapter-1 contains the basic elements of the works done in this thesis. Conclusions have already been mentioned at the end of the other chapters. However, brief conclusions of the Ph.D. works, especially the summaries, can be described chapter-wise as follows.

In chapter 2, we have analytically explored the quantum phenomenon of particle scattering by harmonically trapped Bose and Fermi gases for the short ranged Fermi-Huang (δ_p^3) interactions between the incident particle and the scatterers. We have considered elastic scattering. We have predicted differential scattering cross-sections and their temperature dependence in this regard. The coherent scattering even by a single boson or fermion in the finite geometry gives rise to a new tool for determining the energy eigenstates of the scatterer. Our predictions on the differential scattering cross-sections can be tested within the present day experimental setups, specially, for (i) 3-D harmonically trapped interacting Bose-Einstein condensate (BEC), (ii) BECs in a double well, and (iii) BECs in an optical lattice.

In chapter 3, we have analytically explored the quantum phenomena of particle scattering by rotating trapped quantum gases of electrically neutral bosons and fermions for the short-ranged Fermi-Huang interactions between the incident particle and the scatterers. We have considered rotating co-moving frame for all our analyses. We also have considered elastic scattering. We have predicted differential scattering cross-sections and their temperature and angular velocity dependencies in this regard, in particular, for an ideal Bose gas in a rotating harmonic trap, an ideal Fermi gas in a rotating harmonic trap, and a weakly interacting Bose gas in a slow rotating harmonic trap. We have theoretically probed the lattice-pattern of the vortices in a rapidly rotating strongly interacting Bose–Einstein condensate by the particle scattering method. We also have obtained de Haas-van Alphen-like oscillations in the differential scattering cross-section for an ideal ultracold Fermi gas in a rotating harmonic trap for $T \to 0$. Our predictions on the differential scattering

cross-sections can be tested within the present-day experimental setups.

In chapter 4, we have analytically explored the quantum phenomena of particle scattering by harmonically trapped trapped quantum (Bose or Fermi) gases of electrically neutral atoms exposed to a uniform artificial magnetic field for the short-ranged Fermi-Huang interactions between the incident particle and the scatterers. We have considered elastic scattering. For the bosonic scatterers, we have obtained the differential scattering cross-section around the Bose-Einstein condensation point. For the fermionic scatterers, we have obtained artificial magnetic field dependent differential scattering cross-section exhibiting de Haas-van Alphen like oscillations for $T \to 0$. Here, the main difference from the theoretical study mentioned in chapter 2 is coming from the centrifugal force in the rotating frame. The difference has also been further made by the consideration of the inelastic scattering for all the above cases.

5.2 Future Scopes

The future scopes of the Ph.D. works can be described chapter-wise as follows.

In chapter 2, we have obtained differential scattering cross-section for the Fermi-Huang interaction between an incident particle and a quantum harmonic oscillator at a finite temperature. We have obtained the differential scattering cross-section for a Bose or Fermi gas of quantum harmonic oscillators at a finite temperature. Our study [1] would be important to know about the scatterer(s), in particular, (i) the energy eigenstate of a single scatterer in a harmonic trap, (ii) onset of the Bose-Einstein condensate of a harmonically trapped Bose gas. The differential scattering crosssection for the gas of quantum harmonic oscillator depends on the temperature and the quantum (Bose/Fermi) statistics involved in the gas. Thus, our study would also be important to distinguish the bosonic or fermionic character of a gas of scatterers as their collective property. The angular distribution of the scattering cross-section allows to estimate the size of the condensate, and its intensity makes it possible to determine the number of particles trapped in the condensate. Our results on differential scattering cross-section can be tested within the present-day experimental setups for weakly interacting trapped ultra-cold Bose and Fermi gases, Bose-Einstein condensates (BECs) for haromically trapped bose gas, and BECs in an optical lattice and double well potential, etc.

In chapter 3, we have theoretically obtained the differential scattering crosssection for a rotating harmonically trapped Bose and Fermi gas. The differential scattering cross-section depends on the vortex structure of the rapidly rotating Bose-Einstein condensate. Our study [2] would be important to know about the scatterer(s), in particular, (i) the energy eigenstate of a single scatterer in a rotating harmonic trap, (ii) onset of the Bose-Einstein condensate of a harmonically rotating trapped Bose and Fermi gas, (iii) vortex structure of a rapidly rotating harmonically Bose-Einstein condensate, and (iii) de Haas-van Alphen like effect on a rotating harmonically trapped Fermi gas [2, 3].

In chapter 4, we have obtained theoretical results for differential scattering cross-section for a harmonically trapped Bose or Fermi gas exposed to a uniform artificial magnetic field [4]. The Hamiltonian of an uncharged harmonic oscillator exposed to an artificial magnetic field in a rest frame differs from the Hamiltonian of a rotating uncharged harmonic oscillator in the rotating frame by the centrifugal potential. This leads to a significant difference in the collective property as well as in the differential scattering cross-section for the harmonically trapped Bose or Fermi gas in artificial magnetic field from that of the rotating harmonically trapped Bose or Fermi gas. Above all, the differential scattering cross-section, as well as the scattering cross-section, would appear as a thermodynamic property for the harmonically trapped ultracold Bose or Fermi gas from our study.

Bibliography

- [1] A. Bhattacharya, S. Das, and S. Biswas, J. Phys. B: At. Mol. Opt. Phys. **51**, 075301 (2018)
- [2] S. Das and S. Biswas, Phys. Scr. 96, 125037 (2021)
- [3] S. Das, Phys. Lett. A 397, 127249 (2021)
- [4] S. Das, Physica B **635**, 413833 (2022)

Particle Scattering by Ultracold Quantum Gases of Trapped Atoms

by Samir Das

Librarian

Indira Gandhi Memorial Library UNIVERSITY OF HYDERABAD

Central University P.O. HYDERABAD-500 046.

Submission date: 23-Mar-2023 04:51PM (UTC+0530)

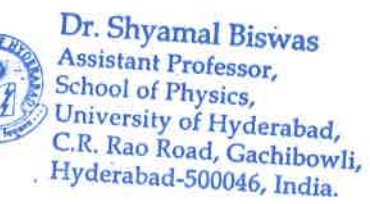
Submission ID: 2044364041

File name: PhD-Thesis_Samir-Das.pdf (4.92M)

Word count: 39457

Character count: 193428

Sh I Ri



Particle Scattering by Ultracold Quantum Gases of Trapped **Atoms**

ORIGINALITY REPORT

SIMILARITY INDEX

INTERNET SOURCES

PUBLICATIONS

STUDENT PAPERS

PRIMARY SOURCES

Samir Das, Shyamal Biswas. "Particle scattering by rotating trapped quantum gases & at finite temperature", Physica Scripta, 202 pr. Shyamal Biswas Assistant Professor, **Publication** School of Physics,

Samir Das. "Particle scattering by harmonically trapped quantum gases in an artificial magnetic field", Physica B: Condensed Matter, 2022

Publication

Dr. Shyamal Biswas Assistant Professor, School of Physics, University of Hyderabad, C.R. Rao Road, Gachibowli, Hyderabad-500046, India.

University of Hyderabad, C.R. Rao Road, Gachibowli, Hyderabad 100/46 India.

Ankita Bhattacharya, Samir Das, Shyamal Biswas. "Particle scattering by harmonically trapped Bose and Fermi gases", Journal of Dr. Shyamal Biswas Physics B: Atomic, Molecular and Optical Physics, 2018 Publication

Assistant Professor. School of Physics, University of Hyderabad, C.R. Rao Road, Gachibowli, Hyderabad-500046, India.

Samir Das, Shyamal Biswas. "Particle

scattering by rotating trapped quantum gases at finite temperature", Physica Scripta, 2021Dr. Shyamal Biswas

Publication

Assistant Professor, School of Physics,

University of Hyderabad, C.R. Rao Road, Gachibowli, Hyderabad-500046, India.

This is from the student's own papers. www.researchgate.net

Internet Source

Dr. Shyamal Biswas Assistant Professor, School of Physics, University of Hyderabad, C.R. Rao Road, Gachibowli, Hyderabad-500046, India.



Dr. Shyamal Biswas Assistant Professor, School of Physics, University of Hyderabad, C.R. Rao Road, Gachibowli, Hyderabad-500046, India.

This is from the group of the supervisor. www.arxiv-vanity.com Internet Source

Dr. Shyamal Biswas Assistant Professor, School of Physics, University of Hyderabad, C.R. Rao Road, Gachibowli,

Hyderabad-500046, India.

sealzhang.tk Internet Source

Samir Das. "Inelastic particle scattering by rotating harmonically trapped quantum gases", Physics Letters A, 2021 Assistant Professor,

Dr. Shyamal Biswas

School of Physics,

Publication

University of Hyderabad, Saeidian, Shahpoor. "Scattering resonances lead to the said of the ultracold atoms in confined geometries", 'American Association for Cancer Research (AACR)', 2008

Internet Source

10	vdoc.pub
	Internet Source

mafiadoc.com Internet Source

Submitted to University of Hyderabad, 12 Hyderabad

Student Paper

arxiv4.library.cornell.edu Internet Source

www.tcm.phy.cam.ac.uk Internet Source



UNIVERSITY OF HYDERABAD

SCHOOL OF PHYSICS

C.R. Rao Road, Gachibowli, Hyderabad-500046, INDIA

DR. SHYAMAL BISWAS Assistant Professor Email: sbsp@uohyd.ac.in

Mobile: +91-9542206208 Telephone: +91-40-2313 4366/4400

Certificate for the Originality

This is to certify that the Ph.D. (Physics) thesis entitled "particle scattering by ultracold quantum gases of trapped atoms" submitted by Mr. Samir Das (Reg. No. 16PHPH09) is an outcome of his original research work done under my supervision. This thesis has been screened for originality by the Turnitin Software on March 23, 2023 at the Indira Gandhi Memorial Library of the University of Hyderabad. The software detects 53% similarity index out of which 44% comes from the student's own research articles as listed below.

- 1. A. Bhattacharya, S. Das, and S. Biswas, J. Phys. B: At. Mol. Opt. Phys. 51, 075301 (2018) [A similar work was also posted to arXiv:1606.02804v5 (2018) and ResearchGate (2018).]
- 2. S. Das and S. Biswas, Phys. Scr. 96, 125037 (2021) [A part of this work was also posted to ResearchGate (2021).]
- 3. S. Das, Phys. Lett. A 397, 127249 (2021)
- 4. S. Das, Physica B **635**, 413833 (2022)

The remaining amount 53% - 44% = 9%, therefore, is the effective similarity index which though is lying below the maximum permissible limit (10%), is coming from the resemblance caused by the frequent use of the well-known standard terms such as scattering, elastic scattering, inelastic scattering, light scattering, scattering amplitude, scattering length, differential scattering cross-section, scattering cross-section, particle scattering, quantum scattering, temperature, quantum gases, Hamiltonian, Schrodinger equation, eigenstate, eigenvalues, quantum number, Bose-Einstein statistics, Bose-Einstein condensate, Fermi-Dirac statistics, Bose gas, Fermi gas, harmonic oscillator, harmonic trap, double-well potential, optical lattice, vortex lattice, rotating trap, Landau levels, de Haas-van Alphen effect, artificial magnetic field, etc. The use of such terms is rampant in the literature, and hence it is not surprising that the similarity index is artificially inflated. It should be noted that the use of such standard terms cannot be avoided. Hence the thesis is free from plagiarism.

Date: March 27, 2023 Place: Hyderabad Dr. Shyamal Biswas [Thesis Supervisor]

Shall Bins

